Detailed Characterization of Flowfields and Uncertainty in a Speed-Bump Turbulent Separated Flow Validation Experiment

Matthew L. Robbins

A thesis
submitted in partial fulfillment of the
requirements for the degree of

MASTER OF SCIENCE IN AERONAUTICS & ASTRONAUTICS

University of Washington

2021

Reading Committee:

Owen Williams, Chair

Antonino Ferrante

Program Authorized to Offer Degree:
College of Engineering,
William E. Boeing Department of Aeronautics and Astronautics

The views expressed in this thesis are those of the author and do not reflect the official policy or position of the United States Air Force, Department of Defense, or the U.S. Government.

This material is declared a work of the U.S. Government and is not subject to copyright protection in the United States.

University of Washington

Abstract

Detailed Characterization of Flowfields and Uncertainty in a Speed-Bump Turbulent Separated Flow Validation Experiment

Matthew L. Robbins

Chair of the Supervisory Committee:
Research Assistant Professor Owen Williams
Aeronautics & Astronautics

Experimental examinations of incompressible flow over a novel speed-bump geometry were conducted towards the development of a turbulence model validation dataset for separated flows. Efforts to characterize the boundary conditions of the experiment were performed including a survey of flow uniformity and side-wall boundary layers at the inflow plane of an empty test section, and measurement of the as-built test model. Surface pressures over the speed-bump were examined and revealed a series of favorable and adverse pressure gradients in the streamwise direction with features associated with a quasi-two-dimensional line of flow separation. Statistical measurements of the flowfield were obtained with planar particle image velocimetry to ascertain model-installed inflow properties, the extent of relaminarization on the upstream slope of the speed-bump, and the size and shape of the separated region. The features of separation, in both the flowfield and on the surface, exhibited a dependency in Reynolds number below $Re_L = 2.55 \times 10^6$ and generally poor agreement with corresponding RANS simulations. Extensive documentation of the experimental facility, instrumentation, signal processing procedures, and treatment of uncertainty is provided to establish a high level of validation completeness. In accordance with the framework of Oberkampf and Smith [1], the model validation completeness of this experiment meets at least level one completeness and is at or approaching level two for most attributes.

TABLE OF CONTENTS

LIST OF FIGURES

LIST OF TABLES

NOMENCLATURE

H: Confinement, distance from top of splitter plate to tunnel ceiling

L: Width of tunnel cross section, 36 in

L_b: Width of speed-bump, 35.5 in

P: Pressure

P_a: Ambient pressure

R: Specific gas constant (dry air), 287.05 J/kg K

T: Temperature

U: Mean streamwise velocity

W: Mean vertical velocity

u_τ: Friction velocity, $= \sqrt{\tau_w/\rho}$

Z: Wall-normal distance

a: Image calibration scale factor

h: Speed-bump height

q: Dynamic pressure

s: Pitot rake station

t: Time

u: Streamwise velocity fluctuation

w: Vertical velocity fluctuation

x: Streamwise coordinate OR characteristic length scale

y: Spanwise coordinate

z: Vertical coordinate

Δ: Differential

δ: Boundary layer thickness (at 99% U_∞) OR uncertainty

μ: Dynamic viscosity

ν: Kinematic viscosity

ρ: Density

σ: Standard deviation

τ_w: Wall shear stress

Subscripts

∞: Freestream conditions

s: From all pitot tube locations at a station

vel: From all stations at a nominal velocity

Subscripts

$\overline{x}$: Time average

$\widetilde{x}$: Median

x^+: Normalized using inner coordinates

ACKNOWLEDGMENTS

First and foremost, I would like to thank my advisor, Dr. Owen Williams, for his support, advice, and patience during what has been undoubtedly one of the most educational endeavors of my academic career. This work simply would not have come together without his active involvement over the past year and a half.

I'm thankful for the support of those in my lab, especially Madeline Samuell and Hariprasad Annamalai, who worked alongside me during this project. I would also like to thank Sahil Kommalapati for his help in the wind tunnel.

The Boeing Company was an instrumental collaborator with this project, and I am especially thankful for the technical advice provided by Mr. Jeffrey Slotnick and Dr. Philippe Spalart.

I'm grateful that the United States Air Force allowed me to pursue this degree as a first assignment, and I appreciate the folks at the Air Force Institute of Technology - Civilian Institution Programs who supported my time at the University of Washington.

I also owe a debt of gratitude to the Department of Aeronautics at the United States Air Force Academy who motivated and prepared me to pursue a graduate-level degree, especially my former research advisors, Dr. Thomas Yechout and Dr. Casey Fagley.

Last, but certainly not least, thank you to my family and friends who continuously support me throughout life. I'm incredibly lucky and blessed to know each of you.

DEDICATION

To Goose: a very, very, good boy.

Chapter 1
INTRODUCTION

THE rapid pace of aircraft design and aerodynamic research simply could not be sustained without the aid of computational tools. In Computational Fluid Dynamics (CFD), the governing equations of fluid dynamics are cast in a numerical scheme to solve for the motion of a fluid under a specified set of initial and boundary conditions. By computationally solving for the fluid properties (e.g. velocity, pressure, etc) over an object, other meaningful information (e.g. forces and moments) can be deduced with less reliance on expensive and time-consuming wind tunnel or flight testing. For both engineers and scientists, CFD is a powerful tool to rapidly expedite the design or research process while providing data with a spatial resolution that is challenging to obtain using other methods.

Although CFD has significantly advanced in capability over the previous three decades, it still faces a compelling list of limitations and is not yet trusted as a sole source of information in most practical engineering problems. The difficulty lies in CFD's attempt to resolve the stochastic motion of a turbulent fluid. The dynamics of a fluid are governed by a set of partial differential equations known as the Navier-Stokes equations. In particular, the equations that express the conversation of momentum in an incompressible, Newtonian fluid are:

$$\rho \left[\frac{\partial u_i}{\partial t} + u_j \frac{\partial u_i}{\partial x_j} \right] = -\frac{\partial p}{\partial x_i} + \frac{\partial T_{ij}^{(\upsilon)}}{\partial x_j} \tag{1.1}$$

where u_i and $T_{ij}^{(\upsilon)}$ are instantaneous components of velocity and the viscous stress tensor respectively [2].

As of this writing, a closed-form analytic solution to these equations do not exist due, in large part, to the non-linear $u_j \frac{\partial u_i}{\partial x_j}$ convective acceleration terms in the equations (see [3]). It can be shown that these terms are relevant as the inertial forces of the fluid overcome the

dissipating effects of viscosity, represented by the non-dimensional Reynolds number:

$$Re = \frac{\rho U x}{\mu} \tag{1.2}$$

When this value is greater than the critical Reynolds number defined for the characteristic flow, the fluid is said to be in the turbulent regime. Unlike laminar flow, turbulent motion is chaotic (e.g. smoke rising off a smoldering fire, or eddies in the wake of a boat). Most engineering problems of practical significance, such as aircraft flight, are partially or fully in the turbulent regime.

Since a closed-form analytic solution to Eq. 1.1 does not exist, solving for the evolution of velocity and pressure in the natural representation of the Navier-Stokes requires that Eq. 1.1 be numerically solved with an extremely fine spatial resolution at many instantaneous moments in time (i.e. a direct numerical simulation, or DNS). While this is a valid method in principle, in practice the computational energy, time, and storage requirements to perform DNS on most engineering problems far exceed the current capability of the state-of-the-art, especially for flows at high Reynolds numbers.

Today, most CFD applications employ the governing equations with some degree of assumption. The most common industrial applications of CFD utilize the Reynolds Averaged Navier Stokes (RANS) equations. With RANS, the instantaneous velocity, pressure, and viscous stress terms of Eq. 1.1 are decomposed into their mean (uppercase) and fluctuating (lowercase) components and averaged. The resulting equation for the averaged motion is:

$$\rho \left[\frac{\partial U_i}{\partial t} + U_j \frac{\partial U_i}{\partial x_j} \right] = -\frac{\partial P}{\partial x_i} + \frac{\partial}{\partial x_j} \left[T_{ij}^{(v)} - \rho \left\langle u_i u_j \right\rangle \right] \tag{1.3}$$

This operation simplifies the equations by considering only the steady, mean components of the flow rather than the unsteady instantaneous motion. However, a consequence of the non-linearly of Eq. 1.1 is the introduction of six new and unknown 'Reynolds stress' terms, $\langle u_i u_j \rangle$. These terms quantify the turbulent features of the flow, but are without any constitutive relation to the fluid itself and cause the system of equations to be poorly-posed,

with too many unknown variables. Equations for the Reynolds stresses could be derived from the equations governing the fluctuations themselves, but this would introduce even more higher-order unknown terms. The inability to naturally relate the Reynolds stresses to the mean motion of the flow without the introduction of unknown terms is known as the 'turbulence closure problem'.

The RANS equations, then, must be closed by turbulence models that *approximate* the relation of the Reynolds stresses to the mean motion of the flow. Many turbulence models employ Boussinesq's hypothesis:

$$-\rho\left\langle u_i u_j\right\rangle + \frac{1}{3}\left\langle u_i u_j\right\rangle = \mu_t\left[S_{ij} - \frac{1}{3}S_{kk}\delta_{ij}\right] \tag{1.4}$$

where S_{ij} is the mean strain rate, δ_{ij} is the Kronecker delta, and μ_t is the 'eddy viscosity'.

Turbulence models of this type approximate the value of eddy viscosity in equations with variable constants that must be tuned to the flow of interest, and therefore may lack predictive capability across a range of flow problems. The need for modeling introduces a healthy degree of skepticism when simulating many practical situations, such as regions of transition and flow separation. As turbulence models are created, studied, and improved, they must have a standard of comparison to assess their efficacy in simulation. Results from experimental test campaigns act as this validation standard.

NASA's CFD Vision 2030 Study [4], the industry's path towards improvement of simulation capabilities, mentions, "Key experimental datasets are critically important in the ongoing development and refinement of the full range of turbulence models". The availability of experimental data suitable for validation purposes has generally lacked, due to the stringent requirements for characterization of the experiment, in addition to the assessment of relevant flow physics. The study detailed in this manuscript aims to fill this void by producing benchmark-quality validation data in an experimental test campaign specifically designed for this purpose.

This study features a new 'speed-bump' geometry that is relevant to wing-like configurations and induces a variety of flow features that challenge the current capabilities of CFD,

including a large region of turbulent separated flow at moderately high Reynolds numbers. Building on the previous studies of Sarwas [5], Samuell [6], and Williams et. al. [7], multiple experimental methods will be employed to measure important features of separation and to characterize the experiment. A geometric scan of the as-built test geometry will be discussed, along with an assessment of inflow uniformity and side-wall boundary layers, measurement of surface pressure over the speed-bump, and a detailed analysis of the flowfield using particle image velocimetry (PIV). Additionally, some results will be compared with Samuell's [6] corresponding computational simulation of the experiment to explore the ability of RANS to predict the unique features of this flow problem.

This report attempts to document the study with a level of detail not commonly seen in traditional test campaigns, and with a rigorous treatment of uncertainty. First, a background of model validation will be presented in Chapter 2, including a description of the framework used to assess the completeness level of validation experiments, an overview of previous and ongoing validation studies, and a detailed description of the 'speed-bump' geometry. Chapter 3 will outline the methods used to collect and reduce the experimental data obtained in this study. Results will be presented in Chapter 4, grouped by characterization data (test article measurement, inflow uniformity and boundary layers), followed by relevant system response quantities (surface pressure profiles and spatial flowfields). Finally, Chapter 5 offers a conclusion of the work with an appraisal of the validation completeness of the dataset and recommendations for further research. In an effort to fully elucidate the experiment, the appendices of this report are extensive and contain thorough documentation of the experimental facility, equipment, reduction methods and results.

Chapter 2

BACKGROUND

Model validation efforts fall under the broader classification of CFD verification and validation (V&V). While the terms may appear identical, validation and verification studies are fundamentally different. Verification considers the numerical aspects of the model (i.e. stability, round-off and truncation errors, solution convergence) and is beyond the scope of this study. Validation, however, analyzes the accuracy of the model from a physical standpoint (i.e. how well the model predicts reality). In other words, verification efforts help determine whether the equations of the model are used properly, while validation determines whether the proper equations are used [8].

Several methods are available to validate a mathematical model. In fluid dynamics, full-scale testing (e.g. flight test) is perhaps the most accurate means to observe the true behavior of a flow since it does not suffer from the adverse effects of scaling. Acquiring data with a high spatial and temporal resolution at this scale is incredibly challenging and costly, however. A direct numerical simulation of the Navier Stokes could be used as its own standard for turbulence models but may be subject to unverified numerical errors and, for the reasons discussed previously, is still prohibitively expensive at the Reynolds numbers encountered in most flows of engineering significance. This often leaves experimental testing as the only viable means to validate a mathematical model.

Oberkampf et. al. [1, 8, 9] published a comprehensive methodology for CFD V&V that is commonly referenced within the field. While data from traditional experiments can be used for validation purposes, these authors stress that this data is often not sufficiently detailed. Traditional experiments may aim to gain a clearer understanding of a physical phenomenon or develop approximate engineering solutions by collecting only the data needed to that end

[9]. Validation experiments similarly aim to capture these relevant flow features but have an additional burden of *characterizing* the experiment to the greatest extent possible.

Features worthy of characterization include both the system response (i.e. the measured features in an experiment, or the output of the model), and the secondary aspects of the flow which may influence the system response. For example, if a traditional turbulent separated flow experiment seeks to ascertain the sensitivities of flow separation, the system response could be a collection of wall shear-stress distributions under a variety of freestream conditions. In a corresponding turbulent separated flow validation experiment, the same system response should be considered, in addition to properties of the inflow (e.g. uniformity and freestream turbulence), a detailed geometry of the wall, a record of ambient conditions during the test, statistical properties of measured quantities, etc.

This additional characterization is often unnecessary for the narrative of a traditional experiment. Although, for validation purposes, it is crucial to provide this additional data since it serves as an input to the numerical model in simulations. Discrepancies between experimental results and the model output could be due to deficiencies in the model, or because its inputs were not consistent with the actual conditions of the experiment. To remove this ambiguity, validation experiments must be tightly integrated with their corresponding simulations and provide sufficient detail of *both* inputs and outputs to/from the model.

2.1 Validation Experiment Completeness Framework

Oberkampf and Smith (2017) [1] provide a widely used framework to assess what level of detail is sufficient in the characterization of a validation experiment. The authors argue that validation datasets should contain a characterization of the experiment with adequate detail for input to a direct numerical simulation of the flow problem. They admit that this is an extraordinary and unprecedented level of detail, but is justified since DNS may be more prolific with the advancement of technology in the coming decades. In pursuit of this goal, the authors proposed a rubric to assess the completeness of validation datasets, with four model validation experiment completeness (MVEC) levels and six experimental attributes.

The six experimental attributes are:

1. *Experimental Facility*: operation, design, and calibration of the experimental facility

2. *Analog Instrumentation and Signal Processing*: sensors, transducers, data acquisition, processing, and recording of measurements

3. *Boundary and Initial Conditions*: measurement of boundary conditions, initial conditions, and test article geometry needed for modeling the flow

4. *Fluid and Material Properties*: fluid properties and characteristics, and thermal and mechanical properties of solids that may be modeled

5. *Test Conditions*: test conditions of the facility, particularly how they may vary during an experiment or from one experiment to the next

6. *System Response Quantities*: quantities that are measured in the experiment, most of which are predicted by the model, i.e. considered as model outputs

where each attribute is assessed one of four MVEC levels depending on the amount of qualitative and quantitative data that is documented:

- *Level 0*: Little or no information is provided on an attribute

- *Level 1*: Some information is provided for an attribute, including assumptions made and an estimate of measurement uncertainty

- *Level 2*: Detailed information is provided for an attribute, including assumptions made and an estimate of total experimental uncertainty

- *Level 3*: Detailed information is provided for an attribute, e.g., highly resolved spatial and temporal measurements, along with an extensive discussion of assumptions

made, data processing procedures, and a comprehensive estimate of total experimental uncertainty

Detailed explanations of the attributes at each level are provided in [1] along with examples of each element in an incompressible wind tunnel experiment. It is important to note that although some attributes are not directly related to the numerical model, they are still relevant for validation purposes. For example, in a wind-tunnel experiment, the aerodynamic features of the flow and the final data products produced in the experiment are linked by a process of acquisition, signal processing, and reduction in a measurement system (hence, 'system response quantity'). Detailed documentation of the sensors used to acquire the measurement and the subsequent signal conditioning procedure allows computationalists to perform a similar treatment of the simulation outputs for a truly accurate comparison of the simulation and experiment's results.

Given that it is impossible to experimentally measure the exact true value of a quantity, a quantification of uncertainty should accompany all measured and derived quantities in the validation dataset for high levels of completeness. Since even modest amounts of uncertainty in model inputs can be propagated to a large extent within the model, uncertainty must be minimized to the greatest extent possible in the products of a validation study. Uncertainty estimation is a complicated and controversial process, with a variety of techniques and assumptions available. In this study, total uncertainty is expressed as the root-sum-square (RSS) of the bias (epistemic) and random (aleatoric) components of uncertainty. For a measured value, the former is associated with the measurement equipment and is often provided by the manufacturer or through a calibration, while the latter is a statistical representation of the variability of a measurement. For derived quantities, measured uncertainties are propagated using a Taylor Series method. The convention adopted in this study is detailed further in Section 3.5 and Appendix C.

The authors of the validation framework remark that a completeness level can only be assessed when substantiated with sufficient documentation. Furthermore, they claim that

an attribute's completeness level does not have to be an integer value, but must satisfy all elements of the preceding integer. Additionally, they stress that the 'overall' completeness of the dataset must be judged in an atomistic sense and not from the arithmetic mean of the levels of all six attributes. The speed-bump experiments described in this report aimed for level two completeness in all experimental attributes.

2.2 Related Validation Studies of Turbulent Separated Flow

The complexities associated with smooth-body separation (e.g. unsteady and three-dimensional separation, recirculating and highly turbulent flow downstream of separation, reattachment, etc.) make this flow regime a formidable test of turbulence modeling capabilities. These challenges, and their relevance to wing-like geometries, make hill and bump-like shapes very popular for turbulence model validation.

Byun et. al. defined one of the earliest experimental smooth body separation studies of an axisymmetric hill [10–12]. Using a combination of oil flow visualization techniques, high-frequency surface pressure measurement, and laser Doppler velocimetry (LDV), the separated region of the flow on the leeward side of the hill was characterized. The line of flow separation near the hill's apex was found to be three-dimensional, producing a series of vortical structures that merged farther downstream. Surface-flow visualizations revealed a reattachment point preceded by a large region of reversed flow, and a small pocket of slow-moving separated flow slightly aft of the hill's apex. Corresponding large-eddy simulations of this geometry [13, 14] followed, and showed poor agreement with the experimental results within and near the separated region.

Bell et. al. revisited the axisymmetric hill geometry in 2012 with the FAITH Hill (Fundamental Aeronautics Investigates the Hill) model, shown in Fig. 2.1a [15]. This study employed a variety of experimental methods, including water tunnel dye injection, particle image velocimetry, pressure-sensitive paint, and fringe imaging skin friction [16]. This study demonstrated the utility of using multiple measurement techniques to observe the flow and produced an initial analysis of the flowfield, with findings similar to those of Byun et. al.

While the axisymmetric hill experiments provided an analysis of the flow physics involved with smooth body separation, considerable effort remained towards the characterization of the experiments for their data to be considered a suitable, strong-sense validation benchmark. Oberkampf and Smith claim that, "although several validation experimental databases are available ... strong-sense benchmarks do not presently [2014] exist in science or engineering" [17].

Since 2014, a few studies began to provide validation data with the emphasis on experimental characterization needed for benchmark-status. The Axisymmetric Transonic Hump and CFD Challenge, posed by Lynch et. al. at Sandia National Laboratories in 2019 [18], is one example. In this ongoing study, an axisymmetric model with a spherical hump (see Fig. 2.1b) is investigated at transonic speeds in a wind tunnel. In addition to the relevant system response quantities, a suite of experimental techniques are employed to measure the boundary conditions of the experiment, including mean values of the stagnation and test section pressure and temperature, turbulence intensity, and tunnel wall boundary layer profiles [19]. This data is intended to invite an ongoing blind-comparison to simulation results provided by the CFD community. This study also prescribes metrics of comparison between the experimental and simulation results [20], which is a key requirement for benchmark datasets.

Another prominent validation campaign currently underway is a joint effort between NASA and Virginia Polytechnic and State University to investigate subsonic flow over the superelliptic-shaped, wall-mounted 'BeVERLI Hill' (Benchmark Validation Experiment for RANS and LES Investigations) [21–26]. The wind tunnel used in the BeVERLI study is modified with sensors in the inlet preceding the test section to allow for the measurement of velocity, temperature, and pressure inflow boundary conditions. Additionally, the model is symmetric and can be rotated through four identical orientations on each wall of the test section, allowing for the quantification of random error contributions by geometric uncertainty and inflow non-uniformity. The BeVERLI Hill features highly three-dimensional flow with a relatively large boundary layer to hill-height ratio ($\delta/h = 1/3$), and targets level three completeness in all experimental attributes.

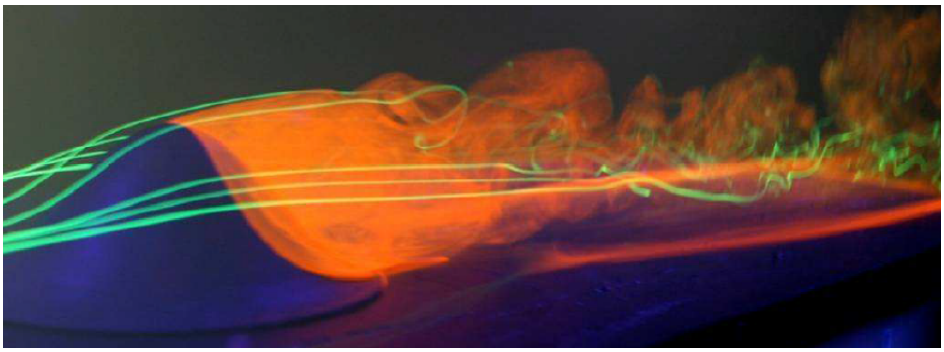

(a)

(b)

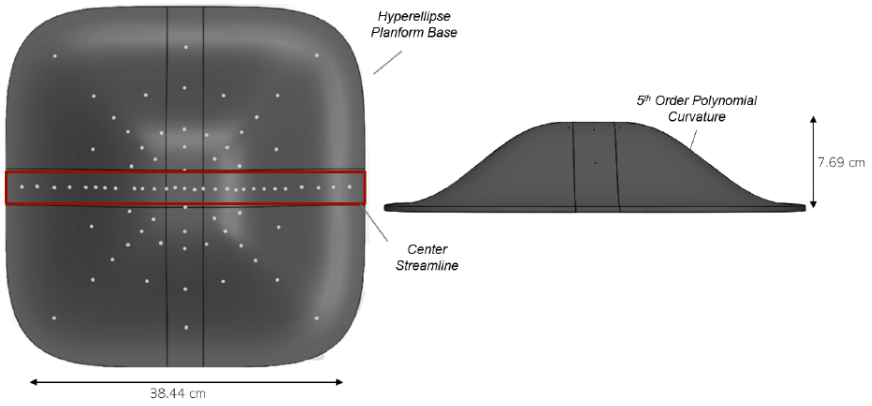

(c)

Figure 2.1: Geometries of previous/ongoing validation experiments: (a) FAITH Hill [15], (b) Sandia Axisymmetric Transonic Hump and CFD Challenge [18], and (c) BeVERLI Hill [25]

2.3 The 'Speed-Bump' Geometry

The test campaign detailed in this report aims to build upon previous and ongoing validation efforts by collecting benchmark-quality data using a novel test geometry. The speed-bump was designed to deliberately induce flow features that stress the current capabilities of turbulence modeling while remaining simple to integrate in experiments and simulation. Slotnick [27] detailed several critical requirements for validation geometries needed to decisively advance the state-of-the-art in CFD turbulence modeling, including a point of flow separation that is not strongly controlled by the geometry, a number of control parameters to affect separation (e.g. Reynolds number, inflow boundary layer, etc.), and amenability to both experiments and simulation.

The Gaussian elongated hill or 'speed-bump' geometry was chosen to satisfy these requirements; it follows the following equation:

$$z(x,y) = \frac{h_0}{2} e^{-\left(\frac{x}{x_0}\right)^2} \left[1 + erf\left(\frac{\frac{L_b}{2} - 2y_0 - |y|}{y_0} \right) \right] \tag{2.1}$$

where $x,\ y,\ z$ are the streamwise, spanwise and wall-normal directions, respectively. The length, L_b is 35.5 inches, and the design variables were chosen to be $x_0 = 0.195L_b$, $y_0 = 0.06L_b$, $h_0 = 0.085L_b$, such that the resulting bump height is $h = 0.085L_b$. The bump geometry is plotted for streamwise and spanwise centerline planes in Figure 2.2.

The streamwise Gaussian profile resembles a wing-like shape that presents a unique challenge to turbulence models by promoting flow separation without dictating a constant separation point. The Gaussian profile tapers towards the side walls in the shape of an error function to promote quasi-two-dimensional flow at the spanwise centerline while minimizing interaction with the walls. It was decided early in the design process that the tunnel walls and ceiling would be included in the simulation definition of the flow problem, allowing the amount of confinement between the geometry and the ceiling to be a parameter to affect the extent of flow separation. The inflow boundary layer thickness and Reynolds number are tunable parameters to study the extent of flow separation as well. The boundary layer

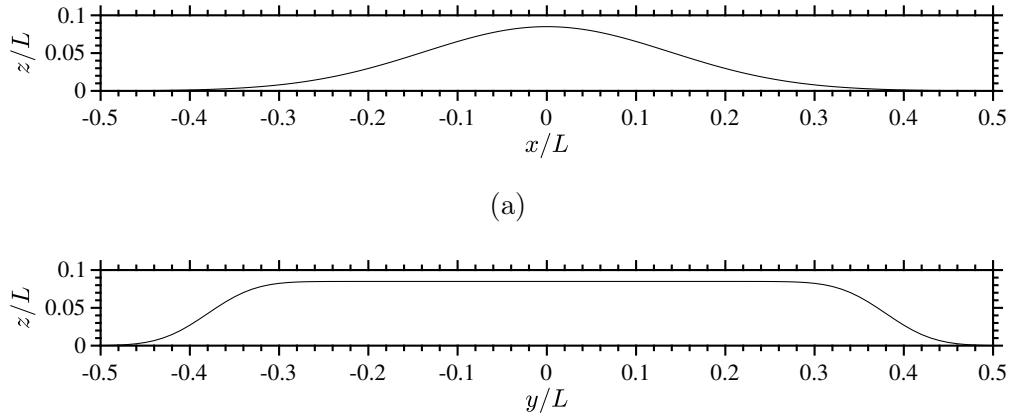

Figure 2.2: Geometry of bump model in (a) streamwise and (b) spanwise directions relative to wind tunnel test section width, L. [7]

thickness to bump-height ratio is deliberately small ($\delta/h \approx 1/12 - 1/10$), distinguishing this geometry from previous asymmetric hill studies. Additionally, the speed-bump features two planes of symmetry, which aid the quantification of uncertainty caused by imperfections in the as-built test article. With all of these features, the geometry still remains practical for use in corresponding simulations.

Sarwas [5] initiated the experimental examination of the speed-bump with studies to investigate the tripping of the inflow boundary layer, a survey of the inflow free-stream turbulence, a china-clay flow visualization, and an initial measurement of surface pressure variation over the bump. Samuell [6] expanded upon the characterization of the inflow boundary layer profile and studied the effect of changes in Reynolds number and confinement on surface pressure. A strong region of flow separation was observed on the leeward side of the speed-bump for all Reynolds numbers tested ($1.32 \leq Re_L \times 10^6 \leq 3.41$), along with two counter-rotating surface vortices located shortly downstream of the ridge. The surface pressure profiles indicated a series of adverse and favorable pressure gradients encountered along the streamwise direction of the flow, with the point of separation occurring shortly

downstream of the speed-bump apex in an adverse pressure gradient region. The surface pressure profiles were found to be insensitive to changes in Reynolds number above $Re_L = 2.46 \times 10^6$.

Samuell [6] also detailed a comparison to a corresponding RANS simulation of the geometry, showing a similar insensitivity to Reynolds number in surface pressure, albeit with the opposite trend observed in experiments. The simulation failed to capture a similar surface pressure profile as experiments in the separated region. The dynamics of separation were found to be highly dependent on the RANS turbulence model employed, although these results were more similar to themselves than the experimental data. Overall, these simulations exposed the significant deficiencies of RANS in predicting smooth-body separation. Wall-modeled large-eddy simulations (LES) of this geometry were performed by Iyer and Malik [28], Wright et. al. [29], and Balin et. al. [30, 31]. In these simulations, RANS similarly struggled to predict near-wall physics where an adverse pressure gradient was encountered and consequently failed to capture the separation trends observed in experiments.

DNS simulations of a 2D cross-section of this geometry were performed by Uzun and Malik [32] and Balin et. al. [30], who postulated that relaminarization may occur on the upstream slope of the speed-bump in the favorable pressure gradient region, and incipient or weak separation of the flow in the adverse pressure gradient region. While these simulations were conducted at a lower Reynolds number than the experiments, both the possibility of relaminarization and the extent of separation, especially at the lower Reynolds numbers of the experiment, became points of interest for future experimental research following these simulations.

While these simulations expounded important flow information relevant to this geometry, it can be argued that the experiment was not fully represented in these simulations since many experimental characterization inputs were not available at the time. Thus, the primary goal of the effort described in this thesis was to adequately characterize this validation experiment such that a faithful representation could be made in corresponding simulations.

Chapter 3

EXPERIMENTAL METHODS

3.1 Facility

All experimental results were obtained in the Low-Speed Wind Tunnel (LSWT) at the University of Washington. LSWT is located in the historic Aeronautics Laboratory on the Seattle campus. The Aeronautics Laboratory, originally built in 1917, houses a single 1,612 square foot room with the wind tunnel at its center. The floor is 8 feet underground, with concrete walls below grade and wood walls above. The floor is accessed by one of two wooden staircases on the east and west walls, approximately 3 feet in width. Storage cabinets, work benches, and other test articles are neatly arranged along the side-walls, extending no more than two feet towards the center of the room as shown in Fig. 3.1. Detailed building schematics of the Aeronautics Laboratory are illustrated in Figs. A.5 and A.6 in Appendix A.

The interior temperature of the facility is controlled by a JencoFan NBCR belt drive centrifugal power roof exhauster capable of flow rates up to 4,984 cubic feet per minute [33, 34], located directly above the tunnel contraction. A louvered ceiling inlet is situated directly above the fan diffuser section and allows fresh air to enter the room while the exhaust fan is in operation. The exhaust fan was started and the room was allowed to reach a steady-state temperature prior to initiating a test.

LSWT is an open-circuit type wind tunnel powered by a 200HP, constant speed motor with pneumatically actuated, variable pitch fan blades and is capable of holding speeds from 34 to 135 mph within 0.1 mph over the duration of a test (30 minutes to 1 hour). The walls of the tunnel are constructed out of a composite, laminate, fiberglass reinforced plastic with a rigid PVC foam core. The interior surface is finished with a smooth polyester gel-coat. Flow

(a)

(b)

Figure 3.1: Low-Speed Wind Tunnel facing (a) upstream and (b) downstream in the Aeronautics Laboratory at the University of Washington.

enters the tunnel through a 9 foot square inlet and is conditioned by a foam filter media, a perforated plate, an aluminum honeycomb, and a high porosity screen. A previous inflow survey of this tunnel measured excellent freestream turbulence intensity values of 0.2% or less across the entire velocity range [5]. The test section is 3 feet by 3 feet by 8 feet with 1 1/4 inch thick type GM plexiglass walls and 5 inch radiused fiberglass corners. The test section is accessed through a 26 inch by 7 foot door on the port side (looking upstream). Two modular 20 inch square plexiglass cutouts are located near the middle of the test section on the top and bottom walls for wiring and tubing access. The motor is flanked by 4 feet long sound baffling sections immediately upstream and downstream. Schematics of LSWT are provided in Fig. 3.2 and detailed drawings of the contraction, including its geometric coordinates, are provided in Appendix A.

Empty tunnel velocity was determined by the pressure differential across a pair of static ports 11 inches upstream of the test section, and another pair 9 feet upstream. Both pairs were situated on the top and bottom tunnel walls at the spanwise centerline. Each pair was fed to a single tube at a T-junction and then directed to an Omega PX653-10D5V pressure manometer, with properties listed in Table 3.1. Assuming negligible losses through the inlet, the pressure differential between these two pairs of static ports was a measure of the bulk velocity through the tunnel. This pressure differential was calibrated against a pitot-static pressure for testing with the bump installed (see Section 3.2.1). Other pressure measurements (e.g. pitot-static and surface pressures) were acquired using one of two Baratron 226A manometers also listed in Table 3.1.

The total temperature of flow through the test section was measured using a 1/16 inch outer diameter, Type K thermocouple (accuracy 1.5°C [36]) extending 3 3/4 inches into the flow from the top wall, 6 1/4 inches downstream of the test section. Ambient pressure, temperature, and relative humidity (RH) were directly measured prior to each test using a Digi-Sense Traceable® Digital Barometer with an accuracy of ±4 mbar, ±0.4°C, and ±3% RH respectively. Density was calculated by the Ideal Gas Law, assuming a specific gas constant of 287.058 J/(kg K), and viscosity was calculated according to Sutherland's Law.

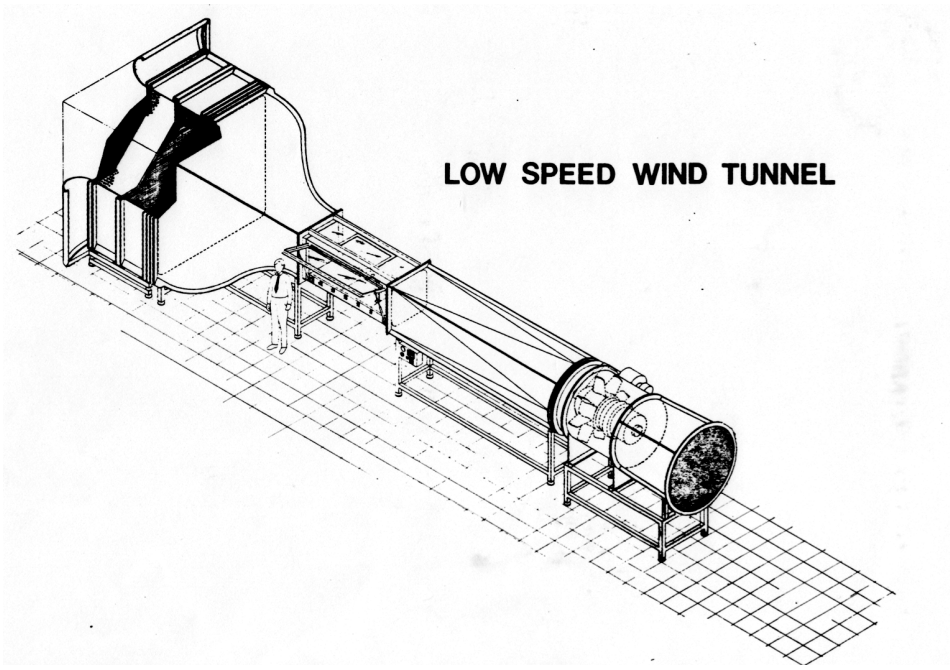

(a)

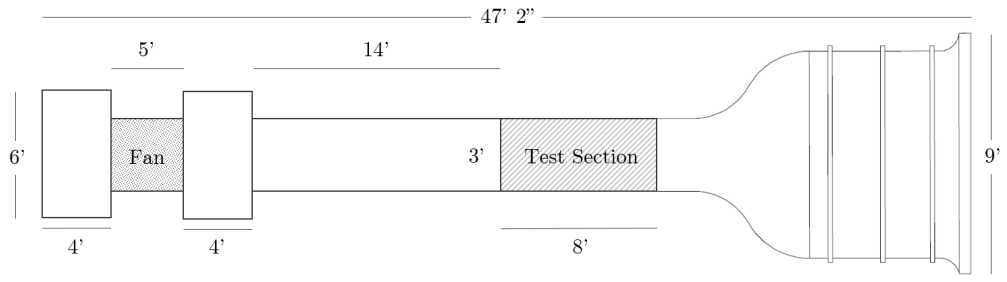

(b)

Figure 3.2: (a) Isometric, without sound baffling sections [35] and (b) top-down schematics of the Low-Speed Wind Tunnel (LSWT) at the University of Washington.

Table 3.1: Selected pressure sensor specifications. See Appendix A for full manufacturer data sheets.

	1	2	3
Manufacturer	Omega	Baratron	Baratron
Model	PX653-10D5V	226A	226A
Range (kPa)	0-2.49	± 2.67	± 6.67
Accuracy (Pa)	±6.2	±4.0	±8.0
Sensor Type	Capacitance	Capacitance	Capacitance
Thermal Zero (Pa/°C)	0.67	2.67	6.67
Thermal Span (%rdg/°C)	0.02	1.07	2.67

.

The sensors measuring the tunnel's interior temperature and velocity were connected to a National Instruments (NI) CompactDAQ data acquisitions (DAQ) platform. The Omega PX653 sensor was sampled continuously at 100 Hz through a NI9205 voltage input module, which featured a gain amplifier and a 16 bit analog-to-digital converter (ADC). The thermocouple was sampled continuously at 100 Hz using a NI 9213 temperature input module with a differential filter and 24 bit analog-to-digital converter. Other pressures measured with the Baratron 226A sensor(s) were acquired at 1000 Hz with an NI PCIe 6361 DAQ (16 bit ADC), through a NI BNC-2110 terminal block.

Manufacturer datasheets and calibrations for the equipment described above are located in Appendix A. Details on the equipment used in particle image velocimetry are found in Section 3.4. Additional information on instrumentation error and measurement uncertainties is documented in Section 3.5.

3.2 Speed-Bump and Splitter Plate

The speed-bump geometry was constructed out of epoxy and Alumina Trihydrate (ATH) powder by Steven Seim of Cyber Modelle, according to the specifications listed in Section 2.3. The bump was secured to a 3/8 inch aluminum backing plate using six bolts, providing a rigid structure. The mounted bump was fastened on either side longitudinally to two 3/4 inch thick MIC-6 aluminum plates, with a surface roughness of less than $0.5\mu m$ and a maximum deviation from flat of 0.005 inches, forming the splitter plate depicted in Fig. 3.3. The splitter plate was secured to two steel bars which were mounted in the tunnel through pin holes on each side-wall. The pin holes were arranged such that the plate could be moved vertically to test the effects of flow confinement, H. Six vertical stations were accessible: $H/L = 1/4, 1/3, 5/12, 1/2, 7/12, 2/3$, with $H/L = 1/2$ considered nominal. The width of the splitter plate, $L_b = 35.5$ inches, was slightly narrower than the tunnel width, $L = 36$ inches, for clearance during installation. The gaps on either side of the plate were filled with 3/4 inch wide, 1/4 inch thick Neoprene foam strips, forming an air-tight seal above and below the plate.

The 8 inch leading edge of the splitter plate was a 3D-printed, 10:1 modified super-ellipse designed to minimize transition across its surface. A thin strip of 240-grit sandpaper was placed at the juncture of the leading edge and upstream plate to fully trip the incoming boundary layer. The downstream plate featured a 12 inch adjustable trailing edge flap to control the stagnation location on the leading edge. Prior to testing at each level of confinement, the flap was adjusted until the stagnation point was slightly above the leading edge tip, determined by measuring the pressure differential across pairs of taps on the upper and lower surfaces of the leading edge.

A 1.5 by 4.5 inch cutout was machined into the aluminum plates upstream and downstream of the speed-bump at the spanwise centerline to fit a motorized pitot tube traverse for measurement of streamwise velocity profiles. The traverse featured a 0.02 inch outer diameter pitot probe with two static ports drilled near the base of the probe. The pressure

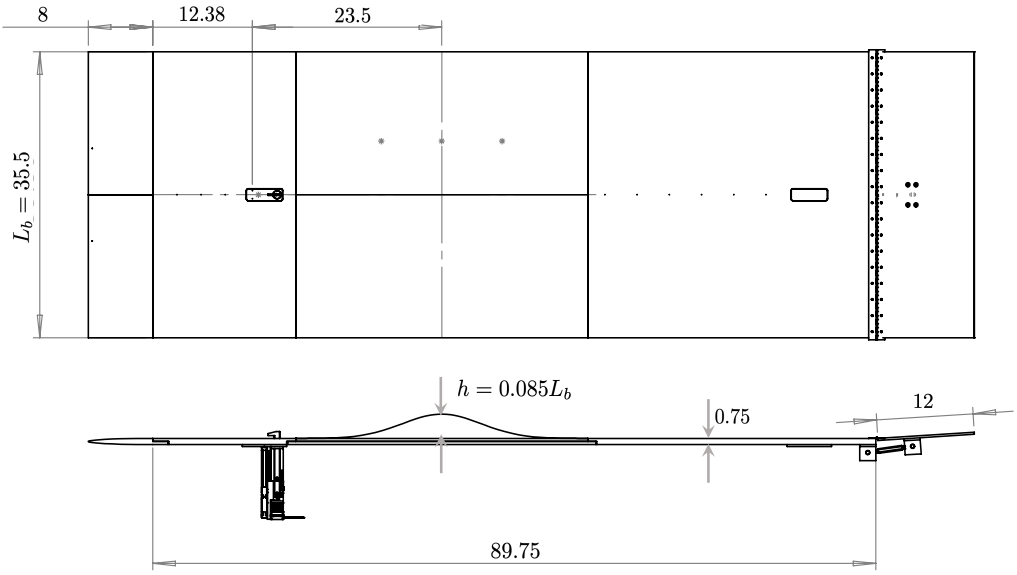

(a)

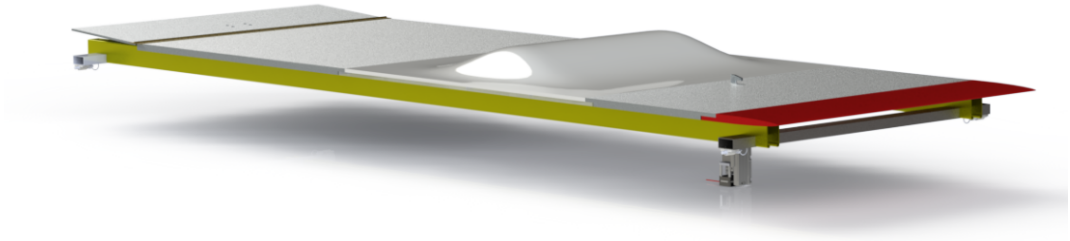

(b)

Figure 3.3: (a) Schematic and (b) CAD rendering of splitter plate and bump with removable pitot tube traverse installed. All dimensions in inches [7].

differential between the tube and the static ports was measured using a 20 Torr range Baratron 226A pressure sensor (see Table 3.1). A motor and encoder on the traverse allowed for high-resolution measurement of the inflow boundary layer at $x/L = 0.35$ downstream from the tripping device ($x/L = -0.65$ from the bump peak) as detailed in [7]. When the traverse was not in use, modular inserts were secured into the cutouts to form an airtight seal.

Surface pressure profiles over the splitter plate and speed-bump were obtained through 49 pressure taps of 1/16 inch outer diameter. Three taps were located upstream of the speed-bump on the spanwise centerline, 40 taps were located on the speed-bump, and six taps were on the downstream plate at the centerline. The taps located on the speed-bump were clustered downstream of the apex to offer increased resolution in the separated region. These taps were also located along symmetric planes to aid in the identification of correlated bias errors. A diagram of the tap layout the locations of the taps are listed in Section A.3 of the appendix.

One of two Baratron 226A pressure sensors, depending on the maximum pressure differential expected in a test, was employed to measure surface pressures. Table 3.2 lists the surface pressure test matrix and whether a 20 Torr or 50 Torr range sensor was used. Tap zero was routed directly to the reference side of the pressure sensor. The other 48 taps were routed to a Scanivalve solenoid prior to the pressure sensor such that each tap could be surveyed individually. The Scanivalve was controlled by an NI 9485 Relay Output module.

The pressure taps were connected to the sensor by 1/32 inch thick polyurethane tubing approximately 10 feet in length. High vacuum leak sealant was applied at the connection to the tap, along with a small zip tie. The tubes were bundled and taped to the tunnel walls with aluminum speed tape and routed outside of the tunnel through a 4 1/4 by 1 3/4 inch gap in the tunnel floor near the middle of the test section. The gap was completely covered with speed-tape, forming an air-tight seal.

A LabView virtual instrument (VI) managed the acquisition of data during a test. Tunnel conditions were measured continuously while each pressure tap was individually sampled for 20 seconds at 1000 Hz.

Table 3.2: Utilization of two Baratron 226A pressure sensors in surface pressure measurement by nominal Reynolds number and confinement. Sensor range in Torr.

	H/L			
$Re_L \times 10^6$	1/4	1/3	5/12	1/2
1.39	± 20	± 20	± 20	± 20
1.97	± 20	± 20	± 20	± 20
2.55	± 20	± 20	± 20	± 20
3.04	± 50	± 50	± 20	± 20
3.44	± 50	± 50	± 50	± 50

3.2.1 Velocity Calibration

The blockage in the test section generated by the splitter plate, speed-bump, and tubing invalidated the velocity measurement obtained by the static pressure differential through the contraction. While the velocity obtained from the traversable pitot tube was not susceptible to blockage, the traverse's wake disturbed the flow over the speed-bump when it was installed. Therefore, to accurately measure flow velocity for tests with the speed-bump and splitter plate installed, the static pressure differential across the contraction was calibrated to the pitot-static differential measured with the traverse. In this way, velocity could be measured both accurately and unobtrusively after the traverse was removed.

A linear calibration equation related the differential pressure from the pitot tube, ΔP_2, to the differential pressure measured from the static ports installed in the tunnel, ΔP_1.

$$\Delta P_2 = A + B(\Delta P_1) \tag{3.1}$$

Where coefficients A and B were given by a least-squares regression [37]:

$$A = \frac{\sum(\Delta P_1)^2 \sum \Delta P_2 - \sum \Delta P_1 \sum \Delta P_1 \Delta P_2}{N \sum(\Delta P_1)^2 - (\sum \Delta P_1)^2} \tag{3.2}$$

and

$$B = \frac{N \sum \Delta P_1 \Delta P_2 - \sum \Delta P_1 \sum \Delta P_2}{N \sum(\Delta P_1)^2 - (\sum \Delta P_1)^2} \tag{3.3}$$

with each summation evaluated through N test points obtained during in the calibration.

Calibration data was obtained by measuring both pressure differentials at ten increasing tunnel fan pitch settings. An example calibration curve under nominal conditions is depicted in Fig. 3.4. A calibration was measured at the beginning and end of each test day, and after the splitter plate was moved to a new level of confinement.

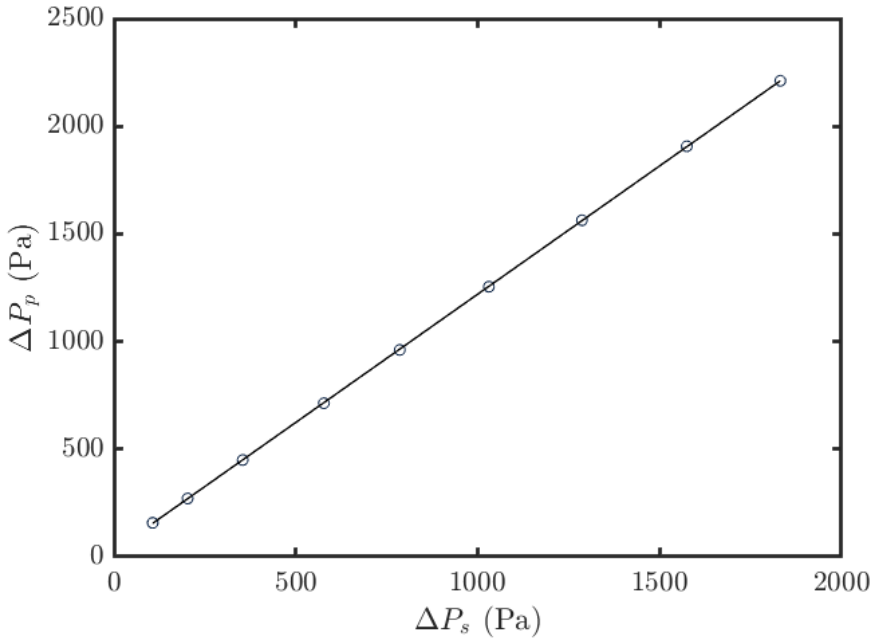

Figure 3.4: Nominal calibration between two differential pressures for velocity measurement (H/L = 1/2).

3.3 Pitot Rake

A pitot tube rake was designed to survey both flow uniformity and the tunnel's side-wall boundary layers at the inflow plane of the test section without the speed-bump and splitter plate installed. Thirty chamfered troughs were milled into a 1/4 inch thick by 2 inch wide, 1018 low-carbon steel bar with a length of 35 3/8 inches, which was slightly narrower than the tunnel width to allow for clearance during installation. Stainless steel pitot tubes with an outer diameter of 0.065 inches were placed into the troughs and secured with epoxy and pressure from a thinner steel plate fastened with screws above. The tubes extended 3 inches upstream to avoid the aerodynamic interference caused by the rest of the apparatus. Figure 3.5 shows the rake installed in the tunnel in two different wall configurations. Detailed drawings of the rake, including the locations of the pitot tubes, are provided in Section A.4 of the appendix.

The pitot tubes were biased towards one end of the rake, with the first ten tubes spaced as close as possible. The next ten tubes were logarithmically spaced outwards to a conservative estimate of the maximum expected boundary layer thickness in the test section, $0.1L$. The remaining ten tubes were linearly spaced to the tunnel centerline.

The rake could be positioned in one of seven locations along each wall to survey the entirety of the tunnel inflow plane, with the exception of the radiused corners. The end of the apparatus on the opposite wall from the pitot tubes was connected to the pins above and/or below the plane of the rake in order to prevent rotation. The plungers at the non-pitot end of the apparatus were tightened such that the pitot-end was flush with the wall. The rake was also capable of being mounted in downstream pin holes on the port and starboard walls for measurement of flow uniformity and boundary layer profiles at the outflow plane.

The pitot tubes were connected to a Scanivalve/Baratron 226A arrangement in a similar fashion as the speed-bump pressure taps (see Section 3.2), with the tunnel static ports 11 inches upstream of the test section (about 5 inches ahead of the pitot tubes) used as a reference. Using LabView, each pitot tube was sampled for 7 seconds at 1000 Hz.

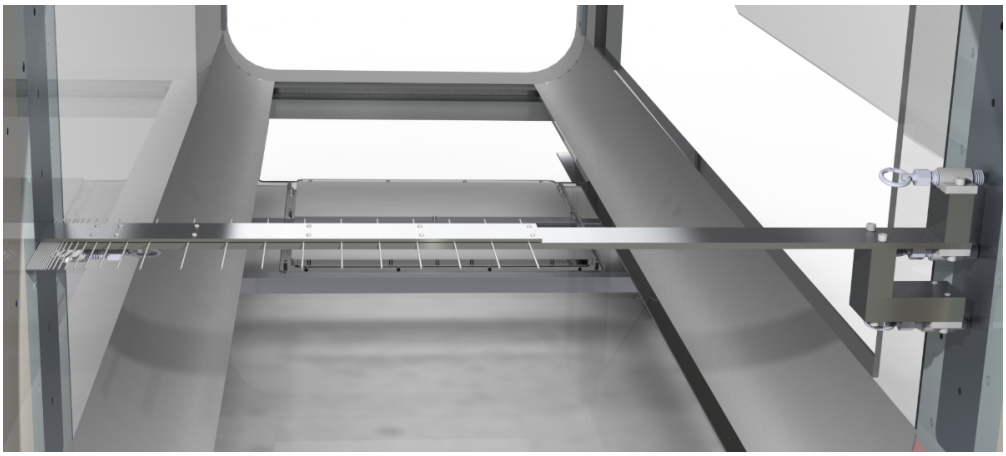

(a)

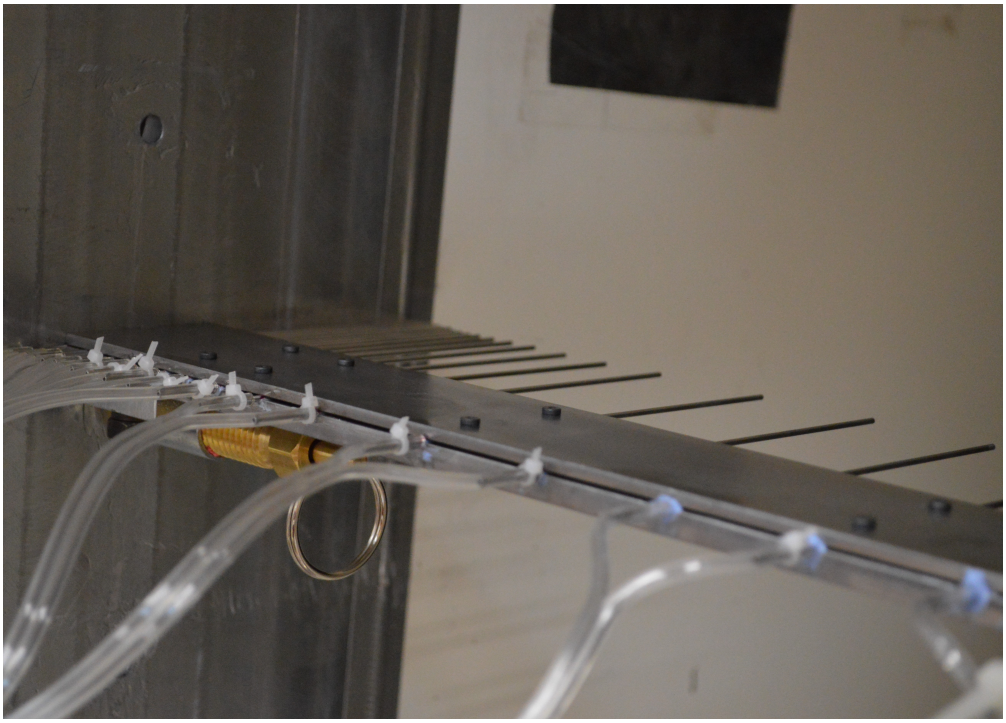

(b)

Figure 3.5: (a) CAD rendering of rake installed for measurement of the starboard side-wall (polyurethane tubing not depicted) and (b) close-up photo of the logarithmic region of tubes for measurement of the port side-wall.

3.4 Particle Image Velocimetry

3.4.1 Equipment

Instantaneous velocity fields near the inflow plane and over the speed-bump were experimentally measured using particle image velocimetry. Using a camera, the locations of smoke particles in the plane of a pulsating laser sheet were captured in pairs of image frames recorded in quick succession. With time between the two frames known, a cross-correlation of pixel intensities (i.e. seeded particle locations) between the pair yielded the velocity vector field observed at that moment in time. Obtaining many image pairs, and hence many instantaneous velocity vector fields, allowed for the calculation of the mean and fluctuating components of velocity, and thus many important turbulent quantities. Since the measurement was external to the wind tunnel, PIV offered an observation of the flowfield without interference from sensors or other equipment.

Planar, double-frame, double-exposure PIV was used in this study to capture non-time-resolved (i.e. statistically independent) snapshots of the flowfield in the streamwise-wall-normal plane of the flow with the speed-bump and splitter plate installed in the test section. The PIV system was traversable and capable of measuring a wide range of the flowfield without losing calibration. Mean flow velocity, in-plane turbulent kinetic energy, Reynolds stress distributions, and their uncertainties were some of the products of PIV used in this study to gain a clearer understanding of the flow's dynamics, particularly in the separated region, and to corroborate results from the other experimental techniques employed.

The interior of the Aeronautics Laboratory was seeded with theatrical smoke particles using a Chauvet DJ Hurricane 1800 Flex fog machine, capable of a 25,000 cfm output [38]. Black Label Ray Tracer premium fog fluid, a mixture of de-ionized water and glycols, was used as the seeding material, producing particles approximately 0.1 mm in diameter. The fog machine was nominally set to produce smoke at 15,000 cfm for six seconds, every two minutes. The timing was adjusted as needed to qualitatively maintain a constant seeding density over the duration of a test.

(a) (b)

(c) (d)

Figure 3.6: Equipment used for PIV measurements of the speed-bump. (a) Chauvet Hurricane 1800 Flex fog machine [38], (b) Imager sCMOS camera [39], (c) EverGreen 200 ICE and laser head [40] and (d) LaVision PTU X timing unit [41].

A single 5.5 megapixel Imager scientific complementary metal-oxide-semiconductor (sCMOS) camera was used to capture the images. This camera was specifically designed for PIV applications by specializing in low light imaging with large signal variations while offering high temporal and spatial resolution over large fields of view illuminated by a laser sheet [39]. The sensor was 2560 by 2160 pixels, with a pixel size of 6.5 μm^2. Data was transferred via a fiber optic cable to a Camera Link high-speed frame grabber. Images were recorded directly to RAM and offloaded to a hard disk simultaneously, allowing for a high rate of acquisition without any speed limitations associated with writing directly to the hard disk.

Two fields of view were measured. A larger 8.76 by 7.39 inch field of view (LFOV) was captured using a Nikon Micro Nikkor 60 mm focal length lens to study uniformity and large-scale features of the flow field. A Nikon 200 mm focal length lens was used to measure the boundary layer and separated region in greater detail with a smaller 2.62 by 2.21 inch field of view (SFOV). The lens apertures were set to an f-stop of f/8 and f/11, yielding average particle diameters of 4 and 2 pixels for large and small fields of view respectively.

Illumination was provided by a Quantel EverGreen 200 dual cavity, solid-state, neodymium-doped yttrium aluminum garnet (Nd: YAG) dual-pulsed laser. The laser was rated for 200 mJ at a wavelength of 532 nm and a repetition rate of up to 15 Hz [40]. The system consisted of a laser head connected to an integrated cooling and electronics (ICE) power supply unit. The laser beam was directed out of a single aperture in the laser head and through a 90 degree steering mirror pointed downwards at the splitter plate. The beam passed through adjustable optics and, finally, through a diverting lens to project the beam into a sheet of light.

The laser optics were adjusted such that the light sheet was as thinnest at the splitter plate, and as streamwise as possible. The laser sheet thickness, measured with burn paper, was 0.0345 inches for large field-of-view testing, and 0.045 inches for small fields of view. The speed-bump and splitter plate were spray-painted black in order to minimize the laser's reflection on the surface.

The camera lenses were focused using a calibration target placed coincident with the laser

sheet. For the 60mm lens, a dual plane 204 by 204 mm (LaVision Type 204-15) calibration target was used. A smaller 58 by 58 mm dual plane (LaVision Type 058-5) target was used for the 200 mm lens. The targets featured a grid of circles with size and separation known by the acquisition software, which automatically calculated the calibration. The resulting scale factors were 292.1 and 975.4 pixels/inch for large and small fields of view respectively.

The timing and synchronization of the camera and laser were controlled within 10 ns by a LaVision Programmable Timing Unit X (PTU) [41]. BNC cables linked the PTU to the flash lamp and Q-switch trigger inputs for each laser cavity on the laser ICE, and to a timing input on the camera. The PTU was connected via USB to a computer to interface with the acquisition software.

The camera and laser head were mounted to a three-axis traverse in order to allow for image acquisition at various locations over the domain without losing calibration. The laser head was fastened to a 24 by 36 inch Vere optical breadboard and flanked by two aluminum standoff boxes. A 72 by 55 inch right-angle frame was secured on top of the boxes and to hang the camera on the starboard side of the wind tunnel.

The traversing apparatus featured five motorized Velmex BiSlides moving in three orthogonal directions. A 15 inch lead-screw driven slide, powered by a Vexta Type 23T1 single shaft stepper motor, was secured to one of the legs of the right-angle frame. The camera was mounted to the carriage of the slide to traverse in the wall-normal axis. The optic table was secured to the carriages of two parallel 40 inch lead-screw driven slides, powered by a Vexta Type 34T1 double shaft stepper motor, allowing for movement in the spanwise axis while maintaining a constant distance between the camera and the laser sheet. Finally, the parallel lead-screw driven slides were mounted to the carriages of two parallel 100 inch belt driven slides, powered by a Vexta Type 34T1 10:1 geared stepper motor, for movement in the streamwise axis. The entire traversable apparatus was secured to the top of the wind tunnel, as shown in Fig. 3.7.

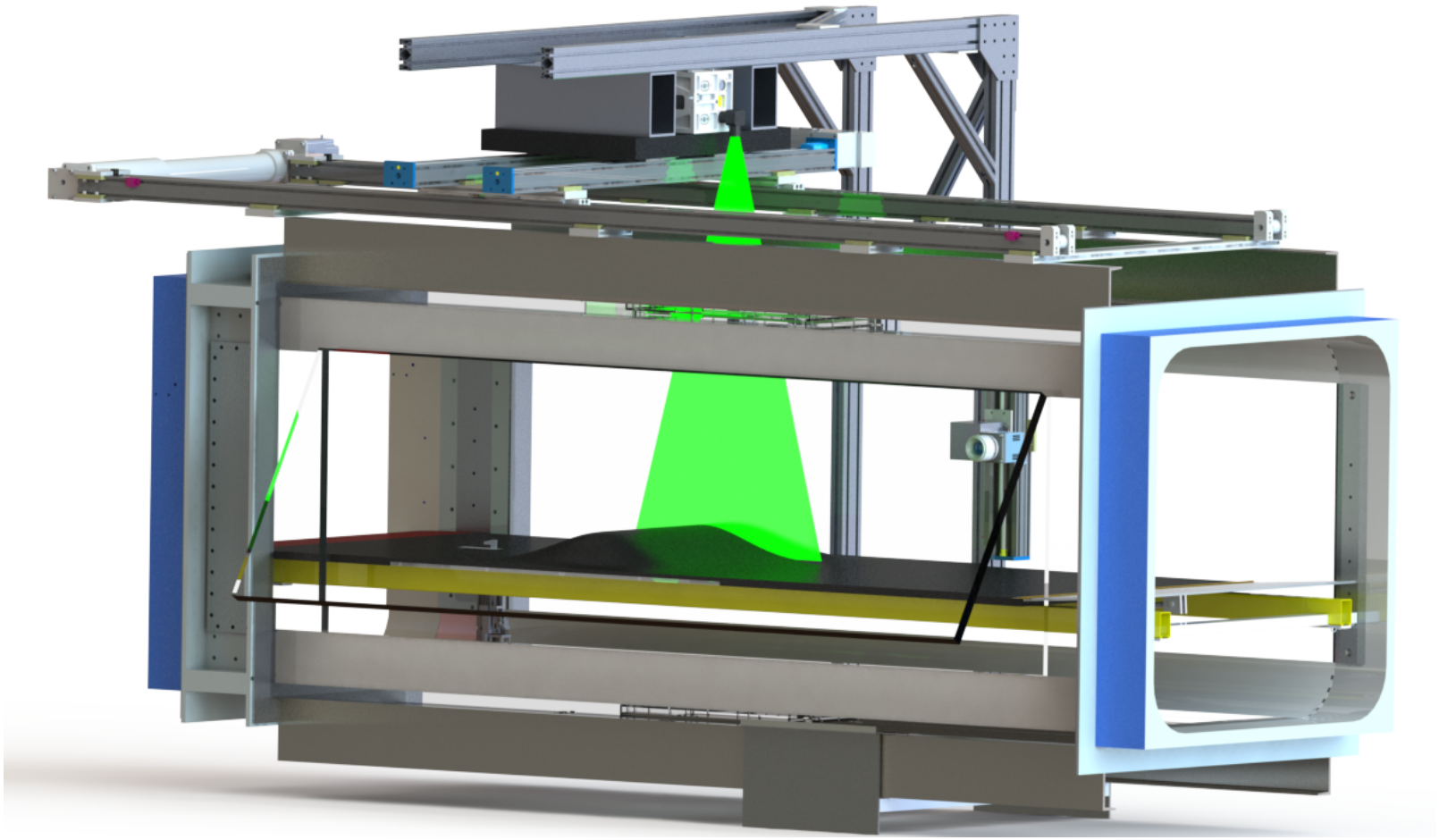

Figure 3.7: Isometric CAD rendering of the traversible PIV apparatus installed on top of the Low-Speed Wind Tunnel.

The motors of the three slides were powered and controlled by a master VXM-2 stepper motor controller and slaved VXM-1 controller. Both controllers interfaced to a computer via an RS-232 protocol. A custom script was written in LabView to control the position of the center of the camera's field of view. The lengths of the slides and the geometry of the wind tunnel restricted the PIV measurement domain to -0.74 $\leq$ x/L $\leq$ 1.18, -0.24 $\leq$ y/L $\leq$ 0.24, and -0.03 $\leq$ z/L $\leq$ 0.38. Limit switches on each slide prevented travel beyond this range.

Additional information on the equipment described above, including manufacturer data sheets, calibrations for the laser and camera, and laser burn marks, is listed in Section A.

3.4.2 Acquisition

Images near the inflow plane were captured at five spanwise locations at the streamwise location of previously obtained centerline boundary layer velocity measurements using a pitot tube traverse (x/L = -0.65). Data sets near the speed-bump were acquired at a series of streamwise locations along spanwise planes closely corresponding to locations of surface pressure taps. Only the small field of view measurements utilized the wall-normal-axis motorized slide to follow the contour of the bump; large fields of view were acquired at a constant vertical position. The streamwise overlap between adjacent fields of view was 30% to allow for a compilation of statistical flowfields over the speed-bump. Locations of the overlapping frames are illustrated in Fig. 3.8 for both large and small field of view measurements.

All image acquisition related events were controlled and monitored in DaVis 10 by LaVision. A host program, ran in LabView from a separate computer, monitored and recorded tunnel conditions and controlled the position of the camera/laser traverse. Prior to a test, each axis of the traverse was positioned at its motor-end limit, and its motor encoder was zeroed. Then, the host program parsed through a list of traverse coordinates supplied as an input by the user. The traverse always arrived at a station from the upstream direction in order to minimize any position error caused by slack in the motor. After the traverse was positioned at each coordinate, the host program sent a TTL signal to the PTU, triggering the start of image acquisition in DaVis for that station. After acquisition at that station

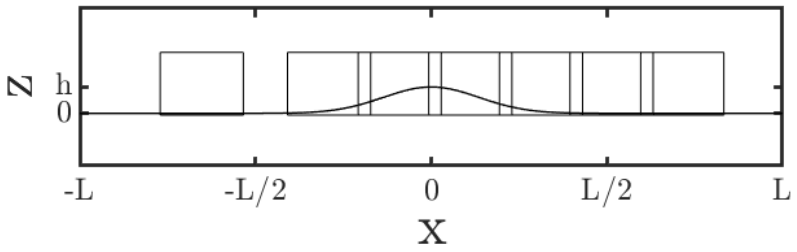

(a)

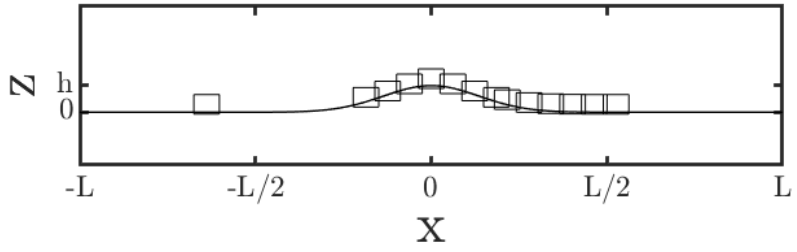

(b)

Figure 3.8: Acquired PIV fields of view along a spanwise plane with (a) large $\sim 9\ in^2$ field of view (60mm lens) and (b) small $\sim 2\ in^2$ field of view (200mm lens).

was complete, the host program commanded the traverse to move to the next coordinate, and the process repeated for all stations specified by the user. In this way, the entire image acquisition process was automated after initialization.

One thousand image pairs were acquired at each station to ensure adequate statistical convergence of the mean flow properties. Images were acquired at the maximum frequency of the laser, 15 Hz. The time between laser pulses, dt, was set such that the maximum particle displacement was limited to 12 pixels. Thus,

$$dt = \frac{12}{1000aU} \tag{3.4}$$

where a is the calibration scale factor in pixels/mm, and U is the calibrated freestream velocity of the flow in m/s.

Table 3.3: Time between frames, dt (μs), in double-frame, double-exposure PIV for a maximum particle displacement of 12 pixels.

Nominal velocity (m/s)	Small FOV	Large FOV
20	7.04	44.7
30	5.59	29.8
40	5.33	22.4
60	4.16	14.9

The time between laser pulses for the nominal velocities tested in both large and small fields of view (FOV) are listed in Table 3.3. A summary of the PIV acquisition parameters for this study is listed in Table 3.4. Note that the calibrated velocities used in the calculation of dt were slightly greater than the nominal velocities listed in the table.

3.4.3 Reduction

In addition to image acquisition, DaVis 10 was also used for image pre-processing and initial data reduction. After acquisition, the images were initially subjected to a stabilization routine to mitigate the effects of vibrations caused by the wind tunnel. All images in the set were shifted relative to a stationary artifact (e.g. curved wall reflection) in the first image of the set. Afterwards, a time-filter was applied to each image at every pixel based on the minimum intensity measured at that pixel in a 50 image range. This subtraction effectively removed most background artifacts, however some non-steady features (i.e. reflections from seeding residue) remained near the wall. Finally, portions of the image below the surface of the speed-bump and splitter plate were manually masked from the image by defining a region below the line of pixels which measured intensities approximately equal to the well-depth of the camera sensor, indicating the surface reflection of the laser.

The images were then analyzed using a multi-grid, multi-pass, cross-correlation method

	Small FOV	Large FOV
Measurement FoV (in)	(2.62 x 2.21)	(8.76 x 7.39)
Image pairs per station	1000	
Acquisition rate (Hz)	15	
Calibration (pixels/in)	975.4	292.1
Light sheet thickness (in)	0.0345	0.045
Lens aperture	f/11	f/8
Particle image diameter (pixels)	≈ 4	≈ 2
Particle size (mm)	0.1	
Maximum particle image displacement (pixels)	12	

Table 3.4: Summary of PIV measurement parameters for small and large fields of view.

with iterative image deformation (see [42]). A perspective correction was applied within this step per the calibration listed in Tab. A.16 in the appendix. Two initial passes employed 128 x 128 pixel correlation widows with 50% overlap. Final passes utilized a 32 x 32 pixel interrogation window with Gaussian weighting and 75% overlap.

Vectors were validated using a correlation level filter ($r < 0.8$) and with 5 passes of a normalized median filter in a universal outlier detection scheme with 11 x 11 vector windows (see Westerweel [43–45]). A final anisotropic denoising filter was applied using values of the instantaneous velocity uncertainty field (filter strength of 3, max kernel size of 21 x 21 vectors) as described in Wieneke [46]. These filters reduced errors while preserving true flow fluctuations.

Since the measurement fields of view overlapped, a single composite flowfield encompassing all of the streamwise stations measured on a spanwise plane could be generated from the statistical quantities calculated at each station. The post-processed instantaneous vector fields generated in DaVis were exported to MATLAB™ for further processing and to stitch

the flowfields together.

Within MATLAB™, the edges of each vector field were trimmed by 5 vectors in order to compensate for poor correlations in this region. Additionally, the coordinate system of the vector fields at each station was transformed to the global coordinate system of the tunnel (see Sec. 4) using the location of the speed-bump's apex from the raw images of that data set. Since this was known in the global coordinate system, the absolute position of the frame containing the apex could be determined given the pixel location of the apex and the scale factor of the image calibration. The coordinates of the other frames were determined relative to the apex using the coordinates list prescribed to the traverse, assuming the traverse moved a relative distance between stations with negligible error. The statistical quantities of the corrected vector fields were then computed at each station and added to a scattered interpolant object. The reduction scripts used for these operations are provided in Appendix D.

For plotting, a linearly spaced grid constructed from the minimum and maximum measured streamwise and vertical coordinates was created. An alpha-shape containing all streamwise and vertical coordinates in the statistical fields was generated to trim the regions of the plotting grid that were either outside of the measurement domain or masked. Composite flowfields were generated using the trimmed plotting grid that was supplied to the scattered interpolant object for each individual variable of interest. An illustrated example of the workflow is depicted in Fig. 3.9.

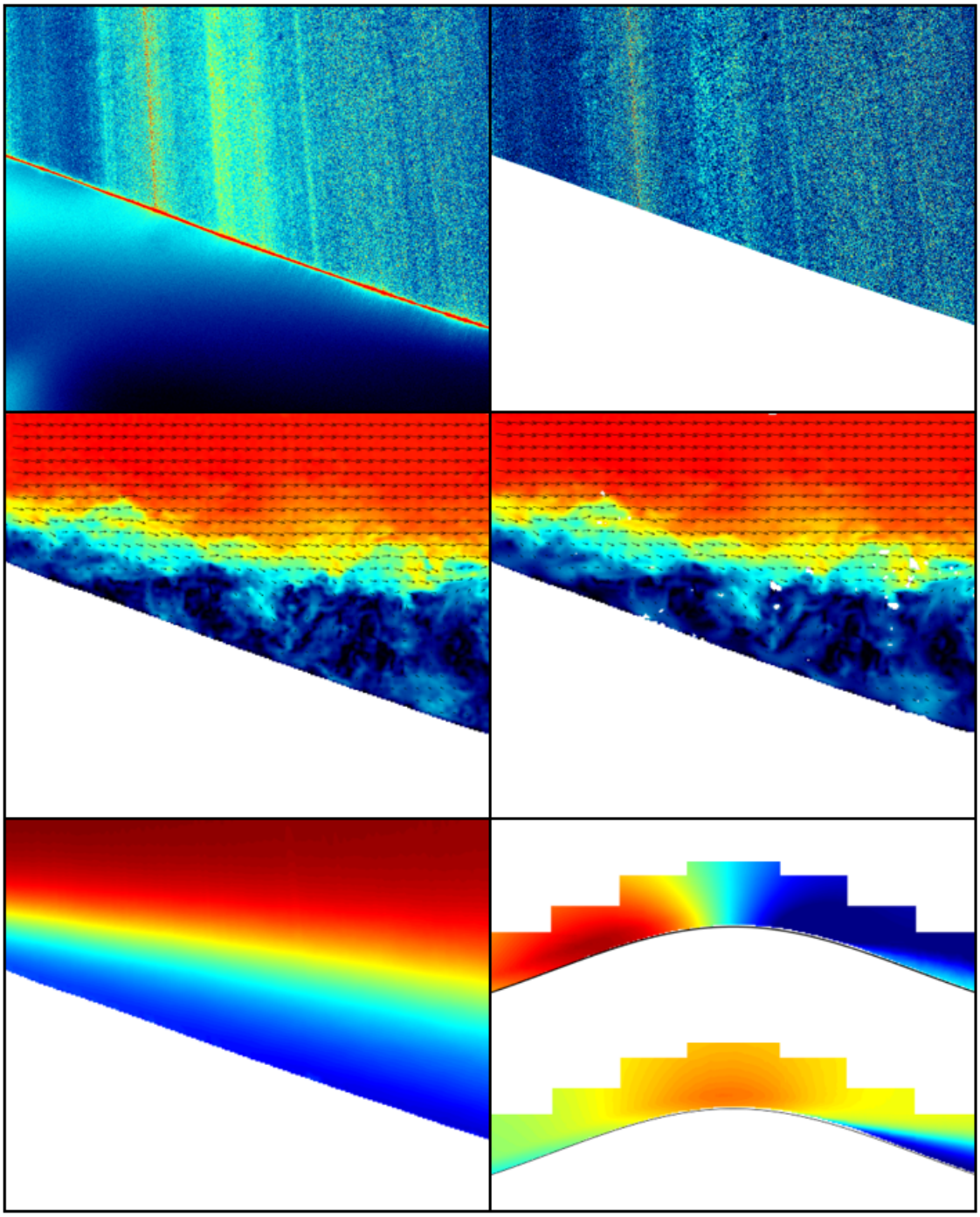

Figure 3.9: PIV reduction workflow example ($Re_L = 1.87 \times 10^6$, y/L = 0.11, x/L = 0.19). From top left to bottom right: raw image, background subtraction and wall masking, instantaneous vector field, filtered vector field, averaged scalar field, composite flowfield.

3.5 Treatment of Uncertainty

This study adopted the American Institute of Aeronautics and Astronautics (AIAA) standard for assessment of experimental uncertainty in wind tunnels, as described in AIAA S-071A [47]. Both random and systematic components of uncertainties were considered for nearly all measured and derived quantities of the experiment. The random component of uncertainty, or precision limit, in a measured quantity, k, (e.g pressure, temperature) was taken to be the standard deviation of the mean:

$$\delta_{k_{ran}} \equiv \frac{\sigma_k}{\sqrt{N}} \tag{3.5}$$

where σ_k is the standard deviation of the time series and N is the number of samples obtained in the measurement. The random component of uncertainty was calculated for the entire measurement system (i.e. sensor, signal conditioner, data acquisition, and reduction).

The systematic component of uncertainty, or bias limit, in a measured quantity was taken to be the manufacturer's specified accuracy of the sensor.

The absolute uncertainty of a measured quantity was taken to be the quadratic sum of its bias and precision limits:

$$\delta_k \equiv \sqrt{(\delta k_{ran})^2 + (\delta k_{sys})^2} \tag{3.6}$$

The bias limit of a derived quantity, q, (e.g. velocity, coefficient of pressure) incorporated the absolute uncertainties of its constituent variables, k, l, m, etc., propagated in accordance with Eq. 3.7. A random component of uncertainty for a derived quantity was only calculated if multiple tests were conducted at the same test point.

$$\delta_q = \sqrt{\left(\frac{\partial q}{\partial k}\delta k\right)^2 + ... + \left(\frac{\partial q}{\partial m}\delta m\right)^2 + (\delta q_{ran})^2} \tag{3.7}$$

For PIV measurements, the systematic component of uncertainty for post-processing and filtering operations was estimated within DaVis 10 using a statistical analysis of the correlation between image pairs. The second image of the pair was dewarped onto the first using the computed displacement vector field. Differences between the two images due to measurement noise were represented by asymmetric correlation peaks. Uncertainty was then estimated with a statistical analysis of the pixel intensity differences and their effect on the correlation peaks. Additional information on this method is provided in Wieneke [48].

The results from PIV presented in this report were statistical properties of time series (i.e. mean and fluctuating components of the flow) and only the random component of uncertainty was considered. Propagation of random uncertainty into derived statistical quantities is detailed in Sciacchitano and Wieneke [49], and listed for each quantity presented in this report in Appendix C.

All error sources added in quadrature were assumed to be independent and uncorrelated. For a measurement system, the errors of the data acquisitions unit, machine precision error, and other minor error sources were considered negligible. Additionally, the calculated uncertainty of a sensor was assumed to be at least the resolution of the sensor, although the resolution had no contribution to the calculated uncertainty. All uncertainty values were given as plus-or-minus ($\pm$) at 95% confidence and were reported to one significant digit unless the leading digit was 1 (in which case, two significant digits were reported).

Additional information on the uncertainty of measured and derived quantities, including derivations, is located in Appendix C.

Chapter 4
RESULTS AND DISCUSSION

The results of this study will be presented in two parts. The products of experimental characterization that act as boundary conditions (i.e. inputs) to the numerical model will be discussed first (e.g. measurement of the as-built test article, assessment of inflow uniformity, and side-wall boundary layers). Then, relevant system responses (i.e. model outputs) will be detailed (e.g. surface pressure profiles and flowfield statistics).

The coordinate system adopted for these results is referenced to the top dead center of the speed-bump, with x, y, and z as the streamwise, spanwise, and vertical coordinates respectively. For side-wall velocity profiles, a capitol Z denotes the wall-normal coordinate. Spatial coordinates are non-dimensionalized either by the speed-bump length, $L_b = 35.5$ inches, the tunnel width, $L = 36$ inches, or the speed-bump height, $h = 3.0175$ inches.

When available, data products are presented along with their total uncertainty. A general description of the treatment of uncertainty adopted in this study is given in Section 3.5, with a detailed description offered in Appendix C.

To keep with the spirit of this section as a results overview, not all data is presented in this section. Ancillary data that contributes to the documentation of the experiment is provided in Appendix E.

4.1 As-Built Speed-Bump Geometry

The speed-bump test article was measured using a Creaform HandySCAN$^{\text{TM}}$307 digital scanner with a resolution of 0.0016 inches. A geometric mesh containing approximately 1.5 million points was generated from the scanner and then linearly interpolated to a uniformly spaced grid centered on the speed-bump. The grid was trimmed 0.6 inches from the edges

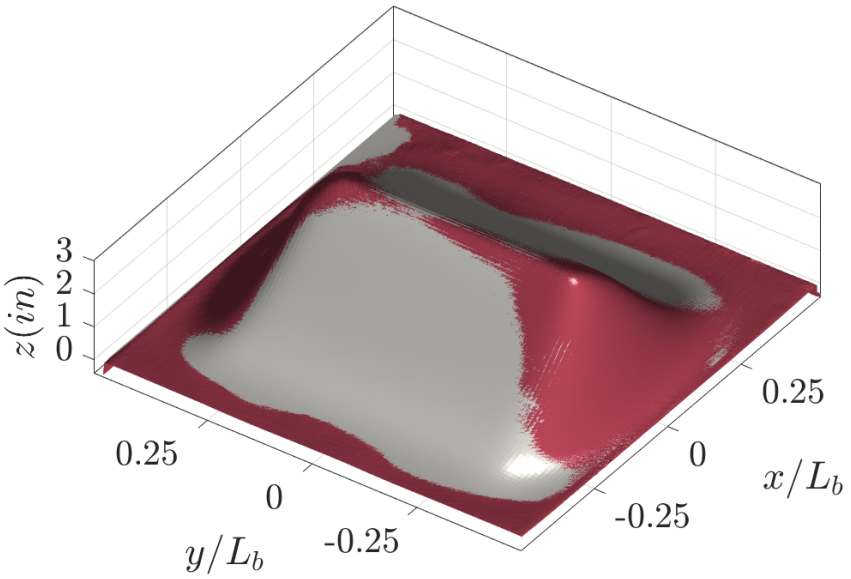

Figure 4.1: As-built speed-bump geometric deviation from mathematical definition. Isometric view of mathematical definition (grey) and actual measurement (red). Flow from bottom left to top right.

to remove scanning distortions. The interpolated grid was directly compared with the mathematical definition of the speed-bump, where the error, ϵ, was taken to be the difference. Since the points from the scanner were arbitrarily scaled, the grid was iteratively translated, rotated, and scaled within a routine to minimize the total error. The result of this analysis is plotted in Figs. 4.1 and 4.2.

The root-mean-square of the measured error from each grid point was 0.018 inches ($\epsilon/h = 0.6\%$), with a maximum error of 0.057 inches observed at the edges of the model closest to the tunnel side-walls. Deviations from the mathematical definition were approximately symmetric about the model centerline. A slight upward flaring was observed on all edges of the speed-bump, accounting for most of the error. This flaring is thought to be caused by differential curing of the epoxy and ATH powder due to the thinness of the model near the

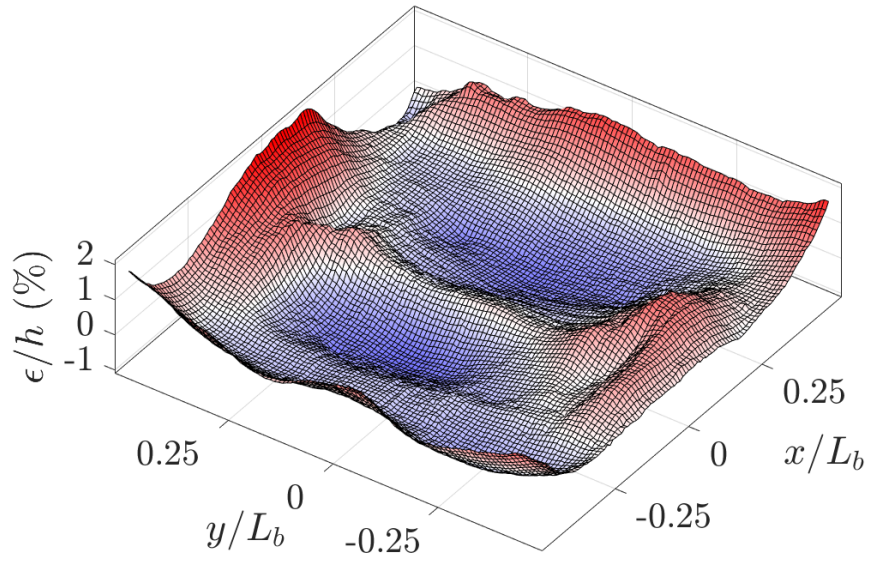

(a)

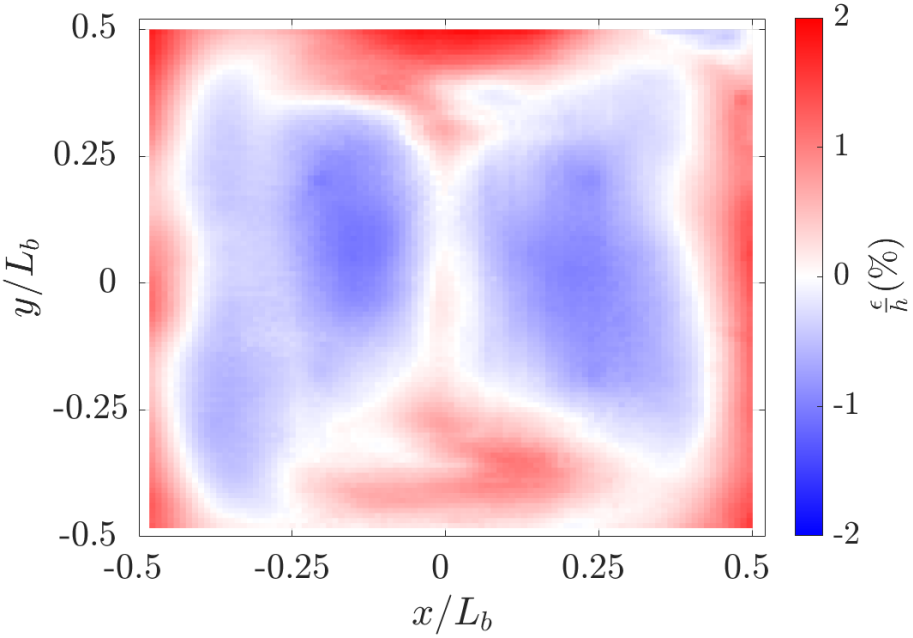

(b)

Figure 4.2: (a) Isometric (flow from bottom left to top right) and (b) top-down (flow from left to right) heat maps of as-built speed-bump error.

edges. Shimming and speed-tape helped ensure a smooth junction between splitter plate and speed-bump geometry, despite the deviation. The height of the actual geometry was slightly lower than prescribed on the streamwise faces, on the order of 1% of the speed-bump height. The small and symmetric deviations were assumed to have a negligible effect on the flowfield, although time constraints prevented testing the speed-bump in its symmetric orientation to confirm this.

4.2 Inflow Survey

The validation framework of Oberkampf and Smith [1] prescribes a survey of the experimental facility's inflow quality. This is a property of the wind tunnel and does not involve the speed-bump geometry. According to the authors of the framework, providing data *without* a test article installed allows the CFD analyst to concentrate on the flow in the empty test section and adjust the physical modeling assumptions for the mathematical model as needed prior to simulating more complicated flow physics. Accordingly, a pitot rake was used to measure flow uniformity and side-wall boundary layers at the inflow plane of the test section, without the speed-bump and splitter plate installed. Empty-tunnel freestream turbulence values were previously measured and discussed in Sarwas [5].

While the pitot rake measurements satisfy the experimental facility attribute, a survey of inflow quality *with* the test geometry installed was required for characterization of the boundary and initial conditions of the flow problem. For these measurements, PIV was employed to measure flow uniformity and boundary layers over the splitter plate.

The inflow survey characterizing the experimental facility is discussed first, followed by the survey with the speed-bump installed.

4.2.1 Empty-Tunnel Inflow

Flow velocity at the inflow plane of an empty test section was surveyed at n = 30 wall-normal locations (see Appendix A.4) from the wall to tunnel centerline using a pitot rake at 20, 40, and 60 m/s nominal tunnel settings. The rake was positioned at one of 28 stations (seven

locations along each wall), providing information on boundary layers and mean flow uniformity across the x/L = -l.0 inlet plane, with the exception of the radiused corners. Different statistical measures of the data were used for presentation and normalization depending on the sample size. The mean was only considered for large samples (e.g. pressures/velocities measured at each pitot tube over the duration of a test). The median was considered for collections of those mean values. For example, mean velocity profiles at each station were normalized by the median of the mean velocities measured from the innermost ten tubes at that station, $\widetilde{U}_{\infty,s}$, in order to account for slight variations in tunnel velocity settings between tests:

$$\widetilde{U}_{\infty,s} = med\left(\{\overline{U}_{(i,s)}\}_{i=21}^{n}\right) \tag{4.1}$$

Mean uniformity flow fields at the inflow plane are shown in Fig. 4.3 for 20, 40 and 60 m/s nominal freestream velocities. Each black dot in these figures represents the location of a pitot tube; data between the dots were linearly interpolated. For the uniformity fields, all mean velocities were normalized by a single freestream velocity: the median of all stations' freestream velocity:

$$\widetilde{U}_{\infty_{vel}} = med\left(\{\widetilde{U}_{\infty,s}\}_{s=1}^{28}\right) \tag{4.2}$$

The velocity variation at each station, σ_U, normalized by the mean velocity measured at each station, $\overline{U}_{(i,s)}$, is also illustrated in Fig. 4.3. While the total component of uncertainty was calculated for each velocity, only the precision component is depicted in this figure to highlight regions of the inflow plane that experienced significant flow fluctuations. The bias component was very sensitive to minute discrepancies in tunnel velocity between runs (see Fig. C.1), and was significantly greater than the variation caused by flow features.

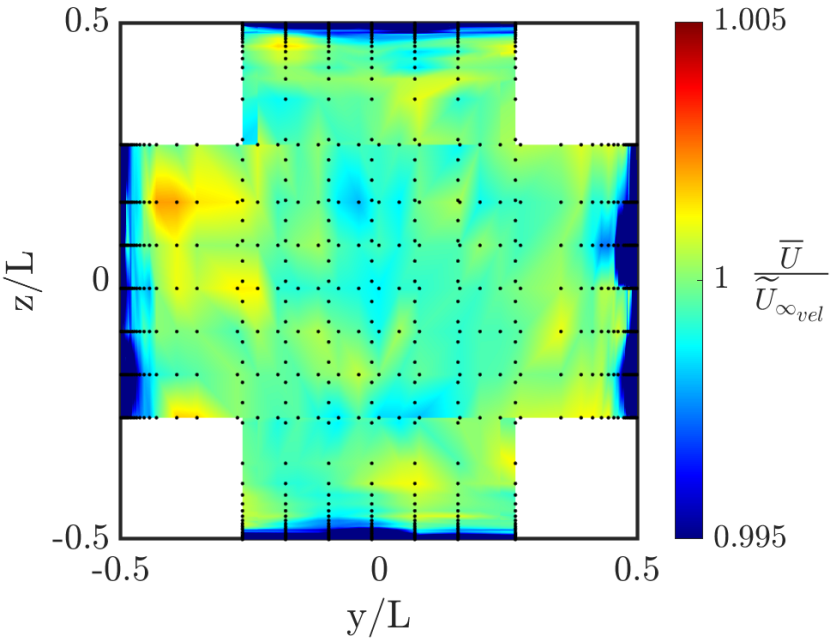

(a) $Re_L = 1.40x10^6$ (20 m/s)

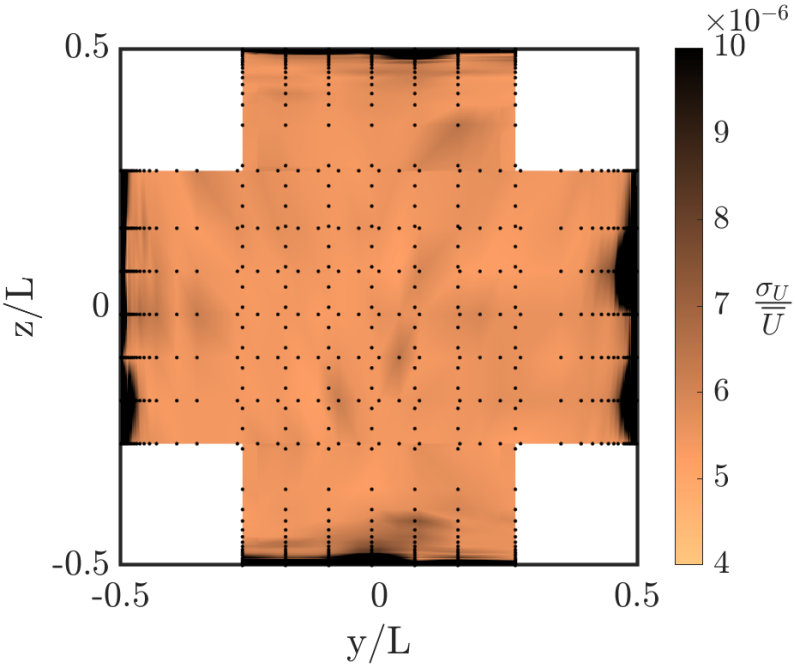

(b) $Re_L = 1.40x10^6$ (20 m/s) variation

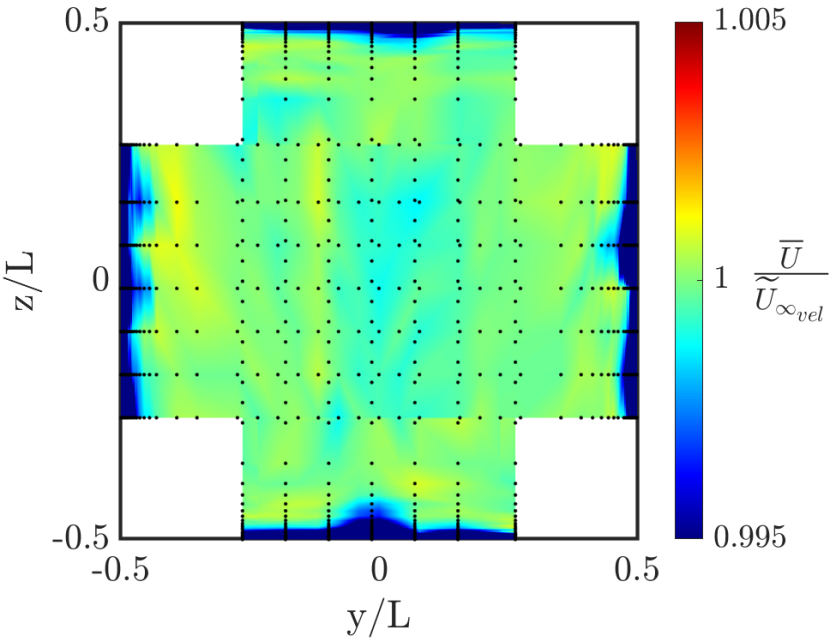

(c) $Re_L = 2.55x10^6$ (40 m/s)

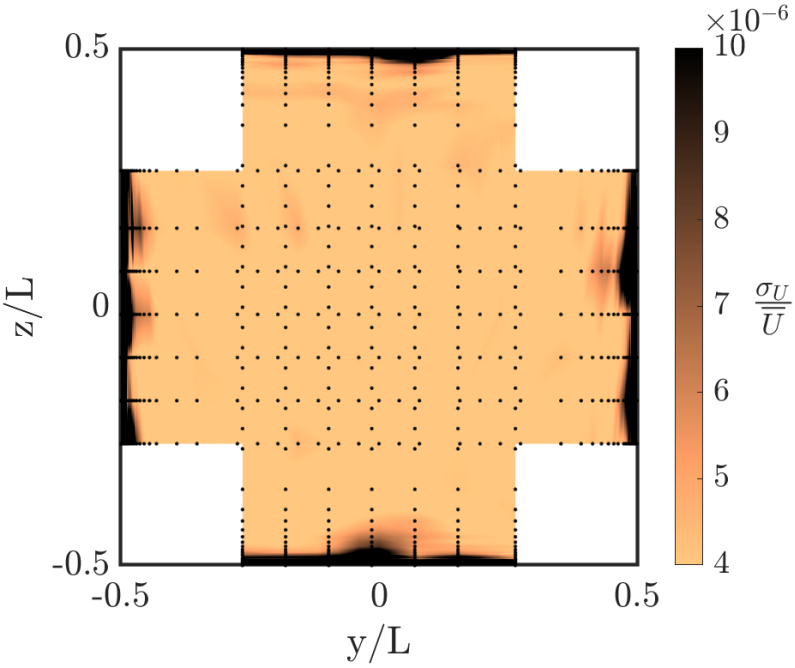

(d) $Re_L = 2.55x10^6$ (40 m/s) variation

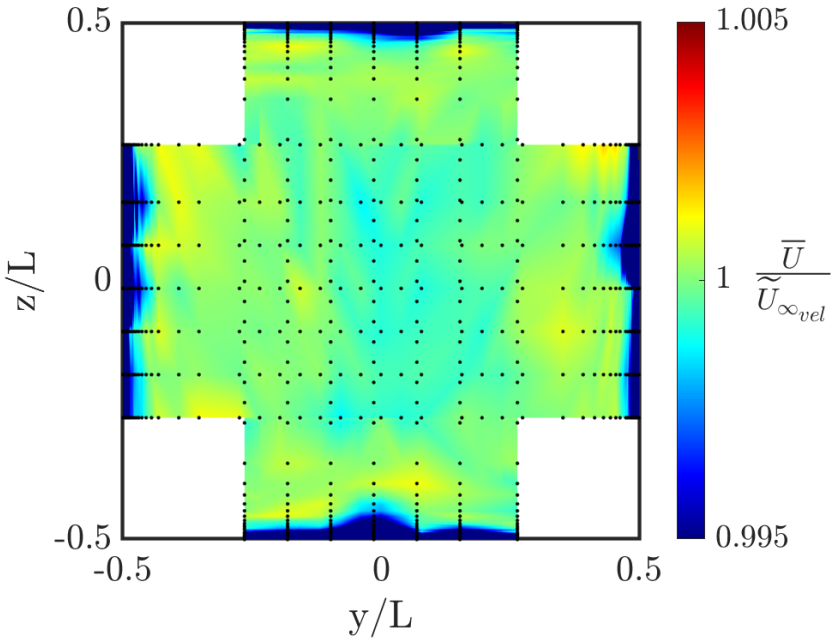

(e) $Re_L = 3.57x10^6$ (60 m/s)

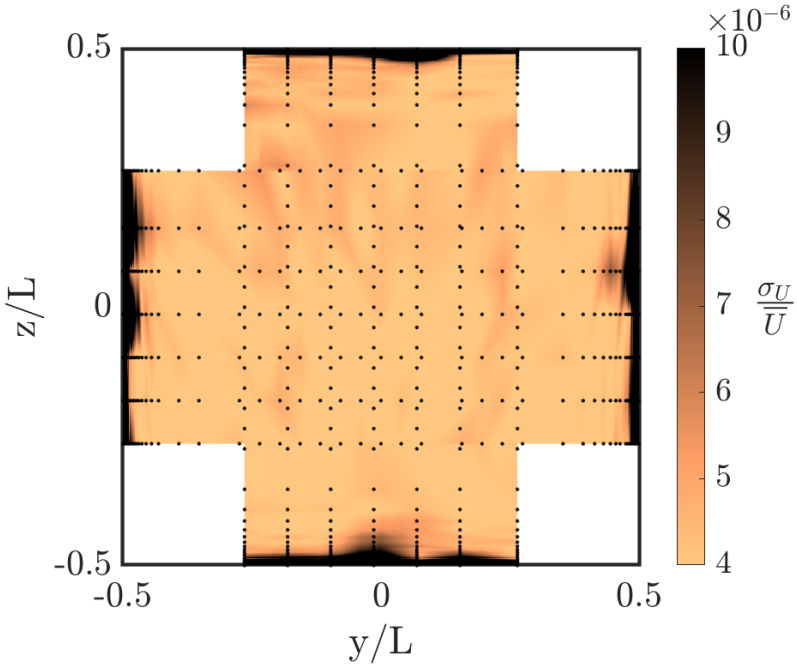

(f) $Re_L = 3.57x10^6$ (60 m/s) variation

Figure 4.3: Mean empty tunnel inflow uniformity and variation looking upstream (x/L = -1.0).

Table 4.1: Non-uniformity statistics of empty tunnel inflow plane core (x/L = -1.0, -0.26 $\leq$ y/L, z/L $\leq$ 0.26) measured using pitot rake.

Nominal Velocity (m/s)	Max (%)	Standard Deviation (%)
20	0.20	0.06
40	0.13	0.04
60	0.12	0.04

Non-uniformity statistics for the tunnel inflow core (-0.26 $\leq$ y/L, z/L $\leq$ 0.26) are given in Table 4.1. Overall, the empty tunnel core inflow demonstrated excellent uniformity for all nominal velocities, with a maximum deviation of 0.2% at 20 m/s. These variations improved to 0.13% and 0.12% at 40 and 60 m/s, respectively. Small leaks between the pitot tubes and the pressure transducer were likely culprits of some spurious mean velocity measurements, as only a slight directional bias towards the port-side wall was observed within the core region. Tubes with known leaks yielded abnormally high values in the mean with little variation and were repaired as needed.

The twenty wall-adjacent and logarithmically spaced pitot tubes on the rake allowed for the measurement of boundary layer velocity profiles along each wall at the inflow plane. The boundary layer thickness, δ, was considered to be the wall-normal distance where the velocity reached 99 percent of the freestream velocity. This distance was determined by linear interpolation between the wall-normal position of the first pitot tube to record a velocity at or greater than 99% of the freestream velocity, Z_i, and the position of the next tube closest to the wall.

For a given nominal velocity of the tunnel, all boundary layer velocity profiles were normalized by the median thickness calculated from all 28 stations, $\widetilde{\delta}_{vel}$. Recall that the mean velocity measured at each pitot tube, $\overline{U}_i$, was normalized to its corresponding freestream velocity at that station, $\widetilde{U}_{\infty,s}$.

As illustrated in Fig. 4.3, some variation in velocity was observed in the near-wall region along each wall. Velocity profiles for the bottom wall at $Re_L = 3.57x10^6$ (60 m/s) are depicted in Fig. 4.4, where two adjacent boundary layer profiles deviate greatly from the other stations and each other. Each wall had one or two such anomalous boundary layer profiles, often at multiple nominal velocities (which were acquired sequentially). This trend was repeatable after reinstallation of the rake for a few of these anomalous stations. The cause of the differences at these locations is not well understood but may be due to slight geometric imperfections in the tunnel contraction, although no such imperfections were visually apparent.

A profile representing each wall at a nominal velocity was determined using the median of all mean velocities measured at each station along the wall, $\widetilde{U}_s$, normalized by the median of the freestream velocities from each station along the wall, $\widetilde{U}_{\infty,s}$. Since the wall-normal

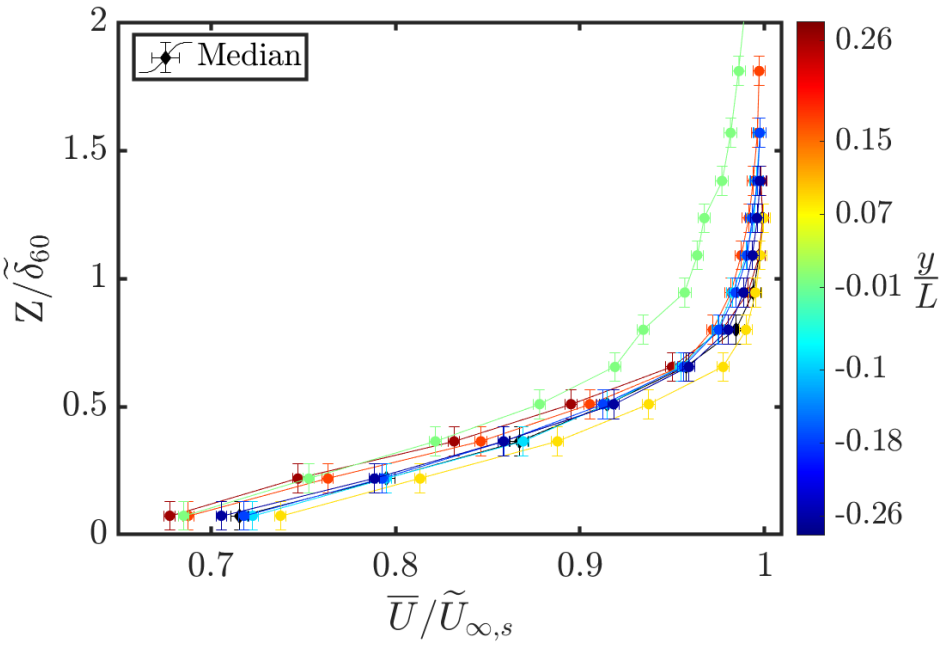

Figure 4.4: Empty-tunnel boundary layer profiles on bottom wall at $Re_L = 3.57x10^6$ (60 m/s), x/L = -1.0.

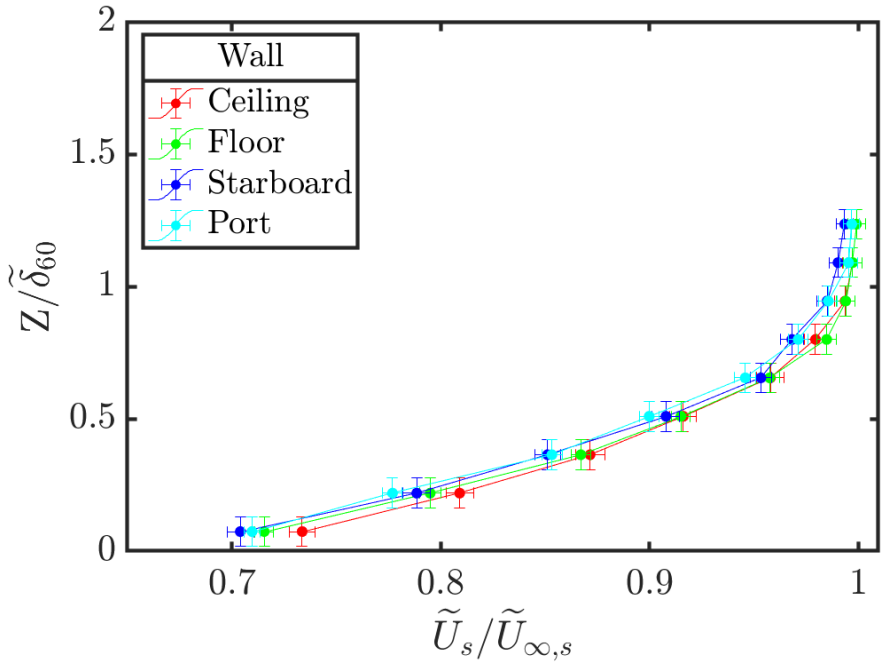

Figure 4.5: Median boundary profiles of all stations for each side-wall at $Re_L = 3.57x10^6$ (60 m/s), x/L = -1.0..

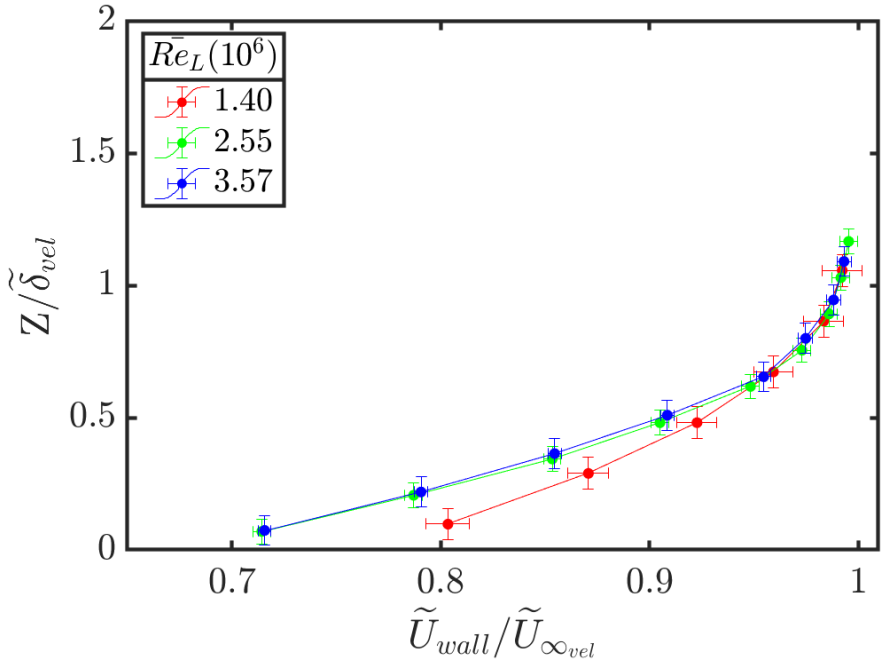

Figure 4.6: Empty-tunnel median boundary layer profiles of all walls for each nominal tunnel velocity, x/L = -1.0.

Table 4.2: Median empty-tunnel boundary layer properties and their corresponding uncertainty at x/L = -1.0.

Nominal Velocity, m/s	20	40	60
$\widetilde{U}_{\infty_{vel}}$ ($\pm\delta_{\widetilde{U}_{\infty_{vel}}}$), m/s	25.3 (0.2)	46.3 (0.2)	65.4 (0.2)
$Re_L \times 10^6$	1.40	2.55	3.57
$Re_h \times 10^5$	1.17	2.14	2.99
$\widetilde{\delta}_C$ ($\pm\delta_{\widetilde{\delta}_C}$), in	0.25 (0.02)	0.40 (0.03)	0.41 (0.03)
$\widetilde{\delta}_S$ ($\pm\delta_{\widetilde{\delta}_S}$), in	0.39 (0.06)	0.47 (0.04)	0.49 (0.04)
$\widetilde{\delta}_F$ ($\pm\delta_{\widetilde{\delta}_F}$), in	0.35 (0.02)	0.49 (0.04)	0.48 (0.04)
$\widetilde{\delta}_P$ ($\pm\delta_{\widetilde{\delta}_P}$), in	0.34 (0.03)	0.49 (0.03)	0.45 (0.03)
$\widetilde{\delta}_{vel}$ ($\pm\delta_{\widetilde{\delta}_{vel}}$), in	0.34 (0.02)	0.47 (0.02)	0.45 (0.03)

distance was non-dimensionalized by $\widetilde{\delta}_{vel}$, the ordinates of the profile points are consistent between all station profiles for a particular nominal velocity, including the median profile. For each wall, the median profiles correspond very closely, as seen in Fig. 4.5. Consequently, the inflow is thought to be quite symmetric between all four walls despite a few small localized disturbances. A summary of median boundary layer properties and their corresponding uncertainty at each nominal velocity is provided in Tab. 4.2. The median boundary layer thickness for the ceiling, starboard wall, floor, and port wall is given by $\widetilde{\delta}_{C,S,F,P}$ respectively. A complete listing of profiles for each station, including the median profiles for all walls, is provided in Appendix E.

Finally, overall profiles for each wall were determined by considering the median of the median velocities at each wall, normalized by Eq. 4.2. The profiles for each nominal velocity tested (20, 40, 60 m/s) are depicted in Fig. 4.6. Nearly identical profiles were seen for 40 and 60 m/s, with a shallower near-wall velocity gradient observed at 20 m/s. While the rake was only able to resolve the outer layer, it can be reasonably inferred from the shape of

the 20 m/s profile that the side-wall boundary layers were not sufficiently tripped near the inflow plane at this velocity, with complete transition occurring somewhere between 20 and 40 m/s.

4.2.2 Model-Installed Inflow

Additional inflow surveys were conducted using PIV to evaluate flow uniformity above the splitter plate. A 2.62 x 2.21 *in* field of view was positioned upstream of the speed-bump with the splitter plate surface toward the lower boundary of the image. Images were captured in five spanwise locations, y/L = -0.181, -0.097, 0, 0.111, and 0.1875, which were selected to closely align with planes of surface pressure taps while offering the best image quality. The center of the frames was positioned at x/L = -0.638, near the location of near-wall velocity measurements previously obtained using a pitot tube traverse.

To assess flow symmetry across the inflow plane, the mean velocity within a 0.08 in^2 region near the center of the frame and above the boundary layer was calculated at x/L = -0.65 for each spanwise location and compared in Fig. 4.7. For consistency, these mean velocities were normalized to the median of the set, $\widetilde{U}_{\infty_{vel}}$. The inflow was uniform within 0.02%, with a slight bias toward the port-side wall. This observation lies well within the conventionally assumed random error limit of PIV (0.1 pixels or ∼0.66% for this case). The cause of this bias is not well understood but could be due to a slight drift in ambient conditions over the duration of the test ($\Delta U_\infty \approx 0.05$ m/s, $\Delta T approx 2^\circ$ K), a perspective distortion between images at different spanwise locations, or a true flow asymmetry.

A well-developed boundary layer was observed for all velocities at all spanwise locations. The velocity and in-plane turbulent kinetic energy (TKE) fields are illustrated for the centerline station at 60 m/s in Fig. 4.8. The depicted fields were trimmed from their original size since the freestream quantities were generally constant above z/h = 0.15. The in-plane TKE field was normalized by an estimate of the friction velocity from inflow boundary layer surveys previously obtained using a traversable pitot tube [7]. Note that the in-plane TKE fields do not account for the unknown out-of-plane fluctuations, and therefore underestimate

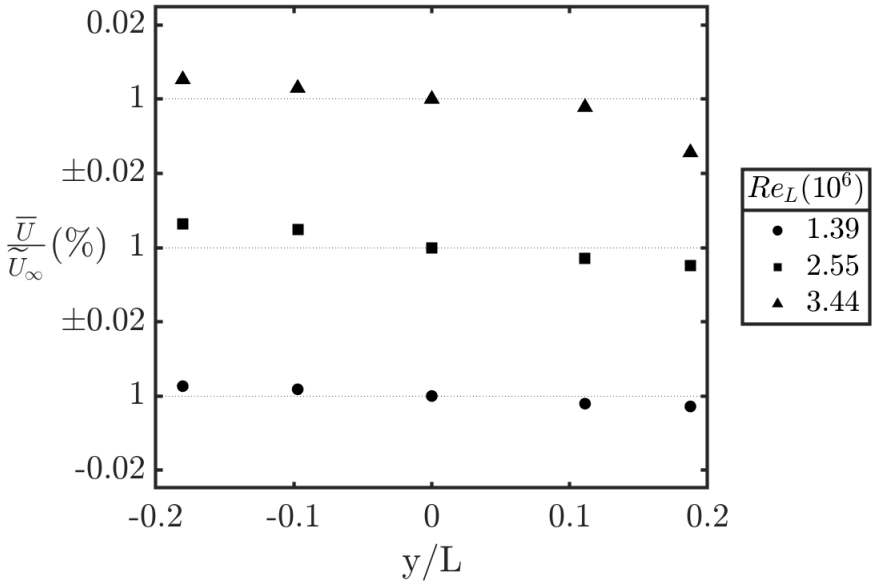

Figure 4.7: Mean velocity near (x/L, z/h) = (-0.65, 0.36) over spanwise extent of splitter plate inflow. H/L = 1/2.

the full TKE of the flow.

In Fig. 4.8a, the initial adverse pressure gradient encountered in the streamwise direction is illustrated by the slight increase in boundary layer thickness as x/L increases. Correspondingly, the turbulent energy in the boundary layer appears to grow in this adverse pressure gradient region. The uncertainty fields closely resemble the distribution of in-plane turbulent kinetic energy, as flow fluctuations increase. Distorted regions of the flow were observed approximately 0.5 mm from the wall ($z^+ = 70$) where the laser's unsteady reflection interfered with the image, indicated by higher magnitudes of uncertainty.

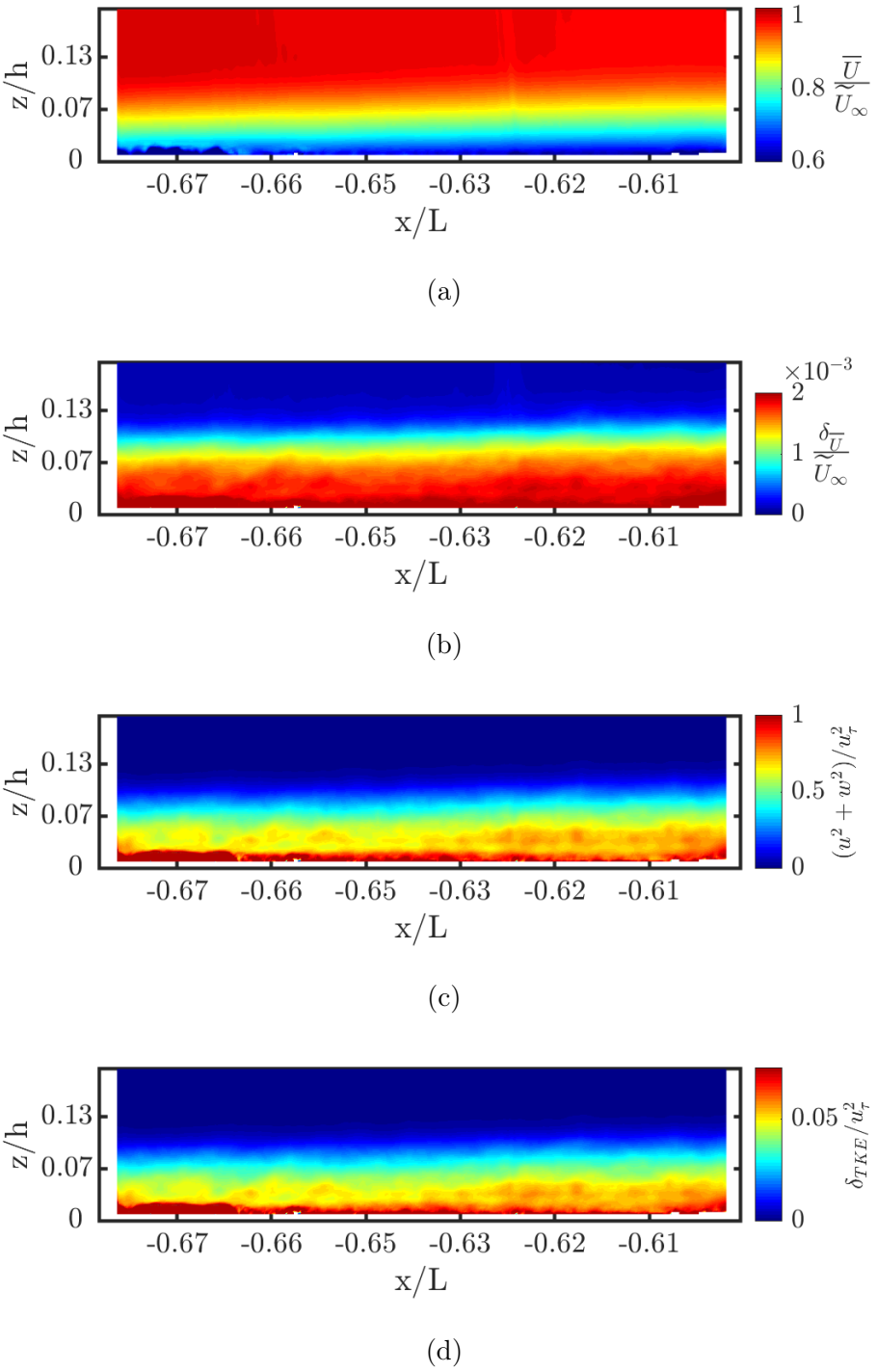

Figure 4.8: Mean (a) velocity, (b) velocity uncertainty, (c) in-plane TKE, and (d) in-plane TKE uncertainty distributions for the inflow boundary layer above the splitter plate. y/L = 0, $Re_L = 3.44 \times 10^6$ (60 m/s), H/L = 1/2.

Table 4.3: Median model-installed boundary layer properties on the splitter plate at x/L = -0.65, H/L = 1/2. (†: see Williams et. al. [7])

Nominal Velocity, m/s	20	40	60
$\widetilde{U}_{\infty_{vel}}$, m/s	24.1	45.3	63.3
$u_\tau{}^\dagger$, m/s	0.92	1.67	2.43
$Re_L \times 10^6$	1.39	2.55	3.44
$Re_h \times 10^5$	0.75	1.40	1.93
$\widetilde{\delta}_{Plate}$, in	0.35	0.32	0.31

Splitter plate boundary layer velocity and in-plane turbulent energy profiles at x/L = -0.65 are illustrated for 20, 40 and 60 m/s in Fig. 4.9, with median properties tabulated in Table 4.3. The wall-normal coordinate was normalized by $\widetilde{\delta}_{Plate}$ per each nominal velocity. For all velocities tested, the boundary layers show good agreement with each other with no discernible bias towards one side of the tunnel. Median profiles for each velocity are presented in Fig. 4.10. The similarity of the velocity profiles affirms that, unlike the side-wall boundary layers, the splitter-plate boundary layer was sufficiently tripped at 20 m/s. The decrease in near-wall turbulent energy for the higher Reynolds number is not intuitive, however, and may the result of the filtering of turbulent features caused by low image resolution near the wall.

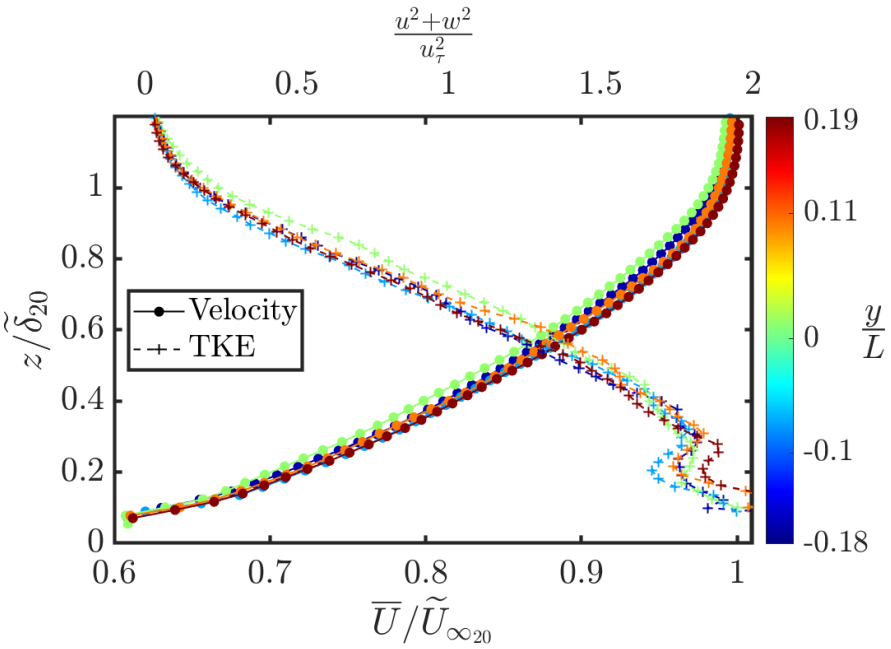

(a) $Re_L = 1.39 \times 10^6$ (20 m/s)

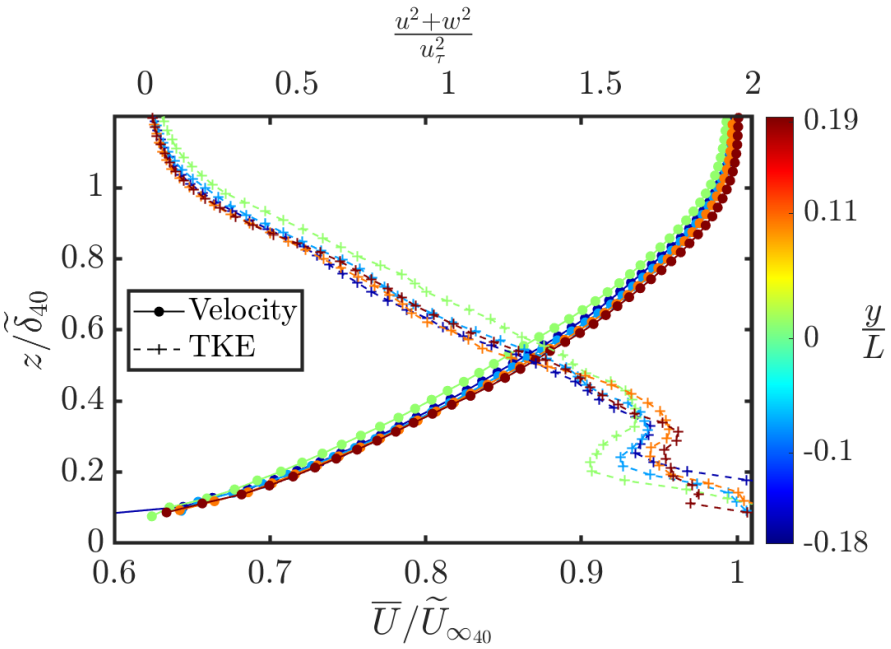

(b) $Re_L = 2.55 \times 10^6$ (40 m/s)

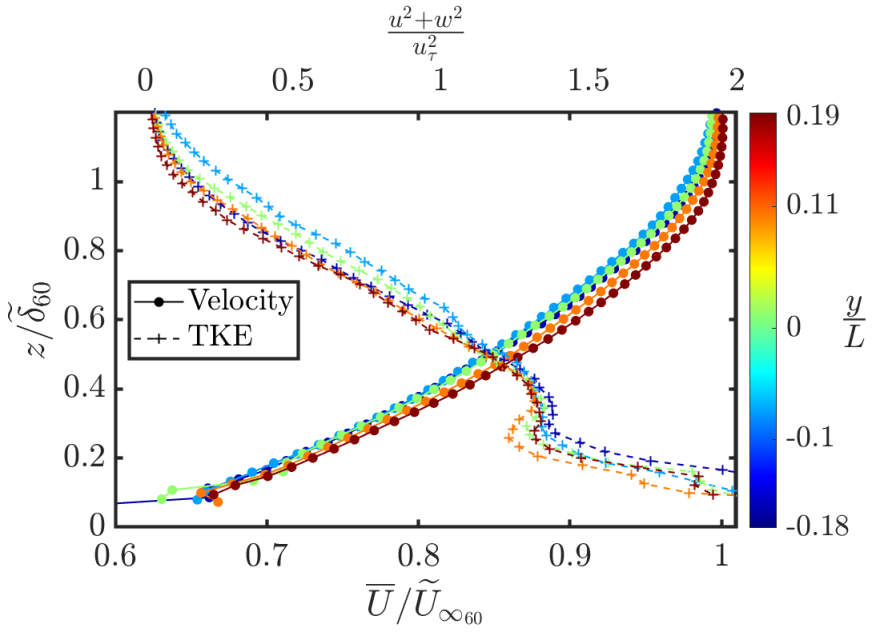

(c) $Re_L = 3.44 \times 10^6$ (60 m/s)

Figure 4.9: Splitter plate inflow velocity and in-plane TKE profiles at x/L = -0.65, H/L = 1/2.

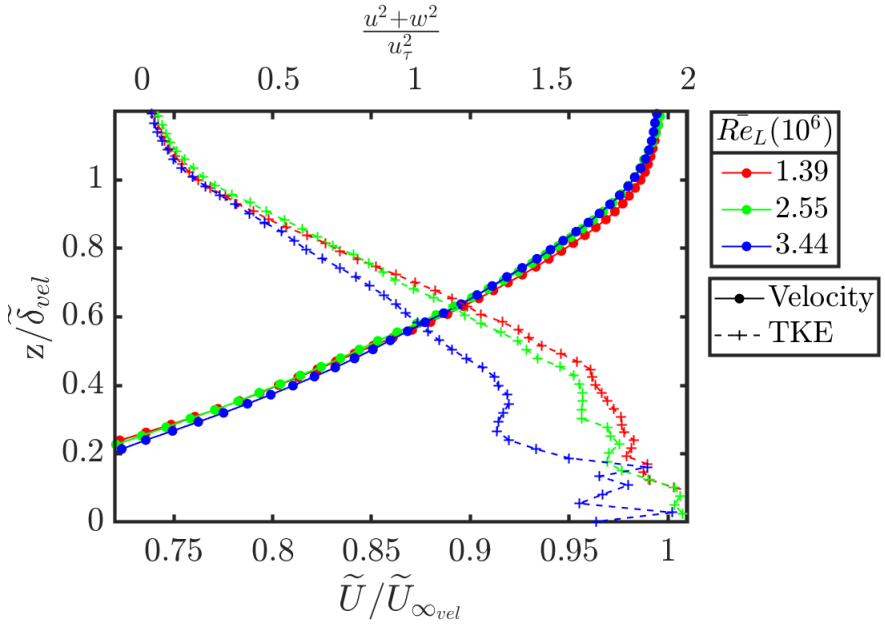

Figure 4.10: Median splitter plate inflow velocity and in-plane TKE profiles at x/L = -0.65, H/L = 1/2 for various Reynolds numbers.

4.3 Surface Pressure

A preliminary survey of surface pressure distributions over the speed-bump was previously acquired and presented in Williams et al. [7] and Samuell [6]. These measurements have, up until recently, been the primary method of comparison between simulations and experiments for this validation test case. As a result, these measurements were repeated to incorporate measurement and uncertainty improvements, and to examine three additional levels of flow confinement $H/L = 5/12, 1/3, 1/4$. Measurement improvements include the use of a lower range pressure transducer at lower velocities for increased accuracy (see Table 3.1), improved tunnel velocity calibration (see Section 3.2.1), and a quadrupled sample time (20 seconds per tap at 1000 Hz) for greater statistical convergence of taps in the highly-variable separated region.

Surface pressures were recorded at 48 locations on the splitter plate and over the speed-bump. These taps are located at a series of streamwise planes at symmetric spanwise locations. See Appendix A.3 for the full list of pressure tap locations. Surface pressures are presented as non-dimensional coefficients of pressure, C_P. While tap zero (x/L = -0.91) was used to reference the pressure differential measurement, the pressure coefficients are referenced to the pressure differential at tap one (x/L = -0.83), i.e.:

$$C_{P_x} = \frac{2RT\Delta P}{P_a U^2} = \frac{2RT\left((P_x - P_0) - (P_1 - P_0)\right)}{P_a U^2} = \frac{2RT(P_x - P_1)}{P_a U^2} \tag{4.3}$$

Coefficients measured along the streamwise and spanwise centerlines are shown in Fig.4.11 for the nominal case: $Re_L = 3.44x10^6$ (60 m/s), $H/L = 1/2$, and in Fig. 4.12 for different levels of flow confinement.

Figures 4.11b and 4.12b illustrate a series of favorable and adverse pressure gradients along the streamwise direction of the flow. Pressure increases momentarily as flow encounters the retarding force brought on by the curvature of the speed-bump. Continuity prevails as flow accelerates over the ridge of the speed-bump, decreasing the pressure at the surface significantly, before recovering shortly thereafter as the cross-sectional area of the flow

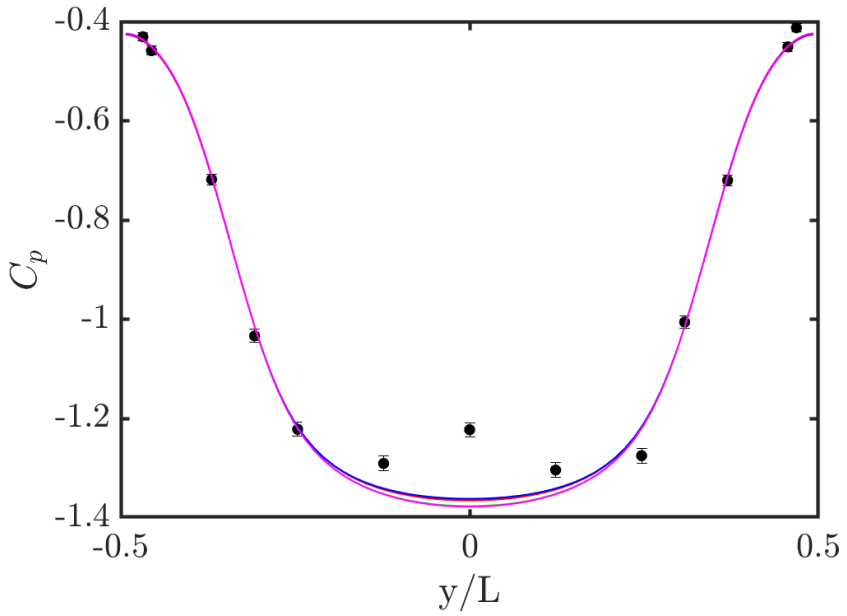

(a)

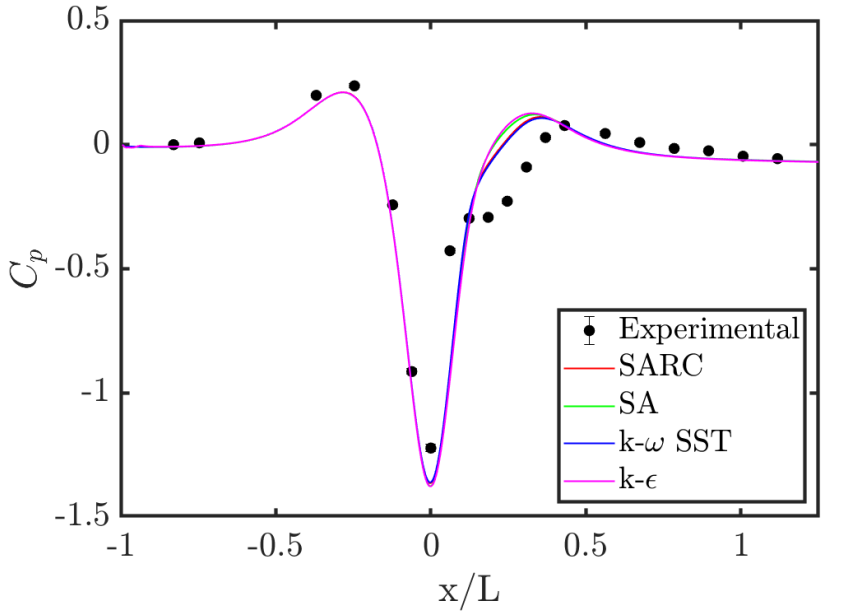

(b)

Figure 4.11: (a) Streamwise centerline and (b) spanwise centerline surface pressure profiles at H/L = 0.5, $Re_L = 3.44x10^6$ (60 m/s), with 3D RANS simulations from Samuell [6].

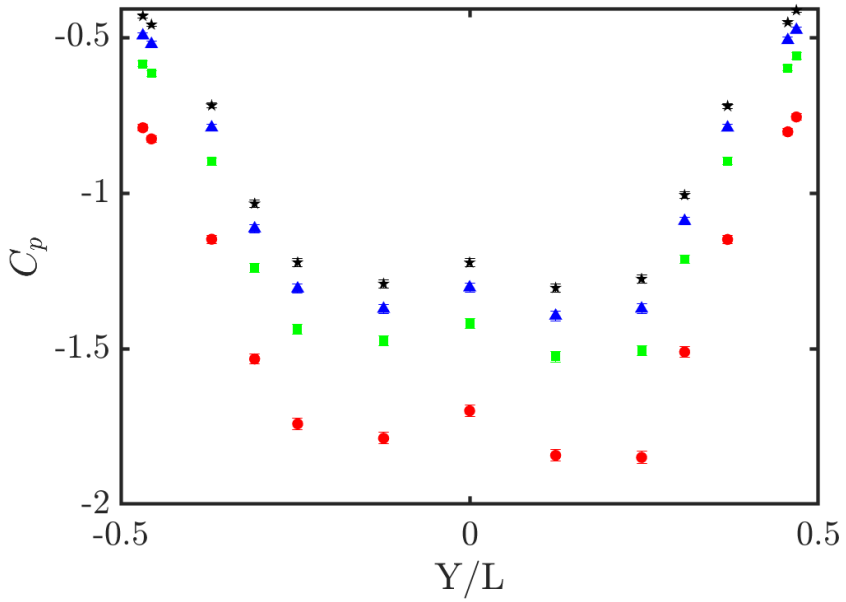

(a)

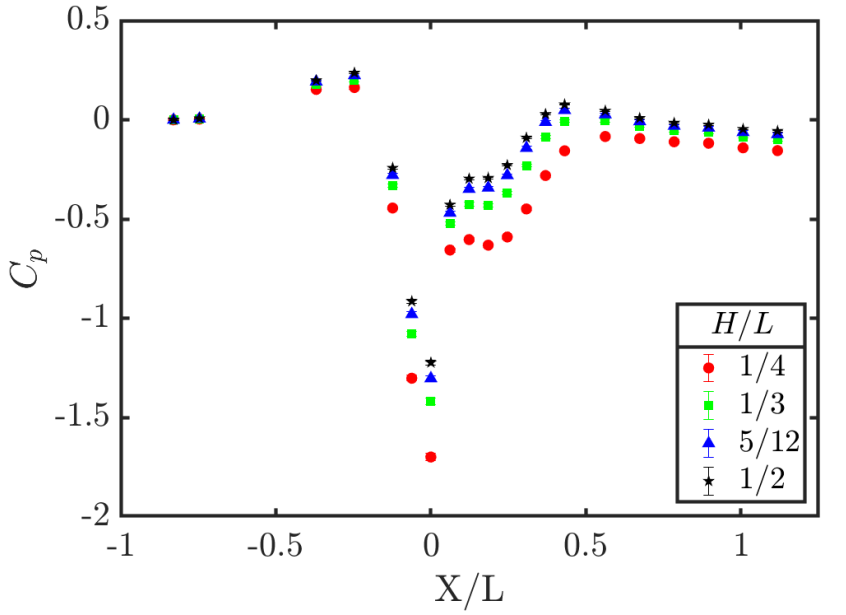

(b)

Figure 4.12: (a) Streamwise centerline and (b) spanwise centerline surface pressure profiles at various levels of flow confinement. $Re_L = 3.44x10^6$ (60 m/s).

channel increases. At the interface of the downstream adverse pressure gradient, the profile departs its symmetric recovery towards a region of lower pressure. While surface pressure is not a conclusive quantity to ascertain flow separation, one can reasonably infer from the surface pressure data that the 'kink' in the spanwise centerline profile is likely due to flow separation. Surface pressure does not recover to the upstream reference pressure downstream of the speed-bump peak due to losses encountered in the separated region.

Samuell [6] studied a comparison of these pressure signals to corresponding 3D RANS simulations. Results from these simulations and the experiment correspond closely along the shoulder of the speed-bump in Fig. 4.11a, but deviate greatly at the streamwise centerline where reduced experimental pressure magnitudes produce a double-peaked profile. Examination of surface pressure along the spanwise centerline in Fig. 4.11b also reveals significant deviation between simulated and experimental trends within the separated region. The experimental features were not captured by any of the tested RANS models in this region. The cause of these discrepancies is not well understood but is thought to be due to a three-dimensional line of separation that is not captured well in simulation (see Section 4.5).

The experimental data revealed a slight spanwise asymmetry, the largest of which was approximately 4%, observed between corresponding coefficients of pressure on either side of the spanwise centerline along the speed-bump ridge near y/L = ± 0.1. The magnitude of asymmetry at this location increased by 2% at the highest confinement, $H/L = 0.25$. Interestingly, the flow was biased towards $y/L > 0$ near the streamwise centerline along the ridge and immediately downstream. For every other location along the speed-bump, including most of the separated region, the flow was biased towards $y/L < 0$. Further testing of the speed-bump in different orientations in the wind tunnel is required to determine if slight asymmetries in the geometry and/or inflow are responsible for the asymmetric pressure trends.

As the amount of flow confinement increased, the unique features of these profiles remained. The only observable effect of increasing confinement was scaling of the profile to higher magnitudes. This data is intended to corroborate corresponding simulations, which

may have difficulty resolving the flow with a more-confined domain. At the time of this writing, these simulations are currently underway and a comparison to these experiments results is forthcoming.

The spanwise centerline pressure profiles show an interesting Reynolds number dependency in both the experiment and simulation as shown in Fig. 4.13a. Simulations in this figure employ the Spalart-Allmaras with Rotational Correction (SARC) model only. Both simulated and experimental data correspond closely outside of the separated region. Interestingly, within the separated region, the simulations had excellent agreement with experimental results at $Re_L = 1.39x10^6$, but the profiles diverge with increasing Reynolds number. Although the trends were in opposite directions, both the experimental and simulation data showed a relative insensitivity to Reynolds number above $2.55x10^6$. The exact cause of the dependency on Reynolds number is not well understood but was initially thought to be due to a dependency upstream (e.g. relaminarization), or a similar dependency on Reynolds number in the line of flow separation. The possibility of upstream relaminzarization is discussed in Section 4.4, and is not thought to occur at the Reynolds numbers tested in this experiment.

Detailed examinations of the entire surface pressure field are presented for nominal conditions in Fig. 4.14. The unsteadiness of the separated region is evident in the visualization of the standard deviation of pressure shown in Fig. 4.14b. Downstream of the speed-bump ridge on either side of the spanwise centerline, where counter-rotating surface vortices were observed in earlier flow visualizations (see Fig. 4.23), surface pressure variation was significantly greater despite the long tubing connecting the taps to the pressure transducer. A comparison of pressure distributions about the mean is shown for the three colored taps in Fig. 4.15. While the pressure distributions are within the uncertainty range of the sensor for taps upstream of separation, those near and in the separated region show significantly higher variability. These results encourage high-frequency direct measurement of surface pressures in the separated region, which may reveal additional information about its structure and dynamics, as a topic of further research.

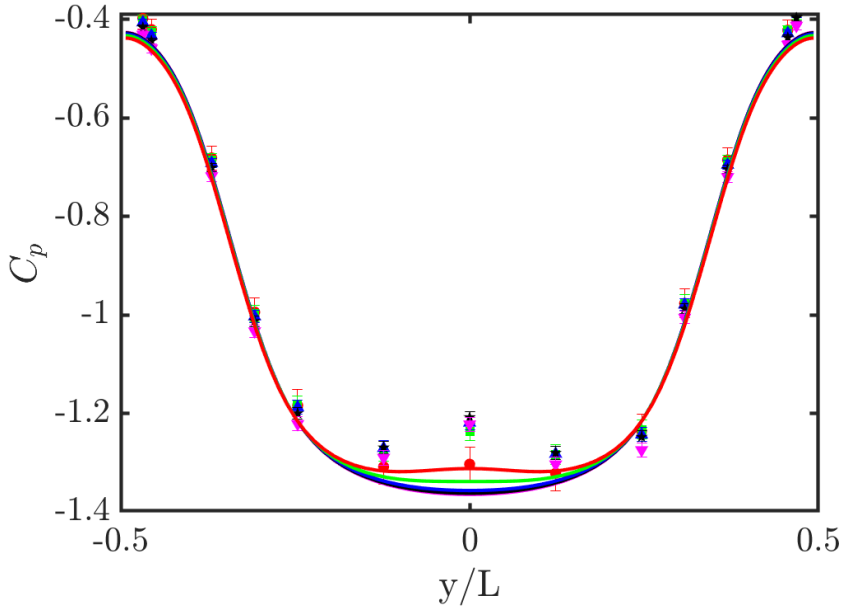

(a)

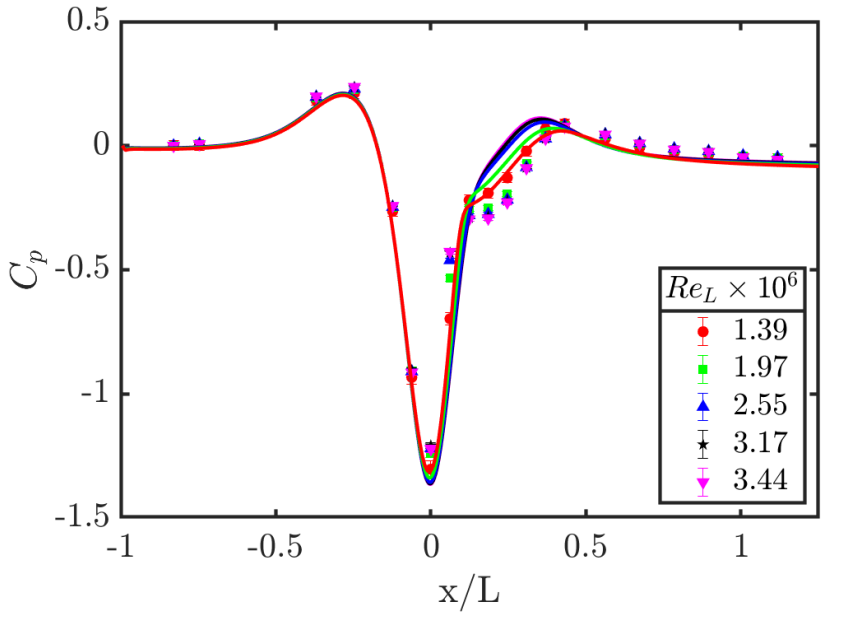

(b)

Figure 4.13: (a) Streamwise centerline and (b) spanwise centerline surface pressure profiles for various Reynolds numbers compared with RANS (SARC) simulations from Samuell [6], H/L = 1/2.

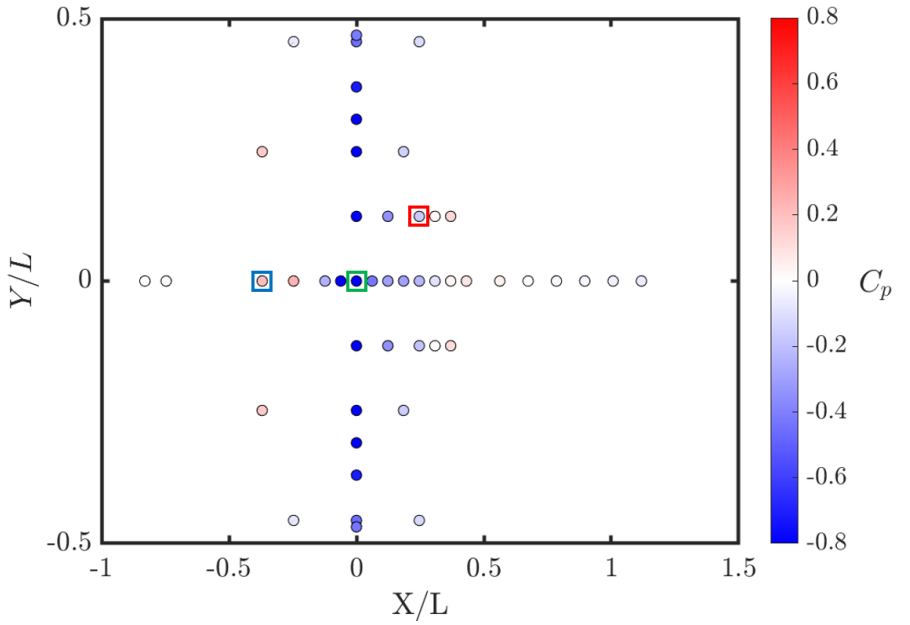

(a)

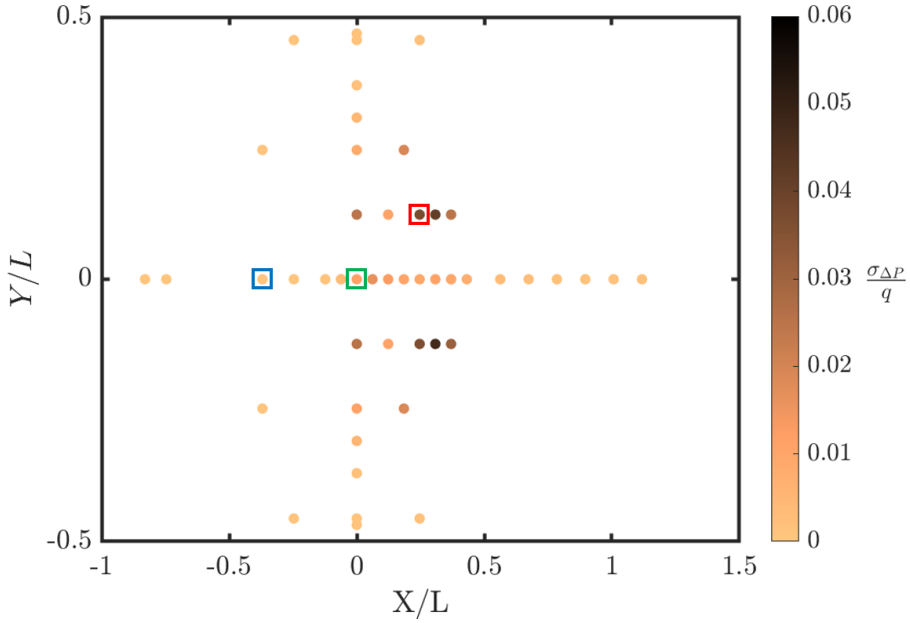

(b)

Figure 4.14: Spatial maps of (a) surface pressure coefficient, and (b) surface pressure standard deviation at $Re_L = 3.44x10^6$, H/L = 1/2. Flow from left to right.

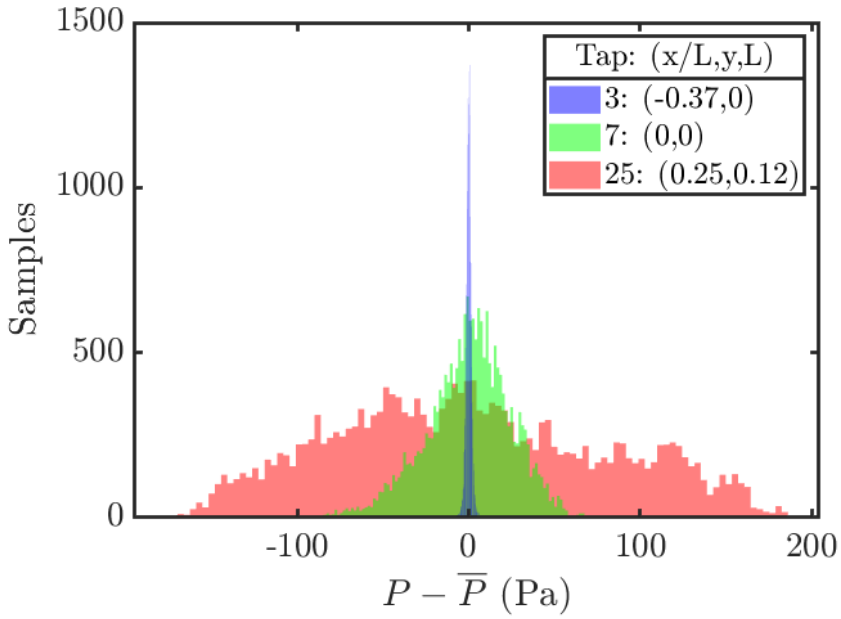

Figure 4.15: Surface pressure distributions about the mean for three pressure taps at $Re_L = 3.44x10^6$, H/L = 1/2.

4.4 Upslope Turbulent Energy

The source of the observed experimental Reynolds number dependence in the surface pressure profiles remains unclear. Given the strong favorable pressure gradient along the upstream slope of the speed-bump, it was hypothesized that the boundary layer either partially or fully relaminarized in this region. Balin et al. [30] and Uzun and Malik [32] observed in DNS ($Re_L = 1.0 \times 10^6$) that a reverse transitional process brought on by the strong favorable pressure gradient substantially weakened the turbulent boundary layer, although whether the flow fully relaminarized is contested.

To determine potential relaminzarization in the experimental flow, and its dependency on Reynolds number, the evolution of turbulent energy was examined upstream of the speed-bump peak along the spanwise centerline for $Re_L = 1.39, 1.97, 3.44 \times 10^6$. Based on PIV data from a series of measurement locations, the in-plane turbulence intensity normalized by the friction velocity is plotted in Fig. 4.16. Small aberrations are present near the apex of the speed-bump due to blockage of the laser by a modular insert on the ceiling of the tunnel.

In-plane turbulence intensity decreased from by 6.26%, 10.26%, and 12.93% between $-0.18 \leq x/L \leq 0.01$ for $Re_L = 1.39, 1.97, 3.44 \times 10^6$ respectively. Since relaminarization is most likely to occur at lower Reynolds numbers, this relationship suggests that the flow did not relaminarize for the Reynolds numbers tested. The difference between the lowest experimental Reynolds number tested ($Re_L = 1.4 \times 10^6$) and that of the DNS ($Re_L = 1.0 \times 10^6$), should be noted in this conclusion. Additional quantities are available in the literature to express the extent of relaminarization, such as the acceleration parameter and relaminarization parameter. Determining these parameters for the experimental flow is a topic of further research.

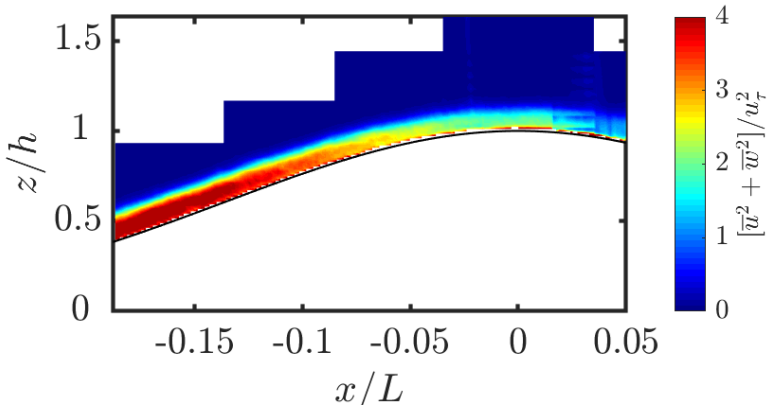

(a) $Re_L = 1.39x10^6$ (20 m/s)

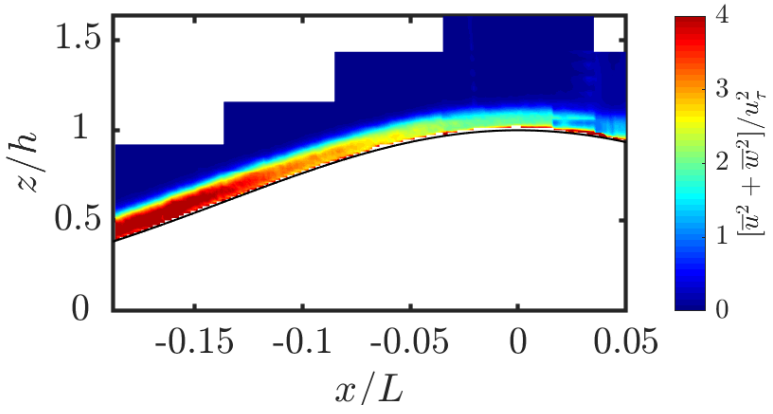

(b) $Re_L = 1.97x10^6$ (30 m/s)

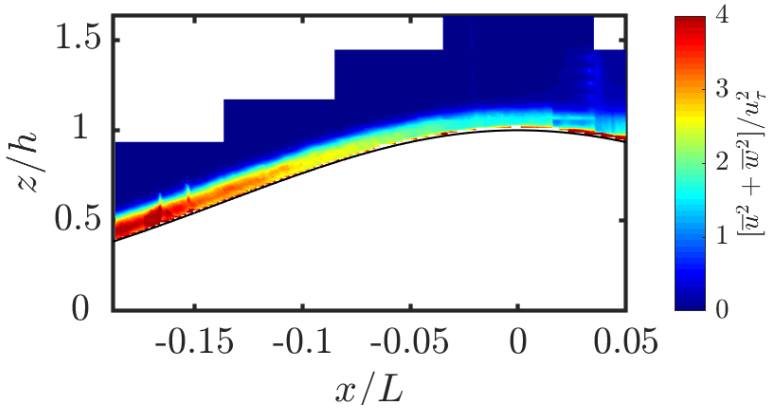

(c) $Re_L = 3.44x10^6$ (60 m/s)

Figure 4.16: Variation in mean in-plane TKE with Reynolds number on upstream slope of the speed-bump.

4.5 Region of Separated Flow

Composite statistical flowfields were obtained via PIV and are illustrated for nominal conditions ($Re_L = 3.44x10^6$, H/L = 1/2) in Fig. 4.17. The aberrations present in these images, particularly near the wall, were due to background noise and laser reflections and are not thought to represent true features of the flow. The mean streamwise velocity field in Fig. 4.17a shows a significant acceleration of the flow to velocities approximately 1 1/2 times freestream near the speed-bump apex. Shortly downstream of the apex, the flow appears to separate off the leeward side of the speed-bump as a strong adverse pressure gradient is encountered. A shear layer developed before reattaching later downstream, possibly forming a thin separation bubble. Mean in-plane turbulent energy, depicted in Fig. 4.17c, was appreciably greater within the separated region, dissipating near reattachment later downstream. The mean vertical component of velocity was positive below the shear layer, near x/L = 0.2, suggesting that the flow was drawn up from the surface and into the separated region near the spanwise centerline.

The uncertainty of the statistical flowfields was formulated on the basis of the standard deviation of a quantity over the series of frames measured in a set (see Appendix C). Thus, uncertainty in all statistical quantities was significantly greater downstream of separation. For mean velocity, uncertainties on the order of 1% of freestream were common in the separated region and were an order of magnitude less elsewhere.

The shape of this region, specifically the separation and reattachment locations, the vertical extent of separation, and its dependency on position and/or Reynolds number, were important to characterize for contextualization of the previously obtained surface pressure measurements. The separated region was found to be highly dependent on spanwise location due, primarily, to the three-dimensionality introduced by the taper of the model geometry towards the side-walls.

Mean streamwise velocity, vertical velocity, and in-plane turbulent kinetic energy fields at $Re_L = 3.44x10^6$ are illustrated at various spanwise locations in Figs. 4.18, 4.19, and 4.20

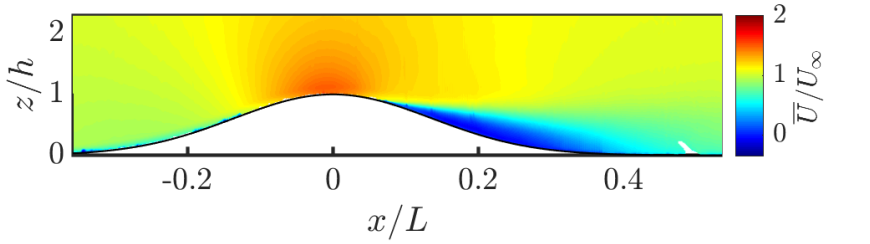

(a)

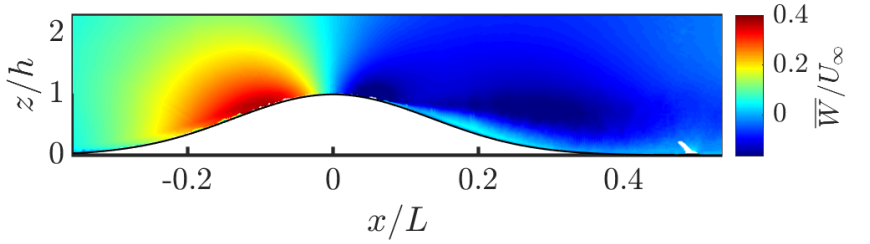

(b)

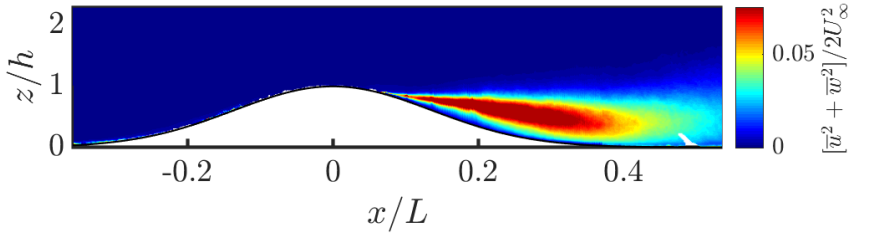

(c)

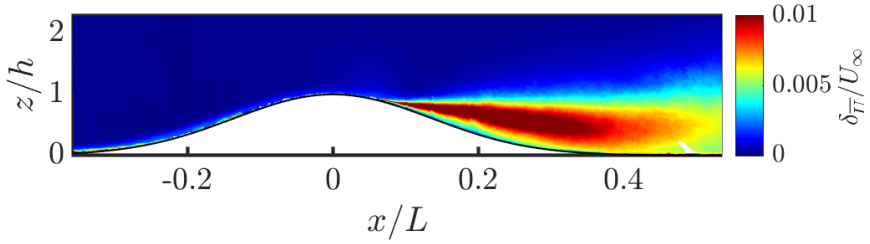

(d)

Figure 4.17: Mean (a) streamwise velocity, (b) vertical velocity, (c) in-plane TKE, and (d) velocity uncertainty flowfields over speed-bump at y/L = 0.083, $Re_L = 3.44x10^6$, H/L = 1/2.

respectively, with spanwise centerline cases depicted in Figs. 4.18a, 4.19a, and 4.20a. The angle of the shear layer from the surface of the speed-bump was greatest at the spanwise centerline and decreased as the spanwise distance from the centerline increased. While it is not possible to directly measure the location of separation with these measurements, the farthest-upstream evidence of the shear layer suggests that separation occurred near x/L = 0.075 at the spanwise centerline for $Re_L = 3.44x10^6$. Farther away from the centerline, the initiation of the shear layer appears to move downstream to x/L $\approx$ 0.1 at y/L = $\pm$ 0.235 and is closer to the surface. The decreasing angle of the shear layer and diminishing region of turbulent energy farther from the centerline implies that the flow experienced, at best, weak or incipient separation past y/L = $\pm$ 0.1. At y/L $\approx$ 0.23, the turbulent energy downstream was highly diminished, suggesting the flow likely remained attached at and beyond this spanwise distance. This three-dimensional line of separation may explain the dual-peaked surface pressure profiles along the ridge of the speed-bump (Figs. 4.11a, 4.12a and 4.13a). However, additional measurements will need to be collected using a specialized method, such as oil-film interferometry, to accurately assess the points of separation and reattachment.

The vertical component of velocity, depicted in Fig. 4.19, was appreciably greater below the shear layer at the centerline than at any other spanwise position. Since vertical flow predominated at the centerline, it is likely that flow was drawn from the shoulders of the speed-bump and across the leeward face (into or out of the plane of the figures) to a saddle point at the centerline, where it rolled up into the separated region. The streamlines of a previously conducted surface flow visualization, shown in Fig. 4.23, corroborate this hypothesis. Out-of-plane velocity measurements using stereo-PIV are required for further confirmation.

Data were also collected at corresponding planes on the other side of the spanwise centerline, allowing for the assessment of flow symmetry. With no discernible biases observed in the as-built speed-bump geometry and only a slight bias observed in the inflow, the mean separated region was expected to remain symmetric. Figure 4.21 plots the vertical extent of the shear layer, denoted as δ and defined as the wall-normal distance where the mean

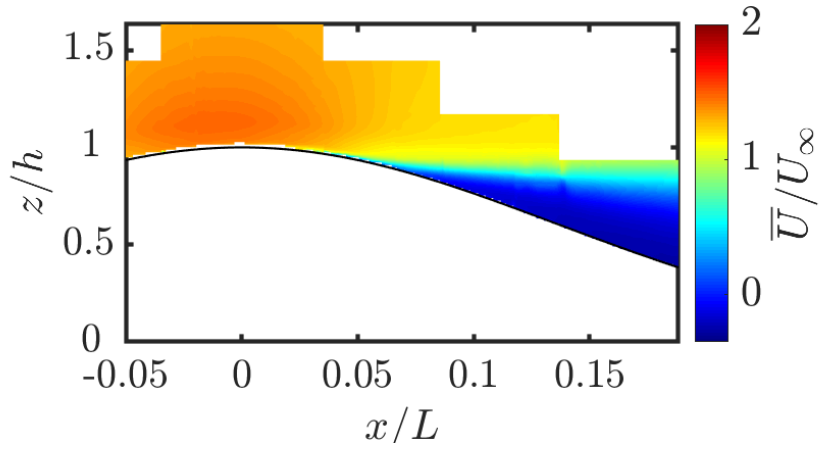

(a) y/L = 0

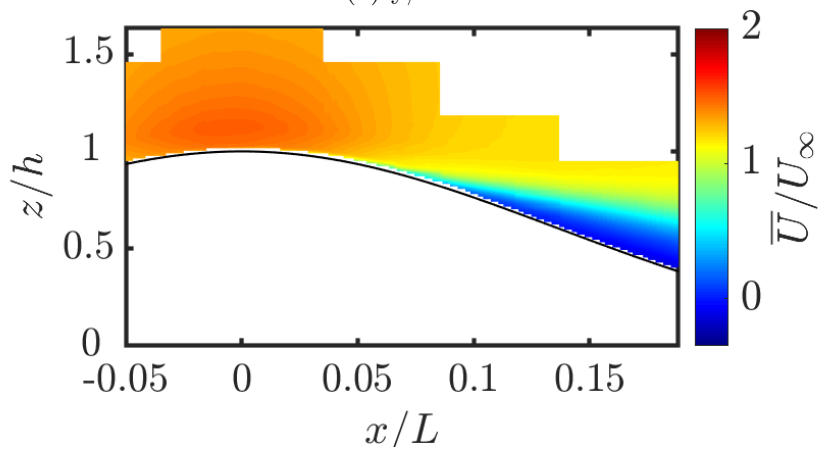

(b) y/L = 0.11

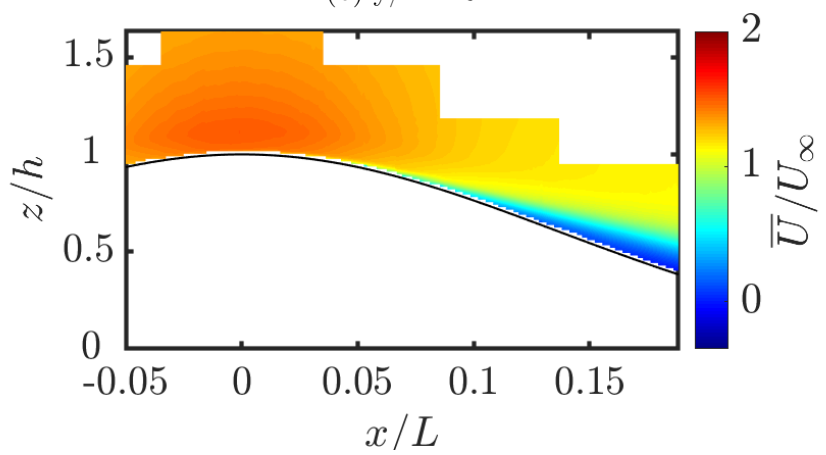

(c) y/L = 0.19

Figure 4.18: Mean streamwise component of velocity over the speed-bump near the separation point at $Re_L = 3.44x10^6$, H/L = 1/2.

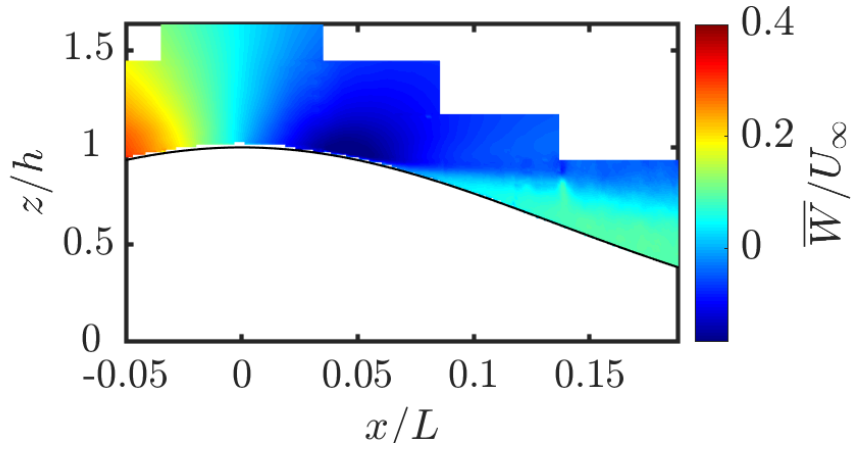

(a) y/L = 0

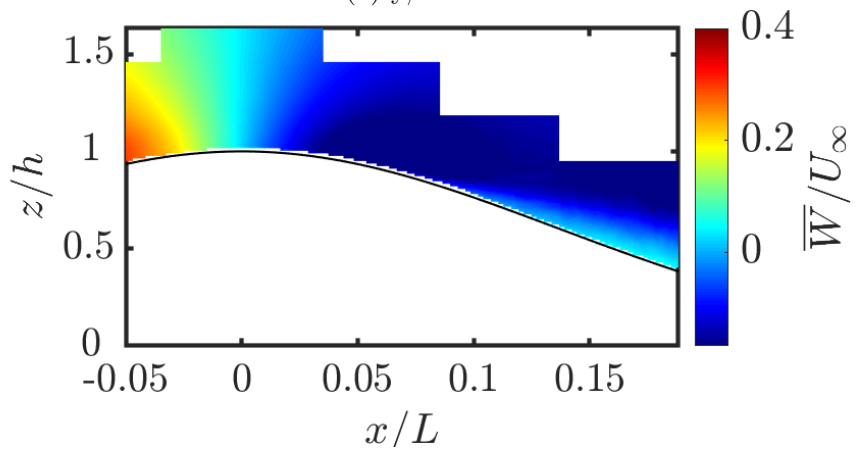

(b) y/L = 0.11

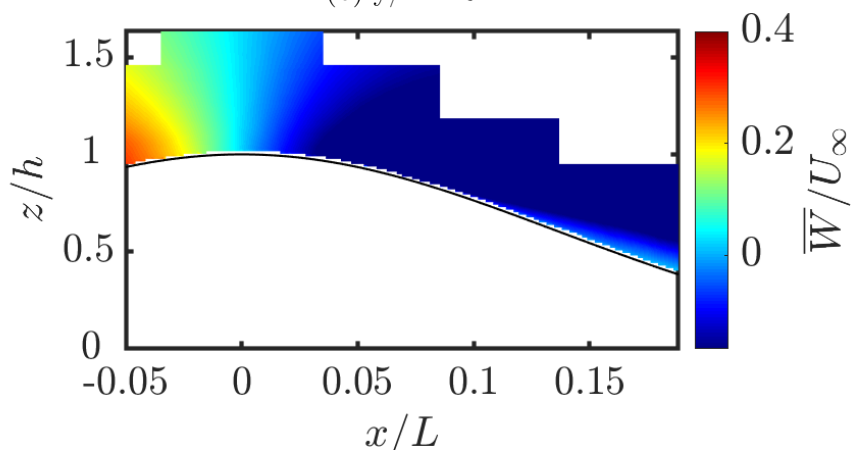

(c) y/L = 0.19

Figure 4.19: Mean normal component of velocity over the speed-bump near the separation point at $Re_L = 3.44x10^6$, H/L = 1/2.

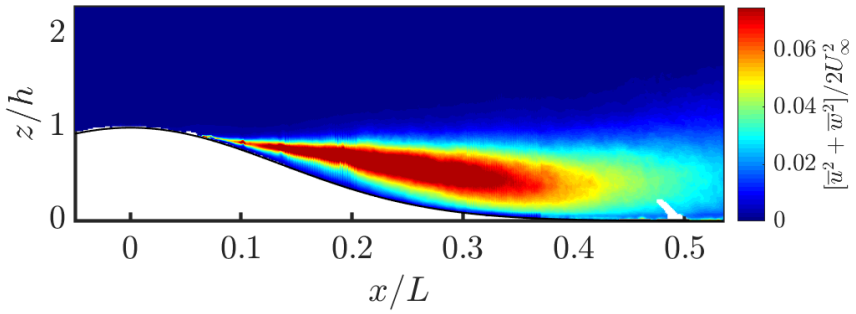

(a) y/L = 0.083

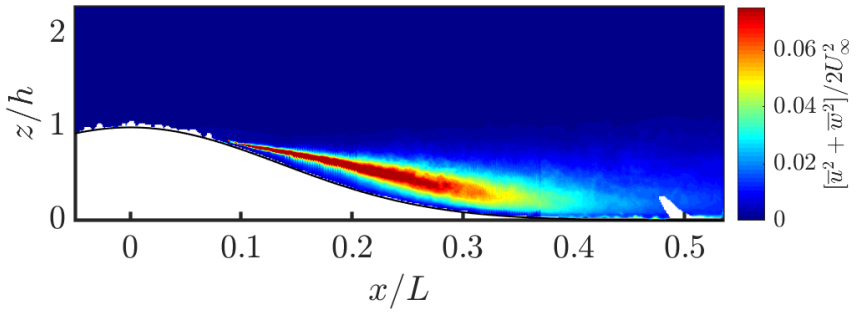

(b) y/L = 0.119

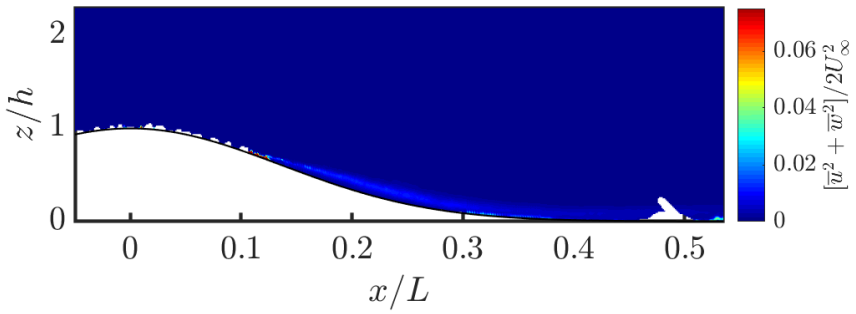

(c) y/L = 0.233

Figure 4.20: Mean in-plane turbulent kinetic energy in the separated region of the speed-bump at $Re_L = 3.44x10^6$, H/L = 1/2.

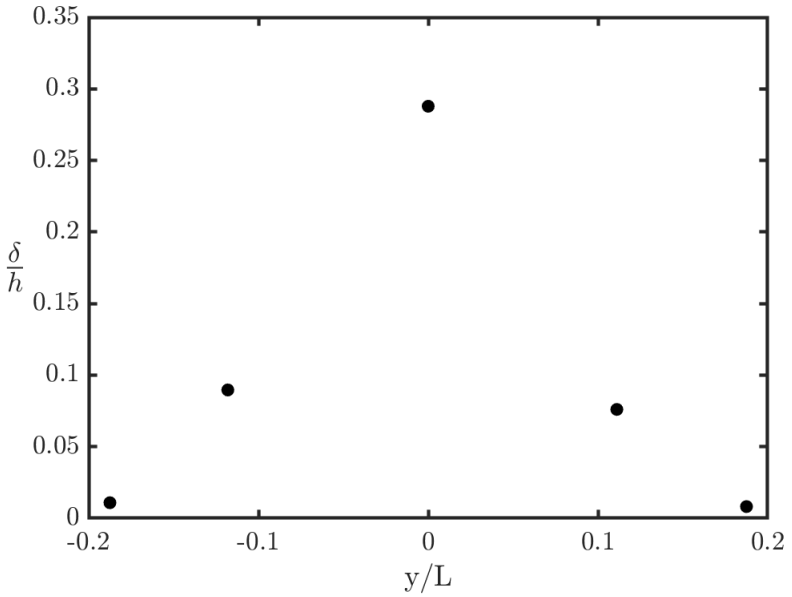

Figure 4.21: Symmetry of vertical extent of shear layer at x/L = 0.18, $Re_L = 3.44x10^6$, H/L = 1/2.

streamwise velocity was 99% of freestream, versus the spanwise locations depicted in Fig. 4.20 and their symmetric counterparts at x/L = 0.18. The height of the separated region was found to be symmetric on either side of the spanwise centerline, within 1.4% of the speed-bump height, corroborating the inflow and geometric measurement results.

Increasing Reynolds number promoted stronger and earlier separation at the centerline, as illustrated in Fig. 4.22. The angle of the shear layer with the surface increased with Reynolds number but was similar for $Re_L \geq 2.55 \times 10^6$ (40 m/s). Similar trends were observed with the intensity of turbulent energy in the separated region and amount of vertical flow observed at the centerline (see Figs. E.7 and E.8 in Appendix E). The estimated separation point migrated upstream from x/L $\approx$ 0.1 at $Re_L = 1.39x10^6$ to x/L $\approx$ 0.075 at $Re_L \geq 2.55 \times 10^6$. These trends highlight a strong correlation between the observed Reynolds number dependency of the surface pressure profiles and the extent of flow separation.

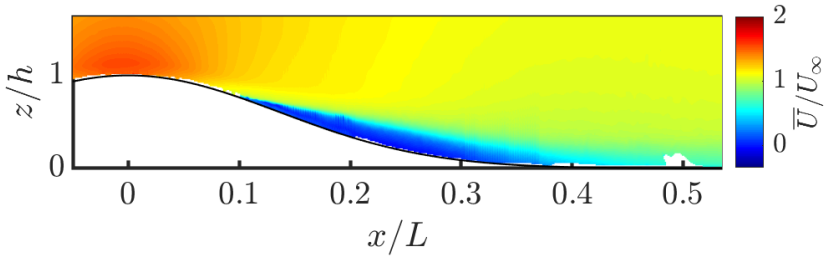

(a) $Re_{L} = 1.39x10^6$

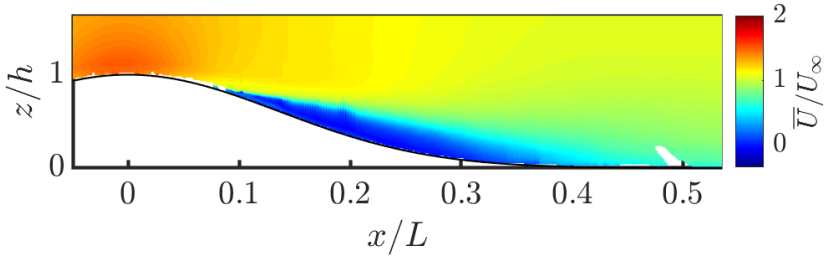

(b) $Re_{L} = 1.97x10^6$

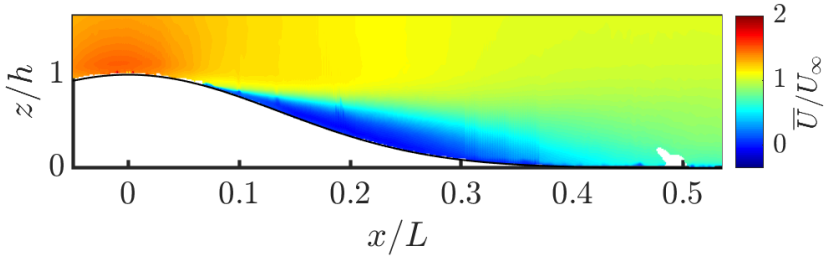

(c) $Re_{L} = 2.55x10^6$

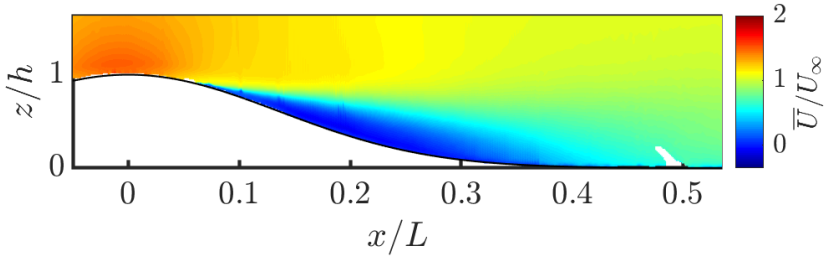

(d) $Re_{L} = 3.44x10^6$

Figure 4.22: Mean streamwise component of velocity near the separated region at various Reynolds numbers at y/L = 0.083, H/L = 1/2.

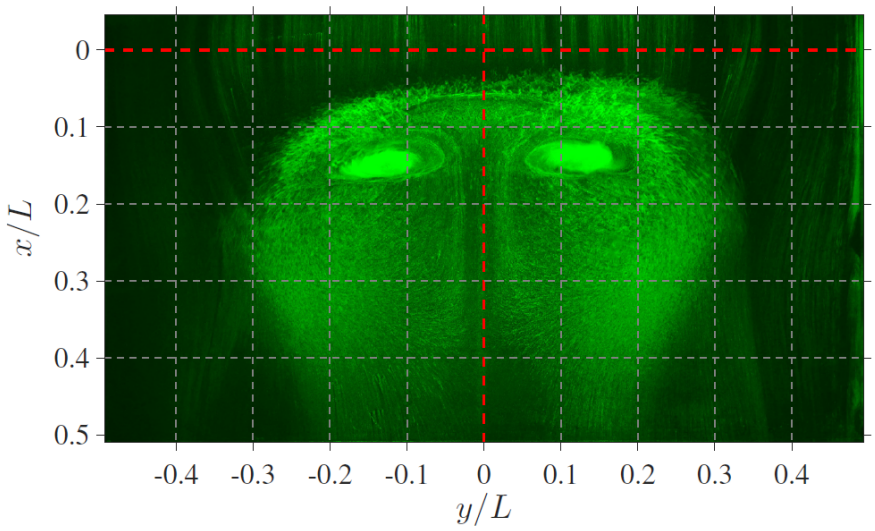

Figure 4.23: China clay flow visualization of flow conducted by Sarwas [5] at $Re_L = 3.44x10^6$, H/L = 1/2. Red lines signify streamwise and spanwise centerlines. Flow from top to bottom.

These flowfields provide a compelling, but not exhaustive, argument for the observed surface pressure trends. Further research must be conducted to understand the interaction of the separated flowfield with the surface, particularly in light of the counter-rotating vortices observed in the separated region from the surface flow visualization illustrated in Fig. 4.23. Additionally, the increased variance observed in surface pressure measurements away from the spanwise centerline and near the counter-rotating vortices should be considered, along with the presence of vertical flow near the spanwise centerline. Out-of-plane velocity measurements and definitive locations of the separation and reattachment are details needed to fully characterize the geometry of the separated region.

Chapter 5

CONCLUSION

Our ability to predict the dynamics of a fluid is limited by computational resources and time. The chaotic nature of high Reynolds number flows requires simplifications, or modeling of turbulence, in some or all regions of a computational simulation in order to produce results at a reasonable expense. In developing numerical turbulence models, some mechanism must be available to validate their efficacy. Comparison to experimental data collected specifically for this purpose is the most practical means to this end.

Experimental validation studies have an additional burden of providing information that not only explores the relevant flow physics of the problem but also characterizes the experiment to the greatest extent possible. This information is important to ensure that the most faithful representation of the experiment is achieved in simulation in order to truly investigate the performance of the numerical model. The level of detail and documentation required of benchmark-quality validation datasets is unprecedented and far exceeds what is typical in traditional experiments.

In collaboration with Boeing, this study attempted to provide benchmark-quality validation data for incompressible flow over a novel speed-bump geometry. The speed-bump deliberately promoted a number of unique flow features that challenge the current capability of turbulence modeling including, most notably, a quasi-two-dimensional region of turbulent separated flow that was affected by a number of control parameters beyond the geometry (e.g. inflow Reynolds number and flow confinement). Other notable features of this geometry that made it unique were amenability to corresponding simulations, taper to avoid interactions with the side-walls and relevance to wing-like shapes.

A number of methods were employed to characterize the experiment. The speed-bump

was three-dimensionally scanned, providing its actual measurement within 1/2 mm for use in simulation, demonstrating compliance with its prescribed definition within 0.057 inches, and showing no geometric biases. The inflow plane of the empty test section was surveyed using a pitot rake, which showed a slight bias towards the port side of the tunnel, and a maximum deviation of 0.2% of the freestream. The median side-wall boundary layers showed good agreement for all tunnel velocities, although some locations on the walls had abnormally thick and highly variable velocity profiles. The side-wall boundary layers were consistent above $Re_L = 2.55 \times 10^6$, but the median profile at $Re_L = 1.39 \times 10^6$ indicated that the side-wall boundary layers were perhaps not fully tripped at this velocity.

With the speed-bump and splitter plate installed, PIV measured fully turbulent boundary layers that were consistent across the span of the splitter plate at all velocities tested. A slight inflow bias towards the port-side of the tunnel was observed over the splitter plate, however this bias was on the order of 0.005% of the freestream velocity and was well within the expected uncertainty of PIV, suggesting that it may have been the result of minor image perspective errors. The turbulent energy on the upstream slope of the speed-bump was also investigated using PIV to determine if relaminarization occurred as a result of the strong favorable pressure gradient. While the turbulent energy of the boundary layer decreased in this region, the relative amount of energy that decreased along the upstream slope of the bump increased with Reynolds number, suggesting that relaminarization did not occur for the range of Reynolds numbers tested in this experiment.

Additional effort was made to define the system responses of the flow, particularly the large-scale features of separation. The surface pressure of the speed-bump was measured at various Reynolds numbers and flow confinements using 48 pressure taps. The streamwise and spanwise centerline pressure profiles revealed a series of streamwise pressure gradients and had unique trends thought to be attributed to separation. These trends were found to be dependent on Reynolds number below $Re_L = 2.55 \times 10^6$, generally increased with flow confinement, and were not well captured by a corresponding 3D RANS simulation. Furthermore, surface pressure was found to be highly variable in the separated region off of

the spanwise centerline, which corresponded to the location of two counter-rotating vortices that were observed in a previously conducted surface flow visualization.

A slight asymmetry was observed in the surface pressure data, the cause of which remains inconclusive as no significant biases were observed in either the as-built test article or in the inflow velocity profile. Rotating the model 180 degrees and retesting in this orientation will ascertain the contribution of any defects in the as-built geometry to the observed pressure asymmetry. Similarly, testing the model in a different orientation in the tunnel, such as on a side-wall, would measure any effects caused by inflow non-uniformity. Simply repeating the test procedure as previously conducted in this study will help determine any random and/or measurement uncertainties that may affect the extent of this asymmetry. Determining a 'total' component of uncertainty from the contributions of the geometry, inflow, and random uncertainty is discussed further in Rhode and Oberkampf [50]. These tasks were not accomplished in this study due to the considerable amount of time and effort required to modify the testing apparatus. If possible, these sensitivities should be examined to investigate the cause.

Finally, the size and shape of the separated region were investigated through spatial mean flowfields measured using PIV. The separated region and line of separation were found to be three-dimensional, with separation occurring farther upstream at the spanwise centerline and with attached flow likely beyond y/L = $\pm$ 0.25. The size of the separated region decreased as the distance away from the spanwise centerline increased. The vertical component of velocity was greatest at the spanwise centerline, corresponding to the location of a saddle point on the surface, meaning that flow was likely drawn in from the shoulders of the speed-bump. Both the shape of the separated region and the separation point were shown to be dependent on Reynolds number, especially below $Re_L = 2.55 \times 10^6$, corresponding to a similar trend observed in the surface pressures. While further research needs to be conducted to fully define the size and shape of the separated region, it is clear from these investigations that the dynamics of the separated region would be challenging to accurately represent with corresponding two-dimensional simulations.

In all of these experiments, a rigorous treatment of uncertainty was applied to both measured and derived quantities when possible. Additionally, these results are accompanied by an extensive amount of documentation of the experimental facility, measurement equipment, reduction methods, and other relevant data located in the appendix of this manuscript.

The work performed towards this validation campaign is far from complete. In an effort to provide benchmark-quality validation data, a greater understanding of the system response quantities is necessary along with further characterization of the experiment, such that a corresponding direct numerical simulation of the experiment could be conducted and used for comparison. This manuscript will conclude with an appraisal of the current model validation experiment completeness levels of this study in accordance with the attributes of a commonly accepted framework provided by Oberkampf and Smith [1], with recommendations for further work.

Experimental facility

The documentation of the experimental facility that is provided in this report includes detailed schematics of the Aeronautics Laboratory from its original construction, dimensions of the wind tunnel (including the coordinates of the contraction section), basic specifications of the wind tunnel materials, the locations of probes and taps, a description of the inflow conditioning system, a description of the tunnel velocity calibration procedure, information pertaining to particle seeding for PIV, and a statement of flow velocity and temperature variability over the duration of a test. Flow uniformity and side-wall boundary layer measurements were obtained at the inflow plane of an empty test section, with the exception of the corners. Additionally, an analysis of the freestream turbulence spectrum at the inflow was conducted and detailed in Sarwas [5].

For higher completeness, the streamwise variability of uniformity and side-wall boundary layers across the test section should be assessed using pitot rake measurements at the outflow plane. Additionally, an exact definition of the wind tunnel's geometry, particularly in the contraction and test section, could be obtained via a three-dimensional scan of the wind

tunnel. A particularly detailed scan of a small section of the interior of the tunnel could classify the surface roughness of the tunnel walls. A more challenging endeavor for higher completeness would involve modifying the wind tunnel to place temperature and pressure sensors upstream of the test section for measurements over the duration of a run.

The information in-hand regarding the experimental facility is extensive, but falls just short of level two completeness, particularly since the outflow is yet not characterized. Therefore, the current completeness level of the experimental facility attribute is **1.75**.

Analog instrumentation and signal processing

A set of manufacturer specifications is provided for the pressure and temperature sensors and data acquisition platforms used in this experiment. Additional information is also provided on the calibration of the pressure sensors. A detailed description of the equipment used in PIV is outlined in this manuscript, along with acquisition parameters and reduction procedures. Over 15 TB of raw images collected with PIV are stored and available at request. Following the specific examples of information required for each level of this attribute, listed in Oberkampf and Smith [1], the documentation in-hand for this attribute meets a high level of completeness.

For a higher level of completeness, planar-PIV results should be corroborated using stereo-PIV, and the testing procedure should be modified to incorporate a zero-pressure tare subtraction for the pressure sensors during each test.

The current completeness level of the analog instrumentation and signal processing attribute in this experiment is **2.5**.

Boundary and initial conditions

For flow with the splitter plate and speed-bump installed, the streamwise and vertical components of velocity are available at five streamwise planes ahead of the bump. Since the flow is subsonic with a moderate amount of tunnel blockage, the empty-tunnel inflow definition obtained with the pitot rake is not a sufficient boundary condition. Therefore, only the

PIV inflow measurements are valid for this purpose. Additional data in-hand includes the as-manufactured geometry of the speed-bump measured from a three-dimensional scan.

A considerable amount of effort should be undertaken towards this attribute in further research. Future data products that would be useful are spanwise components of velocity at the inflow plane of the test section, all three velocity components at the outflow, and static and total temperature in both locations. The surface roughness of the speed-bump's painted surfaces and the plexiglass side-walls should also be characterized. Imperfections in the walls (e.g. the juncture of the splitter plate and the speed-bump), the region between the plate and the side-walls, and the seals of the test section door should all be measured for high completeness. Additionally, for high completeness, any elastic deformations or vibrations in the model geometry over the course of a run should be measured, although the design of the mounting plate suggests that the geometry remains stiff.

The current completeness level of the boundary and initial conditions attribute in this experiment is **1**.

Fluid and material properties

Relative humidity, atmospheric pressure, and ambient temperature were recorded prior to every run. Density and viscosity were calculated by the Ideal Gas Law and Sutherland's Law respectively, assuming accepted constants for dry air. Since this experiment did not consider coupled heat transfer, a flexible test article, or fluid-structure interactions, the material properties of the speed-bump were not relevant for characterization.

It is thought that all relevant elements of this attribute are sufficiently characterized in this experiment. However, the instrument measuring the atmospheric conditions has relatively low accuracy compared to alternative products that could be incorporated in this experiment. Similarly, the instrumentation measuring the tunnel temperature could be improved by integrating a thermistor (see Appendix B. With this in mind, the completeness level of the fluid and material properties attribute is **2.75**.

Test conditions

A log of room temperature, static pressure, and relative humidity at the start of each run was kept. Additionally, a description of the temperature control of the room was provided. Appreciable changes to the relative humidity in the room were observed over the course of longer runs, but not recorded. New instrumentation should be implemented in order to capture the temporal evolution of all atmospheric conditions during runs. The corresponding completeness level of the test conditions attribute is **1.5**.

System response quantities

The surface pressure on the speed-bump and spatial flowfields measured using PIV were two system response quantities studied extensively in this experiment. Both techniques provided an independent assessment of the streamwise pressure gradient of the flow, along with an estimation of the separation location. The surface pressure measurements were compared to a corresponding RANS simulation, exposing the inability of RANS to predict some features of separation. Measurements were collected in a time series, allowing for statistical parameters to accompany the mean results. Additionally, great effort was taken to estimate the dependencies of these quantities on Reynolds number (and flow confinement for surface pressures), along with an estimation of their uncertainty. In conjunction with the signal processing attribute, the scripts used to reduce the system response quantities are also documented.

Conveniently, any further research to gain a greater understanding of the complex flow physics at work in this experiment will provide an additional means of comparison for corresponding simulations. Furthermore, testing with more-specialized techniques may corroborate previously obtained measurements (e.g. stereo-PIV, laser-Doppler velocimetry, hot wire anemometry). In addition to measuring a greater number of system responses, previous measurements should be repeated using the same technique in an effort to quantify the random component of uncertainty for that quantity. Anomalous trends, such as the thick

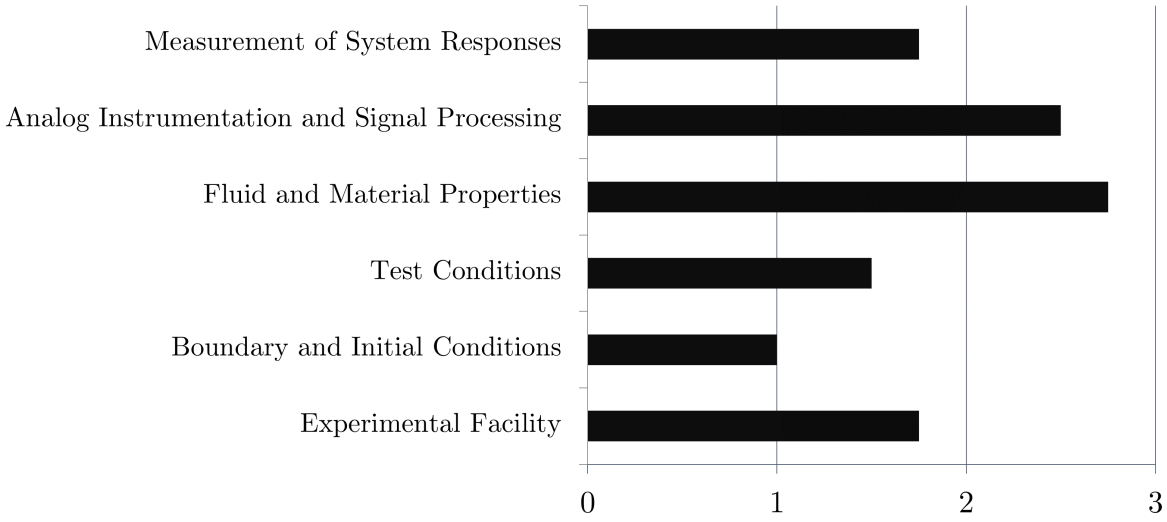

Figure 5.1: Summary of the model validation experiment completeness levels for the speed-bump turbulent separated flow validation experiment at the time of this writing.

boundary layer profiles observed at certain stations at the inflow plane, require the most attention in this regard. These quantities should be measured using a different orientation of the speed-bump in order to quantify uncertainty due to the geometry and instrumentation.

While this experiment gathered data over a wide spatial and temporal range for surface pressures and spatial flowfields, repeated measurements of these quantities using both the previously employed methods and other techniques should be obtained. Thus, the completeness level for the system response quantities attribute in this experiment is **1.75**.

A summary of the completeness level for each attribute in the experiment is given in Fig. 5.1. The greatest deficiency was observed in the boundary and initial conditions attribute, while the fluid and material properties attribute was characterized to nearly the maximum extent. Following this appraisal, it is reasonable to conclude that the efforts conducted thus far towards this project substantially advanced its goal of becoming a strong-sense benchmark for validation.

BIBLIOGRAPHY

[1] William L Oberkampf and Barton L Smith. "Assessment Criteria for Computational Fluid Dynamics Model Validation Experiments". eng. In: *Journal of verification, validation, and uncertainty quantification* 2.3 (2017). ISSN: 2377-2158.

[2] William K George. "Lectures in Turbulence for the 21st Century". In: (2013).

[3] Clay Math Institute. *Navier–Stokes Equation*. https://www.claymath.org/millennium-problems/navier%E2%80%93stokes-equation. Online; accessed 15-Jan-2021. Dec. 2020.

[4] J. Slotnick et al. *Vision 2030 CFD study: A path to revolutionary computational aerosciences*. Tech. rep. NASA/CR-2014-218178, 2014.

[5] E. Sage Sarwas. "Experimental Examination of New Separated Turbulent Flow Validation Test Geometry". MA thesis. University of Washington, Jan. 2019.

[6] Madeline C. Samuell. "Development of a Turbulent Separated Flow Validation Test Case: Experimental and Computational (RANS) Studies". English. PhD thesis. 2020, p. 106. ISBN: 9798684669910. URL: https://search.proquest.com/dissertations-theses/development-turbulent-separated-flow-validation/docview/2456864105/se-2?accountid=14784.

[7] Owen Williams et al. "Experimental Study of a CFD Validation Test Case for Turbulent Separated Flows". In: *AIAA Scitech 2020 Forum*. 2020. DOI: 10.2514/6.2020-0092. eprint: https://arc.aiaa.org/doi/pdf/10.2514/6.2020-0092. URL: https://arc.aiaa.org/doi/abs/10.2514/6.2020-0092.

[8] William L Oberkampf and Timothy G Trucano. "Verification and validation in computational fluid dynamics". eng. In: *Progress in aerospace sciences* 38.3 (2002), pp. 209–272. ISSN: 0376-0421.

[9] Daniel P Aeschliman and William L Oberkampf. "Experimental Methodology for Computational Fluid Dynamics Code Validation". eng. In: *AIAA journal* 36.5 (1998), pp. 733–741. ISSN: 0001-1452.

[10] Gwibo Byun and Roger L. Simpson. "Structure of three-dimensional separated flow on an axisymmetric bump". In: *AIAA Journal* 44.5 (2006).

[11] Gwibo Byun, Roger L. Simpson, and C. H. Long. "Study of Vortical Separation from Three-Dimensional Symmetric Bumps". In: *AIAA Journal* 42.4 (2004), pp. 754–765. DOI: 10.2514/1.1829. eprint: https://doi.org/10.2514/1.1829. URL: https://doi.org/10.2514/1.1829.

[12] Gwibo Byun and Roger L. Simpson. "Surface-Pressure Fluctuations from Separated Flow over an Axisymmetric Bump". In: *AIAA Journal* 48.10 (2010), pp. 2397–2405. DOI: 10.2514/1.J050429. eprint: https://doi.org/10.2514/1.J050429. URL: https://doi.org/10.2514/1.J050429.

[13] Nayan Patel, Christopher Stone, and Suresh Menon. "Large-Eddy Simulation of Turbulent Flow over an Axisymmetric Hill". In: *41st Aerospace Sciences Meeting and Exhibit*. DOI: 10.2514/6.2003-967. eprint: https://arc.aiaa.org/doi/pdf/10.2514/6.2003-967. URL: https://arc.aiaa.org/doi/abs/10.2514/6.2003-967.

[14] Jony Castagna, Yufeng Yao, and Jun Yao. "Numerical Simulation of a Turbulent Flow over an Axisymmetric Hill". In: *50th AIAA Aerospace Sciences Meeting including the New Horizons Forum and Aerospace Exposition*. DOI: 10.2514/6.2012-98. eprint: https://arc.aiaa.org/doi/pdf/10.2514/6.2012-98. URL: https://arc.aiaa.org/doi/abs/10.2514/6.2012-98.

[15] J.H. Bell et al. "Surface and flow field measurements on the FAITH Hill Model". In: *AIAA-2012-0704* (2012).

[16] Nicholas M. Husen, Tianshu Liu, and John P. Sullivan. "Luminescent Oil Film Flow Tagging Skin Friction Meter Applied to FAITH Hill". In: *AIAA Journal* 56.10 (2018),

pp. 3875–3886. DOI: 10.2514/1.J057114. eprint: https://doi.org/10.2514/1.J057114. URL: https://doi.org/10.2514/1.J057114.

[17] William L. Oberkampf and Barton Smith. "Assessment Criteria for Computational Fluid Dynamics Validation Benchmark Experiments". In: *52nd Aerospace Sciences Meeting* (Oct. 2014). DOI: 10.2514/6.2014-0205.

[18] Kyle P. Lynch et al. "Revisiting Bachalo-Johnson: The Sandia Axisymmetric Transonic Hump and CFD Challenge". In: *AIAA Aviation 2019 Forum*. DOI: 10.2514/6.2019-2848. eprint: https://arc.aiaa.org/doi/pdf/10.2514/6.2019-2848. URL: https://arc.aiaa.org/doi/abs/10.2514/6.2019-2848.

[19] Kyle P. Lynch et al. "A CFD Validation Challenge for Transonic, Shock-Induced Separated Flow: Experimental Characterization". In: *AIAA Scitech 2020 Forum*. DOI: 10.2514/6.2020-1309. eprint: https://arc.aiaa.org/doi/pdf/10.2514/6.2020-1309. URL: https://arc.aiaa.org/doi/abs/10.2514/6.2020-1309.

[20] Steven J. Beresh et al. "A CFD Validation Challenge for Transonic, Shock-Induced Separated Flow: Approach and Metrics". In: *AIAA Scitech 2020 Forum*. DOI: 10.2514/6.2020-1308. eprint: https://arc.aiaa.org/doi/pdf/10.2514/6.2020-1308. URL: https://arc.aiaa.org/doi/abs/10.2514/6.2020-1308.

[21] Julie E. Duetsch-Patel et al. "Aerodynamic Design and Assessment of Modular Test Section Walls for CFD Validation in Hybrid Anechoic Wind Tunnels". In: *AIAA Scitech 2020 Forum*. 2020. DOI: 10.2514/6.2020-2214. eprint: https://arc.aiaa.org/doi/pdf/10.2514/6.2020-2214. URL: https://arc.aiaa.org/doi/abs/10.2514/6.2020-2214.

[22] Aldo Gargiulo et al. "Examination of Flow Sensitivities in Turbulence Model Validation Experiments". In: *AIAA Scitech 2020 Forum*. 2020. DOI: 10.2514/6.2020-1583. eprint: https://arc.aiaa.org/doi/pdf/10.2514/6.2020-1583. URL: https://arc.aiaa.org/doi/abs/10.2514/6.2020-1583.

[23] Todd Lowe et al. "Status of the NASA/Virginia Tech Benchmark Experiments for CFD Validation". In: *AIAA Scitech 2020 Forum*. 2020. DOI: 10.2514/6.2020-1584. eprint: https://arc.aiaa.org/doi/pdf/10.2514/6.2020-1584. URL: https://arc.aiaa.org/doi/abs/10.2514/6.2020-1584.

[24] Máté Szoke et al. "Developing a Numerical Model of the Virginia Tech Stability Wind Tunnel for Uncertainty Quantification Based On Real-World Geometry". In: *AIAA Scitech 2020 Forum*. 2020. DOI: 10.2514/6.2020-0343. eprint: https://arc.aiaa.org/doi/pdf/10.2514/6.2020-0343. URL: https://arc.aiaa.org/doi/abs/10.2514/6.2020-0343.

[25] Vidya Vishwanathan et al. "Aerodynamic Design and Validation of a Contraction Profile for Flow Field Improvement and Uncertainty Quantification in a Subsonic Wind Tunnel". In: *AIAA Scitech 2020 Forum*. 2020. DOI: 10.2514/6.2020-2211. eprint: https://arc.aiaa.org/doi/pdf/10.2514/6.2020-2211. URL: https://arc.aiaa.org/doi/abs/10.2514/6.2020-2211.

[26] Aldo Gargiulo et al. "Flow Field Features of the BEVERLI Hill Model". In: *AIAA Scitech 2021 Forum*. DOI: 10.2514/6.2021-1741. eprint: https://arc.aiaa.org/doi/pdf/10.2514/6.2021-1741. URL: https://arc.aiaa.org/doi/abs/10.2514/6.2021-1741.

[27] Jeffrey P Slotnick. "Integrated CFD validation experiments for prediction of turbulent separated flows for subsonic transport aircraft". In: In NATO Science and Technology Organization, Meeting Proceedings RDP, STO-MP-AVT-307. 2019.

[28] Prahladh S. Iyer and Mujeeb R. Malik. "Wall-modeled LES of flow over a Gaussian bump". In: *AIAA Scitech 2021 Forum*. DOI: 10.2514/6.2021-1438. eprint: https://arc.aiaa.org/doi/pdf/10.2514/6.2021-1438. URL: https://arc.aiaa.org/doi/abs/10.2514/6.2021-1438.

[29] James R. Wright et al. "Unstructured LES_DNS of a Turbulent Boundary Layer over a Gaussian Bump". In: *AIAA Scitech 2021 Forum*. DOI: 10.2514/6.2021-1746. eprint: https://arc.aiaa.org/doi/pdf/10.2514/6.2021-1746. URL: https://arc.aiaa.org/doi/abs/10.2514/6.2021-1746.

[30] Riccardo Balin, Kenneth E. Jansen, and Philippe R. Spalart. "Wall-Modeled LES of Flow over a Gaussian Bump with Strong Pressure Gradients and Separation". In: *AIAA AVIATION 2020 FORUM*. DOI: 10.2514/6.2020-3012. eprint: https://arc.aiaa.org/doi/pdf/10.2514/6.2020-3012. URL: https://arc.aiaa.org/doi/abs/10.2514/6.2020-3012.

[31] Riccardo Balin. "Physics and Modeling of Turbulent Boundary Layer Flows Under Strong Pressure Gradients". English. PhD thesis. 2020, p. 207. ISBN: 9798557024402. URL: https://search.proquest.com/dissertations-theses/physics-modeling-turbulent-boundary-layer-flows/docview/2474939608/se-2?accountid=14784.

[32] Ali Uzun and Mujeeb R. Malik. "Simulation of a Turbulent Flow Subjected to Favorable and Adverse Pressure Gradients". In: *AIAA AVIATION 2020 FORUM*. DOI: 10.2514/6.2020-3061. eprint: https://arc.aiaa.org/doi/pdf/10.2514/6.2020-3061. URL: https://arc.aiaa.org/doi/abs/10.2514/6.2020-3061.

[33] UW Facility Management, Design Division. *Aerodynamics Lab Building Remodel Project 010-16403*. Tech. rep. 1992.

[34] JenCoFan. *Downblast Direct Drive Centrifugal Roof Exhaust Fans*. "Online; accessed 21-Jan-2021". 2020.

[35] Engineering Laboratory Design, Inc. *Instruction Manual, 36" Open Circuit Wind Tunnel*. Tech. rep. Jan. 2000.

[36] International Electrotechnical Commission. "IEC 60584-1 Ed. 3.0 b:2013, Thermocouples Part 1 EMF Specifications And Tolerances". In: (). "Online; accessed from https://www.thermocoupleinfo.com/thermocouple-accuracies.htm, 21-Jan-2021".

[37] John Robert Taylor. *An introduction to error analysis: the study of uncertainties in physical measurements*. University Science Books, 1997.

[38] Chauvete and Sons. "Hurricane 1800 Flex User Manual, Version 3". In: (2019).

[39] LaVision Inc. "Image sCMOS Datasheet". In: (Mar. 2018).

[40] Quantel, by Lumibird. "EverGreen 200 Laser Datasheet". In: (Jan. 2014).

[41] LaVision Inc. "Programmable Timing Unit (PTU X) Product Manual". In: (Nov. 2020).

[42] L. Adrian, R.J. Adrian, and J. Westerweel. *Particle Image Velocimetry*. Cambridge Aerospace Series. Cambridge University Press, 2011. ISBN: 9780521440080. URL: https://books.google.com/books?id=jbDl2-yHbooC.

[43] J. Westerweel and F. Scarano. "Universal outlier detection for PIV data". In: *Experiments in Fluids* 39 (Dec. 2005), pp. 1096–1100. DOI: 10.1007/s00348-005-0016-6.

[44] J. Westerweel. *Digital particle image velocimetry: theory and application*. Delft University Press, 1993.

[45] J. Westerweel. "Efficient Detection of Spurious Vectors in Particle Image Velocimetry data Sets". In: *Experiments in Fluids* 16 (1994), pp. 236–247.

[46] B. Wieneke. "PIV anisotropic denoising using uncertainty quantification". In: *Experiments in Fluids* 58.8, 94 (Aug. 2017), p. 94. DOI: 10.1007/s00348-017-2376-0.

[47] "Standard: Assessment of Experimental Uncertainty With Application to Wind Tunnel Testing (AIAA S-071A-1999)". In: *Standard: Assessment of Experimental Uncertainty With Application to Wind Tunnel Testing (AIAA S-071A-1999)*. 1999. DOI: 10.2514/4.473647.001. eprint: https://arc.aiaa.org/doi/pdf/10.2514/4.473647.001. URL: https://arc.aiaa.org/doi/abs/10.2514/4.473647.001.

[48] Bernhard Wieneke. "PIV uncertainty quantification from correlation statistics". In: *Measurement Science and Technology* 26.7 (June 2015), p. 074002. DOI: 10.1088/0957-0233/26/7/074002. URL: https://doi.org/10.1088/0957-0233/26/7/074002.

[49] Andrea Sciacchitano and Bernhard Wieneke. "PIV uncertainty propagation". In: *Measurement Science and Technology* 27.8 (June 2016), p. 084006. DOI: 10.1088/0957-0233/27/8/084006. URL: https://doi.org/10.1088/0957-0233/27/8/084006.

[50] Matthew N. Rhode and William L. Oberkampf. "Estimation of Uncertainties for a Model Validation Experiment in a Wind Tunnel". In: *Journal of Spacecraft and Rockets*

54.1 (2017), pp. 155–168. DOI: 10.2514/1.A33563. eprint: https://doi.org/10.2514/1.A33563. URL: https://doi.org/10.2514/1.A33563.

[51] Omega Engineering. “Pressure Transducer Manual M1436/0902”. In: (). "Online; accessed from: https://assets.omega.com/manuals/M1436.pdf, 22-Jan-2021".

[52] MKS Instruments. “226A/228A Baratron® Pressure Transducer Manual (1028109-001)”. In: (). "Online; accessed from: https://www.mksinst.com/f/226a-differential-capacitance-manometers, 22-Jan-2021".

[53] National Instruments. “NI 9485 Datasheet”. In: (May 2015). "Online; accessed from https://www.ni.com/pdf/manuals/374820a$_0$2.*pdf*, $23 - Jan - 2021$”.

[54] National Instruments. “NI 9213 Datasheet”. In: (Jan. 2017). "Online; accessed from https://www.ni.com/pdf/manuals/374916a$_0$2.*pdf*, $23 - Jan - 2021$”.

[55] National Instruments. “NI 9205 Datasheet”. In: (July 2017). "Online; accessed from https://www.ni.com/pdf/manuals/378020a$_0$2.*pdf*, $23 - Jan - 2021$”.

[56] National Instruments. “NI 6361 Device Specifications”. In: (Sept. 2015). "Online; accessed from https://www.ni.com/pdf/manuals/374650c.pdf, 23-Jan-2021".

[57] LaVision Inc. “3D Calibration Plate”. In: (Mar. 2019).

[58] Velmex, Inc. *Belt-Driven BiSlide Assembly*. "Online; accessed from https:// www.velmex.com/Produc $Feb - 2021$”.

[59] Velmex, Inc. *BiSlide Specifications*. "Online; accessed from https://www.velmex.com /Products/BiSlide/BiSlide$_M$*otorized.html?tab* $= 3TabbedPanels1, 1 - Feb - 2021$”.

[60] Debb Gould Architects. *Boeing Aerodynamics Laboratory Plans*. "Online; accessed from UW Facilities Record Lookup 21-Jan-2021". 1917.

[61] *44000 Thermistor Elements*. 44000. Omega. URL: https://assets.omega.com/spec/44000_THERMIS_ELEMENTS.pdf.

Appendix A

EQUIPMENT AND FACILITY SPECIFICATIONS

A.1 Manufacturer Data

Table A.1: Omega PX653 pressure sensor manufacturer specifications [51].

Excitation (Vdc)	12 to 36
Output (Vdc)	1 to 5
Linearity (%FS)	0.3
Hysteresis (%FS)	0.02
Repeatability (%FS)	0.05
Operating Temperature (°C)	-29 to 72
Compensated Temperature (°C)	2 to 57
Thermal Effects (zero) (%FS/°F)	0.015
Thermal Effects (span) (%rdg/°F)	0.015
Proof Pressure (psi)	15
Burst Pressure (psi)	20
Static Pressure (psi)	25
Gage Type	Capacitance
Supply Current (mA)	<5
Response Time (ms)	250

Table A.2: Baratron 226A pressure sensor manufacturer specifications [52].

Resolution (% FS)	0.01
Accuracy (% FS)	0.30
Temperature Coefficient (Zero) (% FS/°C)	0.1
Temperature Coefficient (Span) (% FS/°C)	0.04
Ambient Operating Temperature (°C)	0 to 50
Maximum Overpressure (Measurement)	120%FS or 20 psi (higher)
Maximum Overpressure (Reference) (%FS)	120
Maximum Line Pressure (psig)	40

Table A.3: NI 9485 solid-state relay digital output module manufacturer output characteristics [53].

Relay type	Normally open solid-state relay (SSR)
Switching voltage	60 Vdc max, 30 Vrms max
Switching current, per channel (A)	1.2 max
Switching rate (90% duty cycle)	1 operation per second
Relay open time (ms)	0.5 typ
Relay close time (ms)	9.0 typ
On resistance (mΩ)	200 max
Off stage leakage (μA)	30 typ
MTBF (hours at 25 °C)	2,172,740

Table A.4: NI cDAQ 9213 thermocouple module manufacturer input specifications and accuracy (high-resolution mode, 25 °C, type K thermocouple) [54].

ADC resolution (bits)	24
Type of ADC	Delta-Sigma
Sampling Mode	Scanned
Voltage measurement range (mV)	±78.125
Conversion time (per channel) (ms)	55
Sample rate (all channels) (S/s)	1
Input bandwidth (Hz)	14.4
Noise rejection (dB)	60
Differential input impedance (MΩ)	78
Input noise (nVrms)	200
Gain error	0.03% typical
Offset error (μV)	4 typical, 6 maximum
Offset error from source impedance	Add 0.55 μV/Ω when >50Ω
Cold-junction compensation accuracy (°C)	0.8 typical, 1.7 maximum
Measurement sensitivity (°C)	<0.02

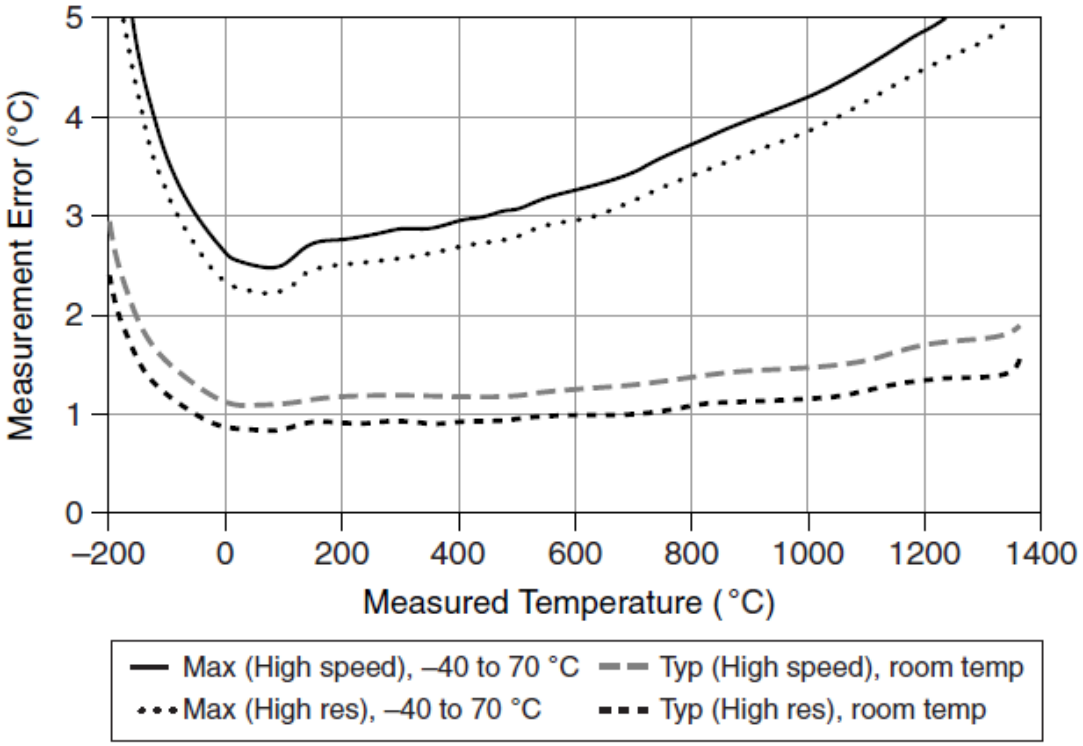

Figure A.1: NI cDAQ 9213 thermocouple Type K measurement error (accounts for gain errors, offset errors, differential and integral nonlinearity, quantization errors, noise errors, 50 Ω lead wire resistance, and cold-junction compensation errors. Does not account for accuracy of thermocouple itself) [54].

.

Table A.5: NI cDAQ 9205 voltage input module manufacturer analog input and accuracy specifications (± 5V input) [55].

ADC resolution (bits)	16
DNL	No missing codes guaranteed
Conversion time (μs)	4.00 (250 kS/s)
Input coupling	DC
Input impedance (GΩ)	<10 in parallel with 100 pF
Input bias current (pA)	±100
Crosstalk, at 100 kHz (adjacent channels) (dB)	-65
Analog bandwidth (kHz)	370
Scaling coefficient (muV/LSB)	164.2
CMRR, DC to 60 Hz (dB)	100
Accuracy at full-scale (μV)	3,230
Random noise (μV RMS)	121
Sensitivity (μV)	46.4
Residual gain error (ppm of reading)	135
Gain tempco (ppm/°C)	11
Reference tempco (ppm/°C)	5
Residual offset error (ppm of range)	20
Offset tempco (ppm of range /°C)	47
INL error (ppm of range)	76

Table A.6: NI PCIe 6361 voltage DAQ manufacturer analog input and accuracy specifications (± 10V input) [56].

ADC resolution (bits)	16
DNL	No missing codes guaranteed
Sample Rate (MS/s)	2.00 maximum
Timing resolution (ns)	10
Timing accuracy (ppm of sample rate)	50
Input coupling	DC
CMRR, DC to 60 Hz (dB)	100
Input impedance (GΩ)	<10 in parallel with 100 pF
Input bias current (pA)	±100
Crosstalk, at 100 kHz (adjacent channels) (dB)	-75
Small signal bandwidth (-3 dB) (MHz)	1.7
Input FIFO size (samples)	2,047
Data transfers	DMA (scatter-gather), programmed I/O
Settling time (±60 ppm of Step) (μs)	1
Residual gain error (ppm of reading)	48
Residual offset error (ppm of range)	13
Offset tempco (ppm of range /°C)	21
Random noise (μV RMS)	315
Absolute accuracy at full-scale (μV)	1,660
Gain tempco (ppm/°C)	13
Reference tempco (ppm/°C)	1
Sensitivity (μV)	46.4
INL error (ppm of range)	60

Table A.7: Programmable Timing Unit (PTU X) sequencer I/O specifications [41].

Output drivers (Ω)	TTL 50
Time resolution (ns)	10
Typical jitter between all outputs (ns)	< 1
Jitter to external signals (ns)	$\pm$ 5
Trigger source	generator, external TTL input
Frequency strategy	direct static
Frequency generator range	0.01 Hz - 1 MHz
Reference times	1, 8
Digital inputs (kΩ)	TTL programmable polarity, 2.7 to GND

Table A.8: Imager sCMOS camera general system specifications [39].

Double shutter	two images with 120 ns (min) interframe time
Exposure time	15 μs - 100 ms
Digital output (bit)	16
Interface	Frame grabber CLHS optical for PCIe 4 x slot
Lens mount	F-mount (optional C-mount)
Number of pixels	2560 x 2160
Pixel size (μm)	6.5 x 6.5
Active area (mm)	16.6 x 14.0
Spectral range (nm)	370 - 1100
Quantum efficiency	typ. 53% @ 532 nm
Full well capacity (e^-)	30,000
Readout noise (e^-)	< 3 @ 286 MHz
Frame rate (fps)	50

Table A.9: LaVision 3D calibration target specifications [57].

	SFOV	LFOV
Type	058-5	204-15
Dimensions (mm)	58 x 58	204 x 204
Dot distance (mm)	5	15
Dot diameter (mm)	1.2	3.2
Level separation (mm)	1	3

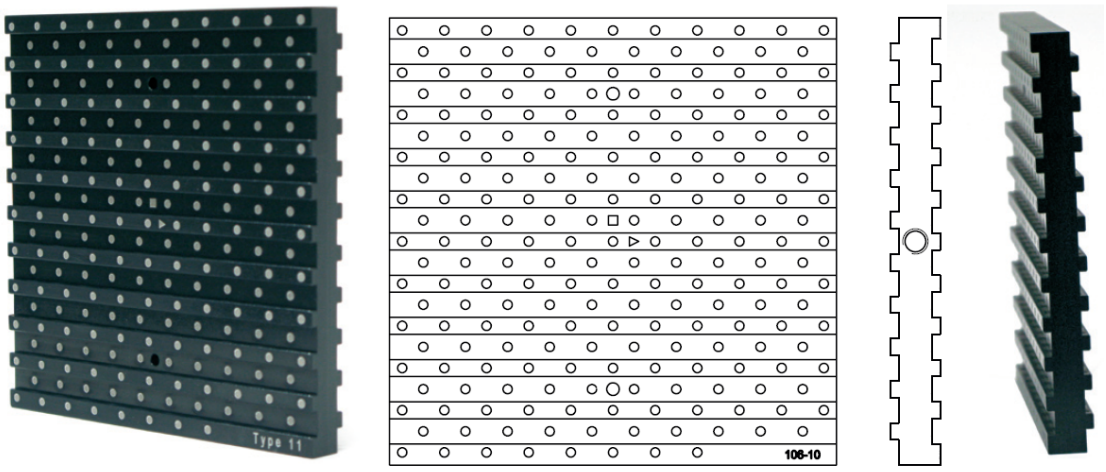

Figure A.2: Calibration target depiction (actual size not pictured) [57].

Table A.10: EverGreen 200 laser general system specifications [40].

Wavelength (nm)	532
Pulse repetition rate (Hz)	15
Energy (mJ)	200
Pulse-to-pulse energy stability	< 2 % RMS
Energy drift over 8 hours	10 %
Pulse width (ns)	≤ 10
Near field beam diameter (mm)	< 6.35
Beam divergence (mrad)	< 4
Shot to shot point stability (μrad)	< 100
Far field beam overlap (μrad)	$\pm$ 100
Near field beam overlap (μrad)	$\pm$ 100
Polarization	linearly polarized, vertical
Spectral purity	> 98 %
Near field beam profile	flat-top, uniform

Table A.11: Velmex BiSlide specifications for camera/laser traverse [58, 59].

	Streamwise (x)	Spanwise (y)	Vertical (z)
Model	MB10-1000-M10-33,20	MN10-0400-M02-31,20	MN10-0150-M02-21
Drive	Belt	Lead Screw	
Travel (in)	100	40	15
Motor	Vexta PK296		Vexta PK264
Controller	VXM-2		VXM-1
Advance per step (mm)	0.03 mm	5 μm	
Repeatability (in)	0.0002		
Straight line accuracy	0.0007 in/ 10 in	0.003 in/ entire travel	

A.2 Equipment Calibrations

Table A.12: Baratron 226A (20 Torr range) pressure sensor (type 226A21TFFFFFU2A1) calibration report. Calibrated on 20 June 2018 with UUT S/N 022435190.

Pressure (Torr)	Voltage Std	Voltage UUT	Error (mV)	Error (%)
0.00	0.00	0.00	0.00	0.00
2.01	1.00	1.01	5.00	0.05
4.03	2.01	2.03	15.00	0.15
8.05	4.03	4.05	21.00	0.21
11.98	5.99	6.01	19.00	0.19
15.92	7.96	7.95	10.00	0.10
19.99	10.00	9.97	30.00	-.30

Table A.13: Baratron 226A (50 Torr range) pressure sensor (type 226A51TFFFFFU2A1) calibration report. Calibrated on 12 June 2020 with UUT S/N 022764957.

Pressure (Torr)	Voltage Std	Voltage UUT	Error (mV)	Error (%)
0.00	0.00	0.00	0.00	0.00
5.01	1.00	1.00	3.00	0.03
10.00	2.00	2.01	5.00	0.05
19.99	4.00	4.01	7.00	0.07
29.97	5.99	6.01	13.00	0.13
10.01	8.00	8.02	15.00	0.15
49.65	9.93	9.95	24.00	0.24

Table A.14: Omega PX653-10D5V (0-10 "WC range) pressure sensor (S/N X16380087) calibration report. Calibrated on 21 Sept 2016.

Pressure ("WC)	Output VDC	% Error (Span)	% Error (BSL)
-0.00018	1.001	0.03%	0.00%
2.50069	2.002	0.04%	0.03%
4.99958	2.999	-0.02%	-0.01%
7.49821	3.997	-0.06%	-0.03%
9.99997	4.999	-0.01%	0.04%
7.49877	3.997	-0.06%	-0.03%
5.00019	2.999	-0.02%	-0.01%
2.50087	2.002	0.03%	0.02%
-0.00033	1.001	0.03%	-0.01%

Table A.15: EverGreen 200 laser system as-measured calibration and beam parameters, courtesy of Quantel by Lumibird.

	Laser 1	Laser 2
Wavelength (nm)	532	532
Energy (mJ)	211	202
Near Field Beam Diameter (mm)	5.54	5.60
Spec Energy Voltage (V)	602	583
Voltage Min (V)	497	487
Voltage Limit (V)	608	589
Q-Switch Delay (μs)	135	135

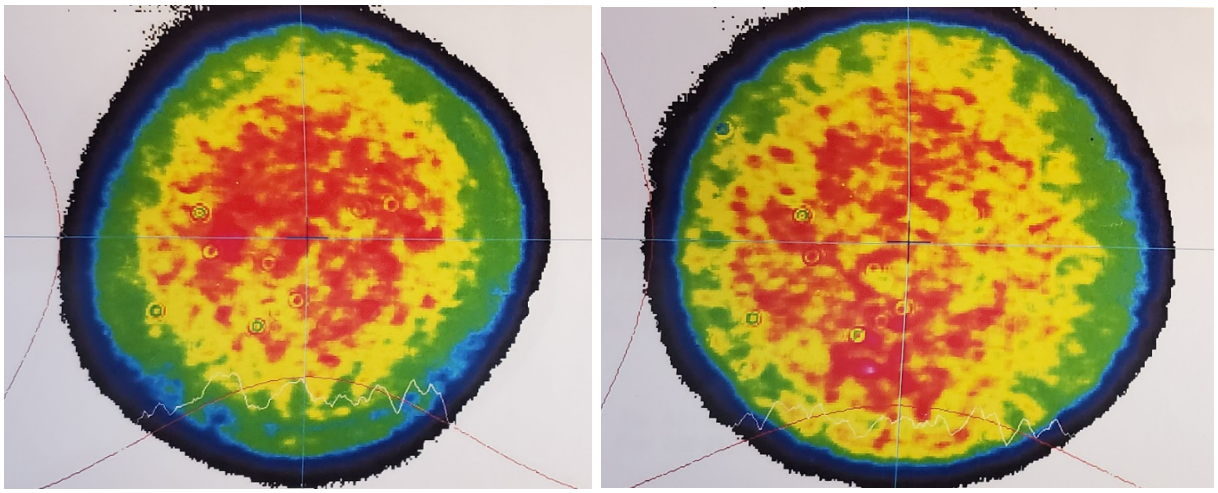

(a) (b)

Figure A.3: Evergreen 200 actual laser beam profile for (a) laser 1 and (b) laser 2.

.

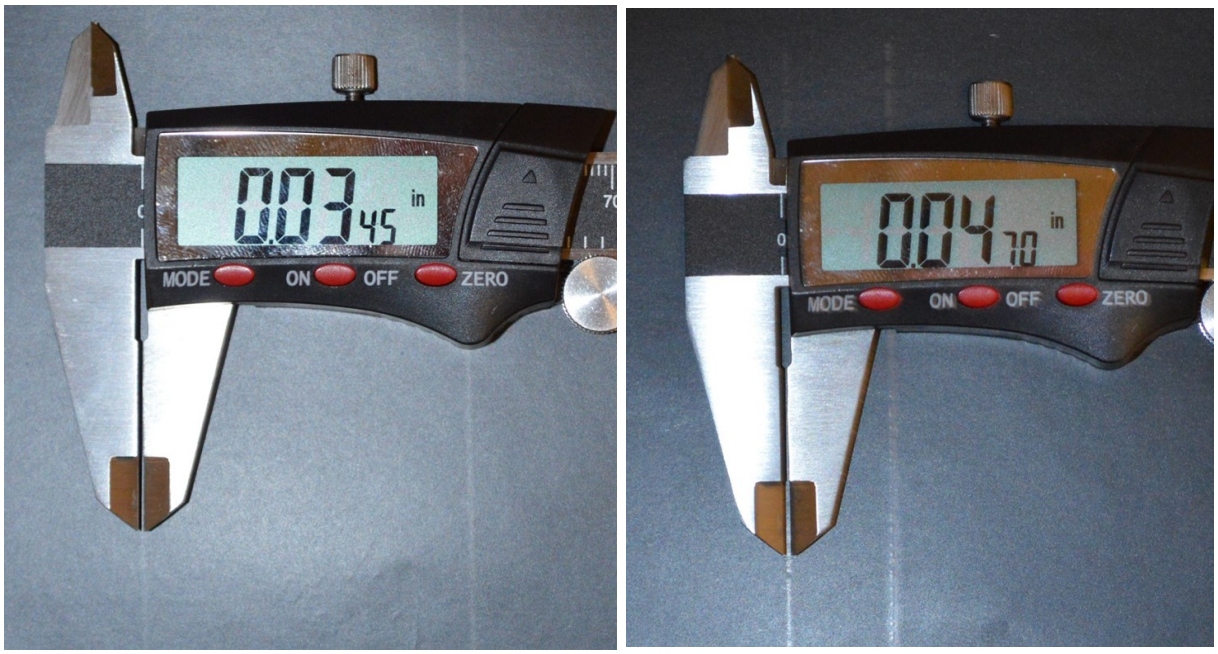

(a) (b)

Figure A.4: Laser sheet thicknesses on burn paper for (a) large field of view and (b) small field of view testing. Max energy at 15 Hz for 5 seconds.

.

Table A.16: PIV image calibrations for small and large fields of view (SFOV/LFOV). Pixel locations referenced to upper left corner of image.

	SFOV	LFOV
Mapping function	Pinhole	Pinhole
Fit error (pixels)	0.7439	20.4292
Size of dewarped image (pixels)	2559 x 2159	2575 x 2170
Camera translation offset (mm)	(-25.05, 25.79)	(-117.14, 103.21)
Camera rotation	(-0.98, 0.95, 0.02)°	(0.33, -1.54, 0.11)°
Image distortion principal point (pixels)	(1279.50, 1079.50)	(1493.85, 823.95)
Radial distortion, κ_1	N/A	4.46685
Radial distortion, κ_2	N/A	24159.6
Tangential distortion, ρ_1	N/A	-0.0231455
Tangential distortion, ρ_2	N/A	0.071932
Camera focal length (mm)	53809441.31	757.88
Pixel size (mm)	0.0065	0.0065
Pixel aspect ratio	1	1
Image origin (pixel)	(315.24, 2070.44)	(113.03, 2047.48)
Scale factor (pixel/mm)	38.44	11.84

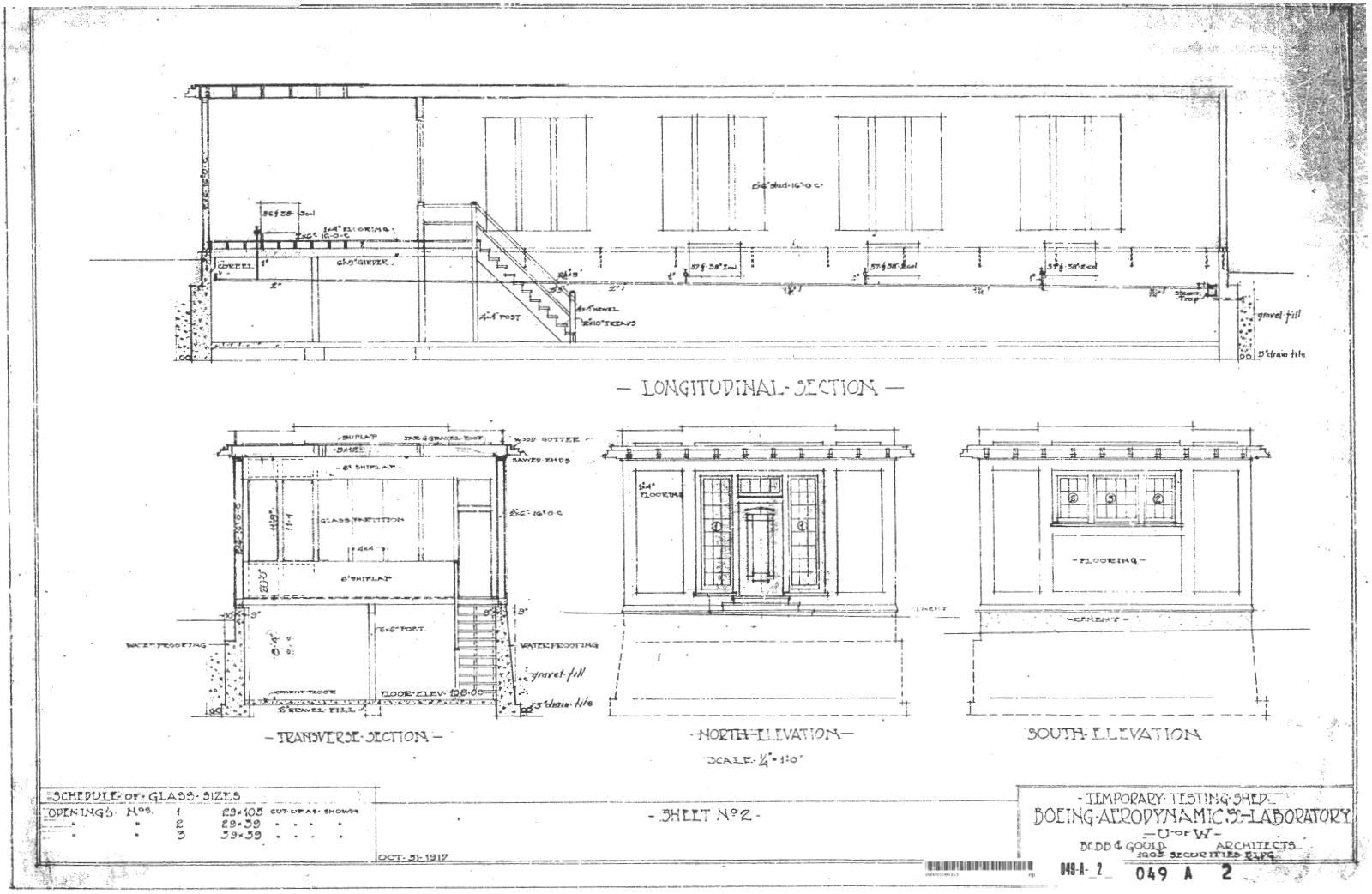

Figure A.5: Side view of Boeing Aeronautics Laboratory, 1917. North office since removed. [60]

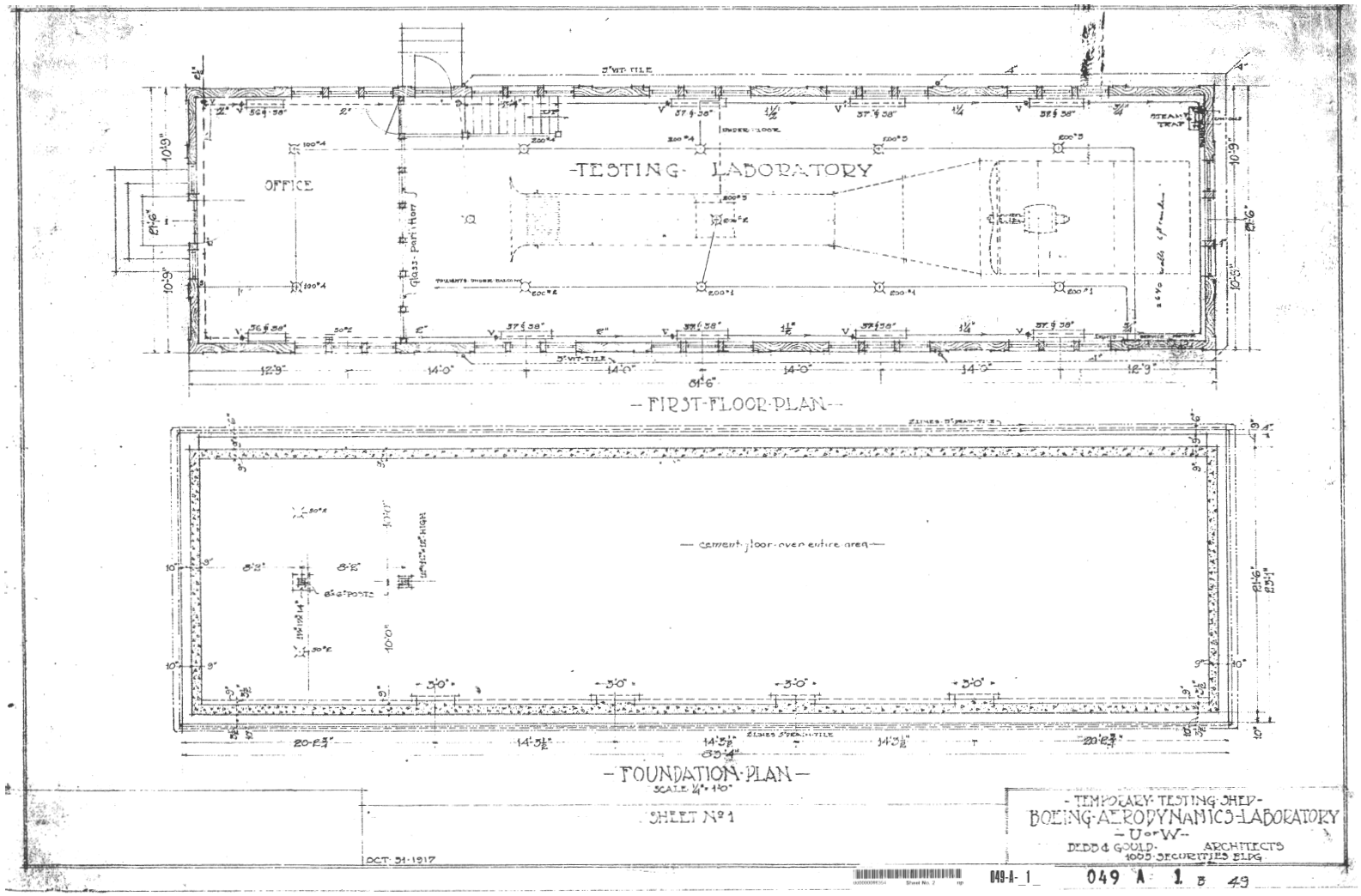

Figure A.6: Plan view of Boeing Aeronautics Laboratory, 1917. North office since removed, wind tunnel upgraded [60].

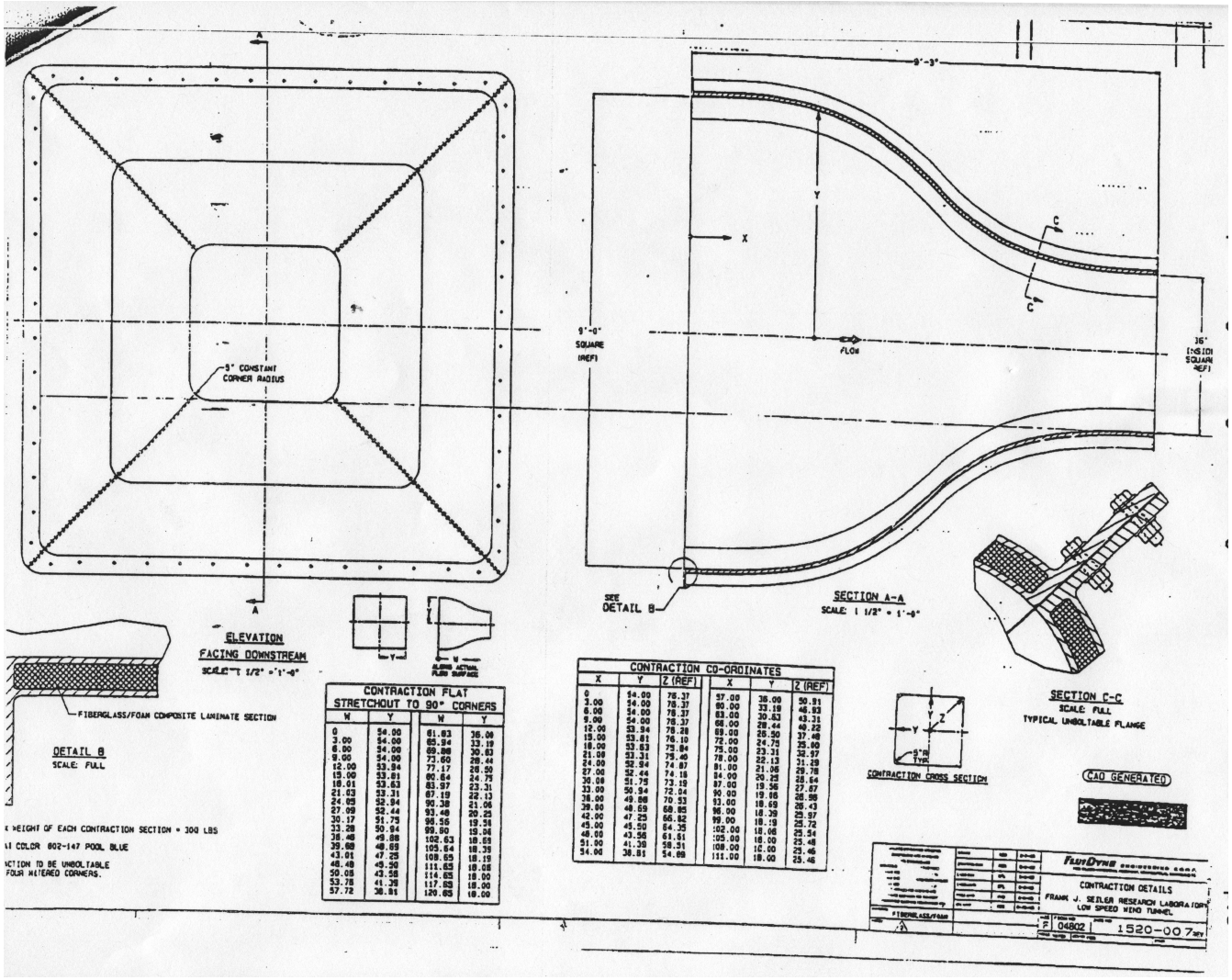

Figure A.7: Front and side view drawings of the tunnel inlet, including coordinates. Schematic provided from an identical tunnel located at the United States Air Force Academy [35].

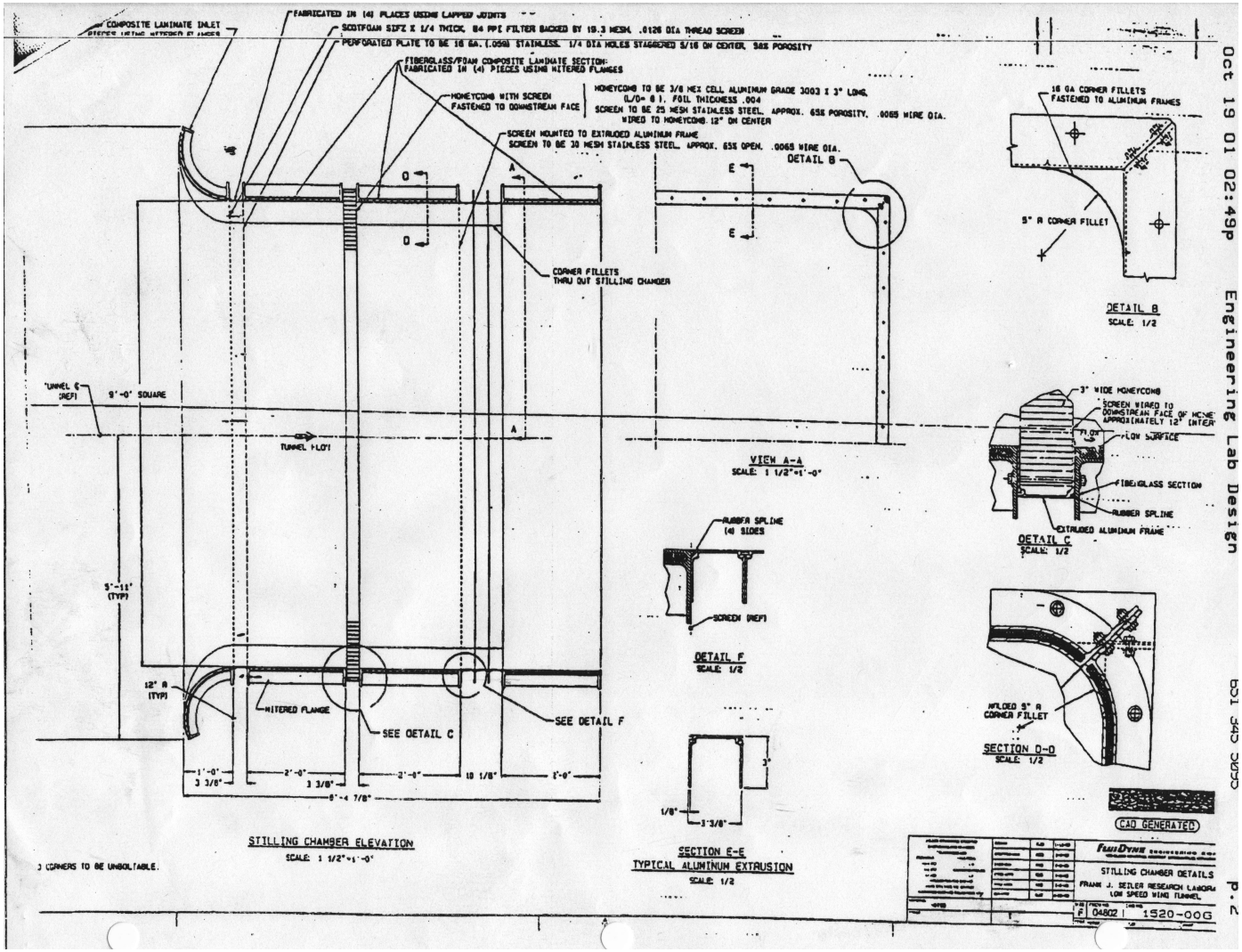

Figure A.8: Top view drawing of the tunnel inlet. Schematic provided from an identical tunnel located at the United States Air Force Academy [35].

A.3 Speed-Bump Pressure Tap Locations

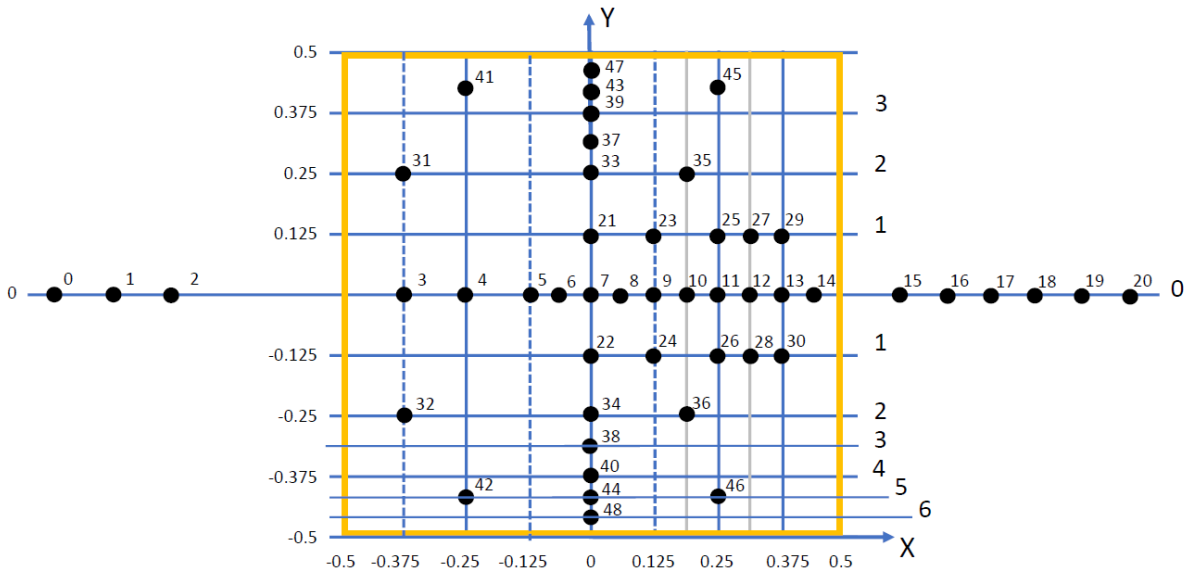

Figure A.9: Splitter plate and speed-bump pressure tap numbering system and locations. All dimensions as a fraction of $L_b = 35.5$ inches[5].

Table A.17: Summary of pressure tap locations organized by spanwise plane number indicated in Fig. A.9 [5].

Tap No.	Plane	y/L_b	x/L_b	y/L	x/L
0	0	0.0000	-0.9261	0.0000	-0.9132
1		0.0000	-0.8415	0.0000	-0.8299
2		0.0000	-0.7570	0.0000	-0.7465
3		0.0000	-0.3750	0.0000	-0.3698
4		0.0000	-0.2500	0.0000	-0.2465
5		0.0000	-0.1250	0.0000	-0.1233
6		0.0000	-0.0625	0.0000	-0.0616
7		0.0000	0.0000	0.0000	0.0000
8		0.0000	0.0625	0.0000	0.0616
9		0.0000	0.1250	0.0000	0.1233
10		0.0000	0.1875	0.0000	0.1849
11		0.0000	0.2500	0.0000	0.2465
12		0.0000	0.3125	0.0000	0.3082
13		0.0000	0.3750	0.0000	0.3698
14		0.0000	0.4375	0.0000	0.4314
15		0.0000	0.5704	0.0000	0.5625
16		0.0000	0.6831	0.0000	0.6736
17		0.0000	0.7958	0.0000	0.7847
18		0.0000	0.9085	0.0000	0.8958
19		0.0000	1.0211	0.0000	1.0069
20		0.0000	1.1338	0.0000	1.1181
21	1	0.1250	0.0000	0.1233	0.0000
22		-0.1250	0.0000	-0.1233	0.0000
23		0.1250	0.1250	0.1233	0.1233

24		-0.1250	0.1250	-0.1233	0.1233
25		0.1250	0.2500	0.1233	0.2465
26		-0.1250	0.2500	-0.1233	0.2465
27		0.1250	0.3125	0.1233	0.3082
28		-0.1250	0.3125	-0.1233	0.3082
29		0.1250	0.3750	0.1233	0.3698
30		-0.1250	0.3750	-0.1233	0.3698
31	2	0.2500	-0.3750	0.2465	-0.3698
32		-0.2500	-0.3750	-0.2465	-0.3698
33		0.2500	0.0000	0.2465	0.0000
34		-0.2500	0.0000	-0.2465	0.0000
35		0.2500	0.1875	0.2465	0.1849
36		-0.2500	0.1875	-0.2465	0.1849
37	3	0.3125	0.0000	0.3082	0.0000
38		-0.3125	0.0000	-0.3082	0.0000
39	4	0.3750	0.0000	0.3698	0.0000
40		-0.3750	0.0000	-0.3698	0.0000
41	5	0.4625	-0.2500	0.4561	-0.2465
42		-0.4625	-0.2500	-0.4561	-0.2465
43		0.4625	0.0000	0.4561	0.0000
44		-0.4625	0.0000	-0.4561	0.0000
45		0.4625	0.2500	0.4561	0.2465
46		-0.4625	0.2500	-0.4561	0.2465
47	6	0.4750	0.0000	0.4684	0.0000
48		-0.4750	0.0000	-0.4684	0.0000

A.4 Pitot Rake Tube Locations and Drawings

Table A.18: Ordinate dimensions of troughs referenced to wall-end of bottom bar (i.e. wall-normal distance of pitot tubes).

Tube	Wall-Normal Distance (in)	Tube	Wall-Normal Distance (in)
1	0.033	16	1.647
2	0.098	17	2.023
3	0.163	18	2.506
4	0.228	19	3.126
5	0.293	20	3.922
6	0.358	21	5.330
7	0.423	22	6.738
8	0.488	23	8.145
9	0.553	24	9.553
10	0.618	25	10.961
11	0.702	26	12.369
12	0.810	27	13.777
13	0.948	28	15.184
14	1.126	29	16.592
15	1.354	30	18.000

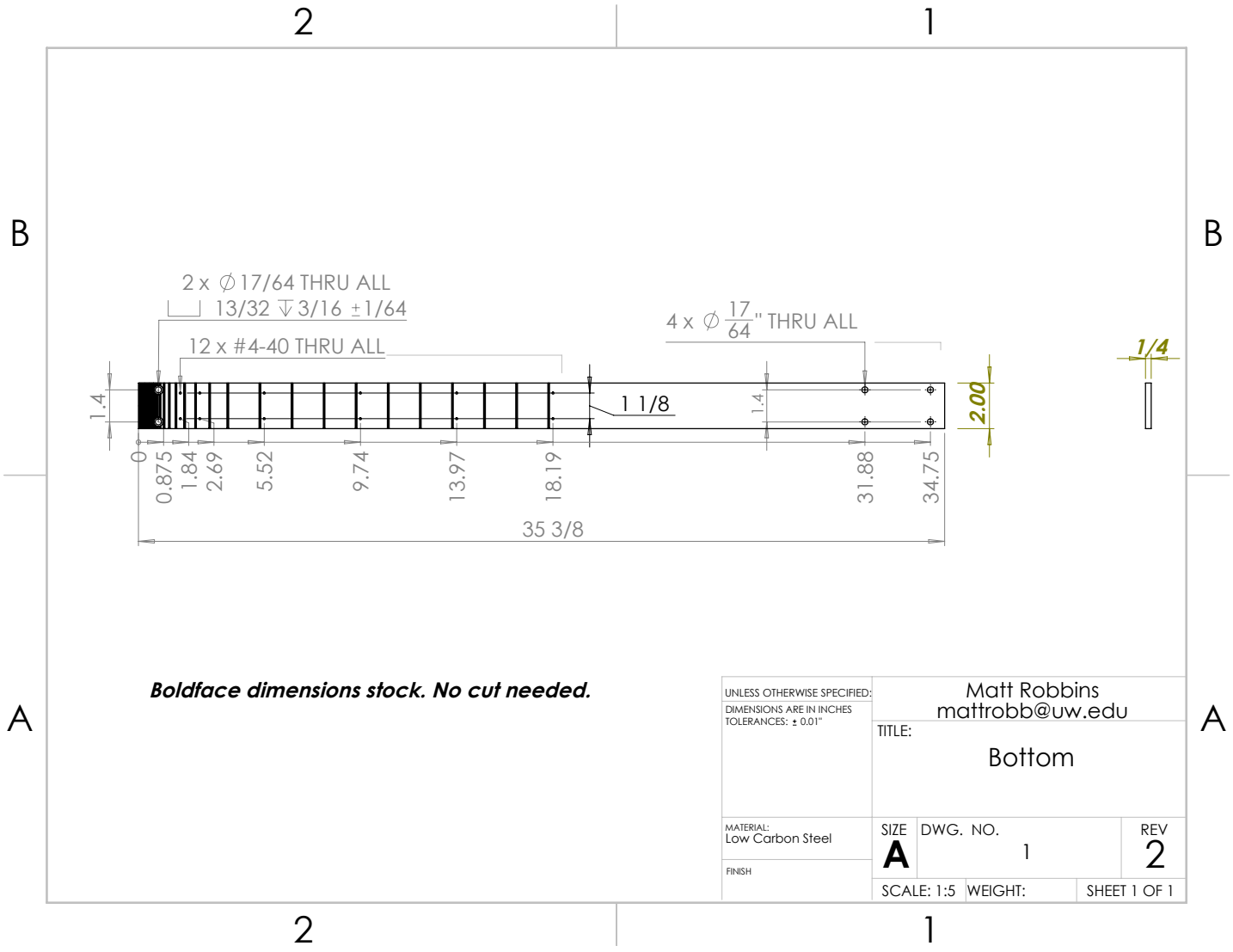

Figure A.10: Plan view of bottom bar of pitot rake.

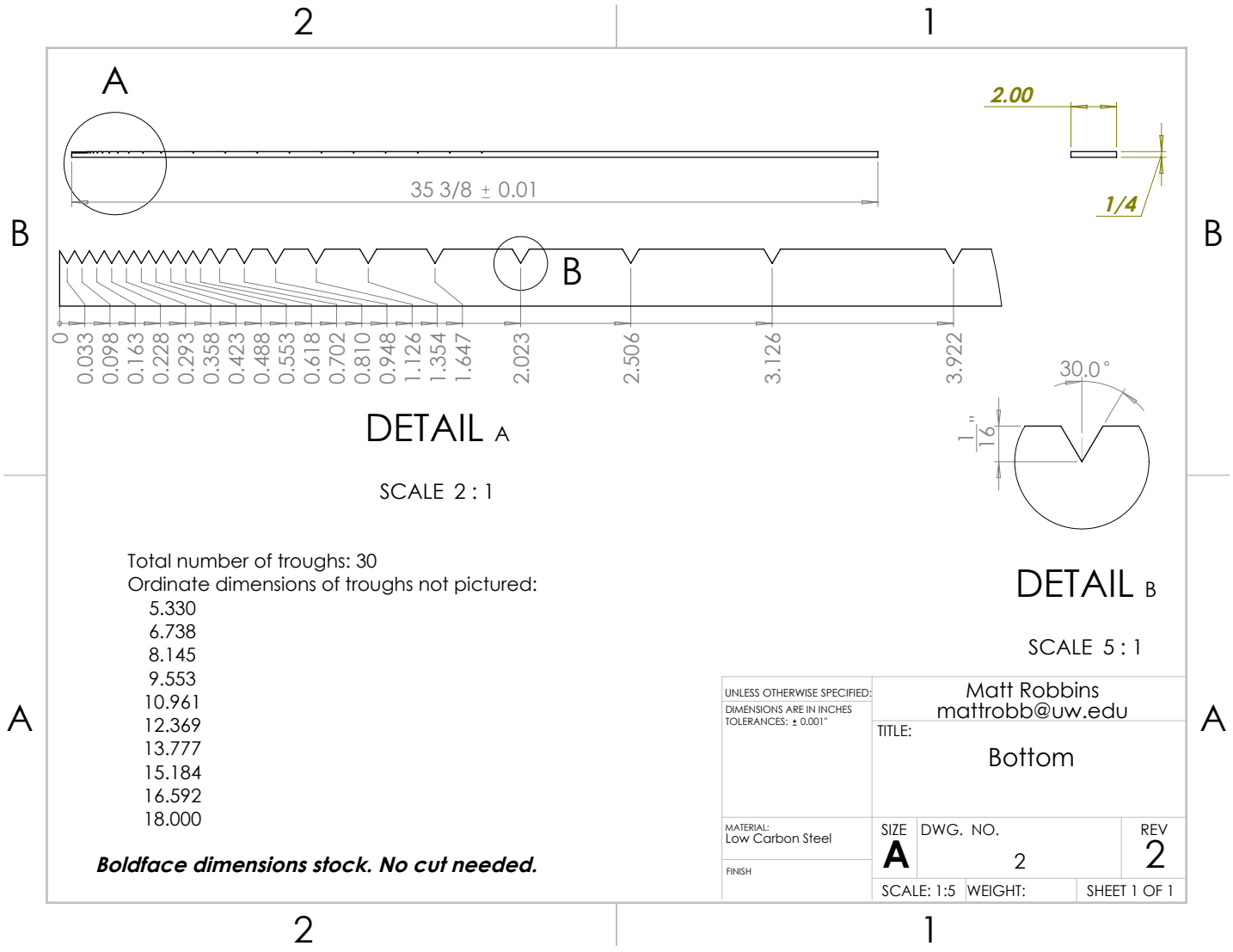

Figure A.11: Side view of bottom bar of pitot rake, including trough dimensions.

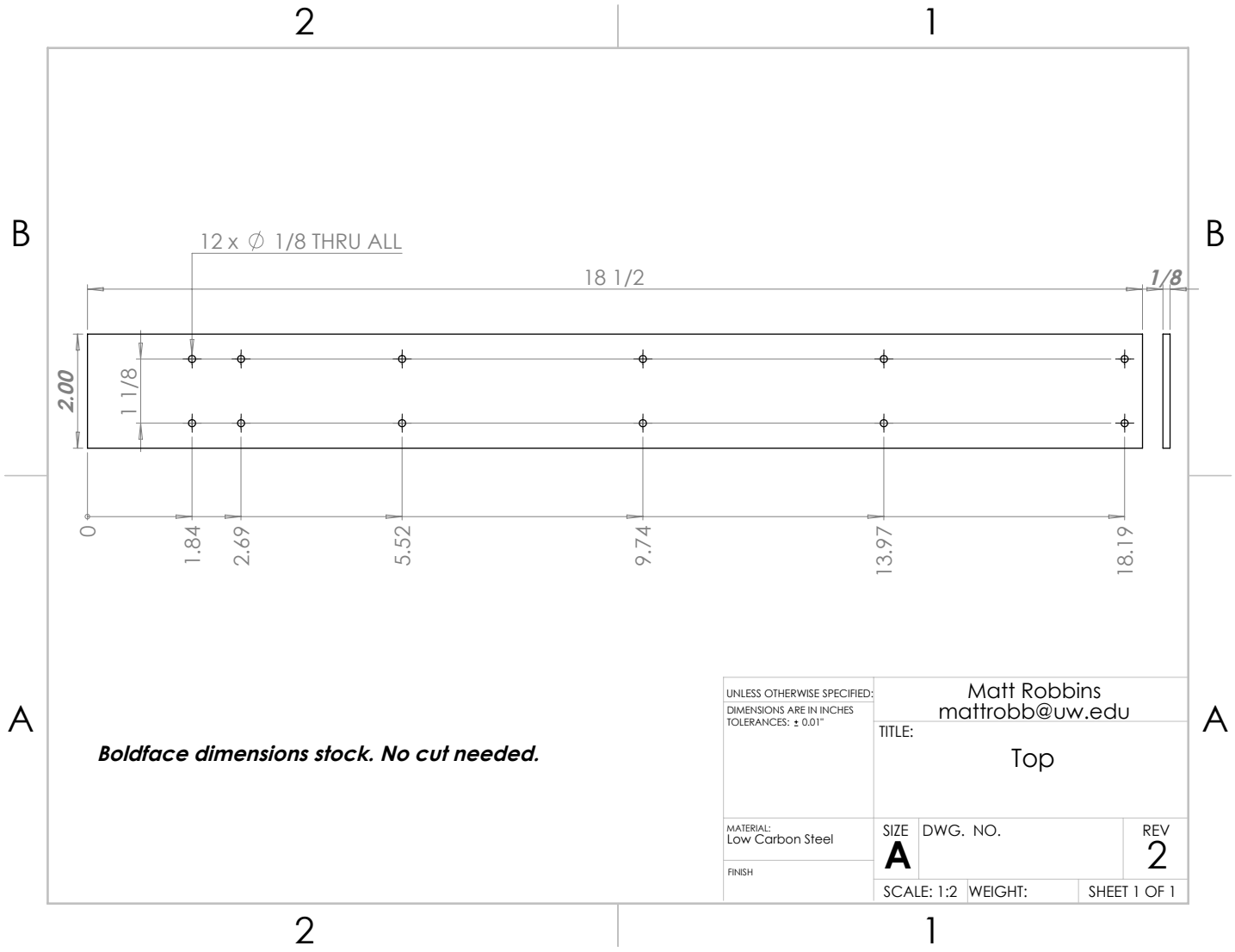

Figure A.12: Plan view of top/fastener bar of pitot rake.

Appendix B

THERMISTOR INTEGRATION PROPOSAL

While conventional wind tunnel configurations utilize thermocouples, the nature of this validation test campaign demands a temperature measurement method with superior resolution and accuracy. The following analysis is a proposal for the integration of a thermistor measurement system and serves as an example of the attention to uncertainty minimization required in the design of validation experiments. A negative temperature coefficient (NTC) thermistor is considered in this analysis as it provides excellent accuracy, stability, and time response over the nominal temperature range of testing.

Thermistors consist of semiconducting material with a resistivity that is highly dependent on temperature. Thus, when implemented in a circuit, thermistors behave as resistors that vary with the temperature of the fluid it is immersed in. The Wheatstone bridge circuit depicted in Fig. B.1 can be employed to optimize temperature resolution, sensitivity, and error minimization.

When R_{drop}, R_1, R_2, and R_3 are known, the thermistor resistance, R_{th}, can be determined by measuring the ratio of the voltage between the two legs of the Wheatstone bridge, V, to the voltage across the entire bridge, V_{ref}:

$$R_{th} = \frac{V_{ref} - V_{th}}{V_{th}} R_{ref} \tag{B.1}$$

The thermistor's resistance is then related to temperature by the Steinhart-Hart equation:

$$\frac{1}{T} = A + B[ln(R_{th})] + C[ln(R_{th})]^3 \tag{B.2}$$

where A, B, and C are calibration constants supplied by the manufacturer.

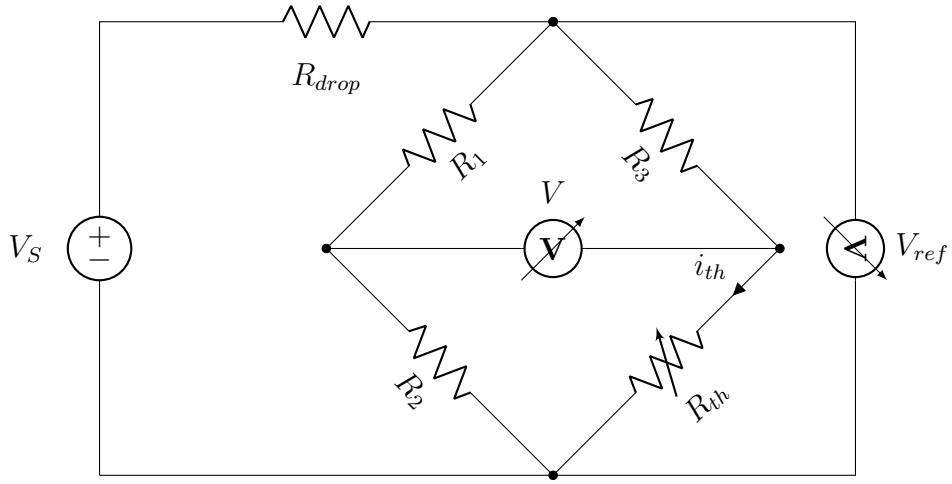

Figure B.1: Thermistor implemented in a ratiometric Wheatstone bridge circuit.

Important design considerations for a thermistor circuit include the supplied reference voltage, the reference resistance, the maximum current through the thermistor to avoid the effects of self-heating, and the nominal resistance of the thermistor. The latter is typically expressed as a resistance at 25°C ($R_{25°C}$). The two thermistors under consideration in this proposal are Omega models 44031 and 44032 with 10 $k\Omega$ and 30 $k\Omega$ nominal resistances respectively.

The choice of reference resistance impacts the sensitivity of the thermistor circuit at various temperature ranges. The voltage ratio, $\alpha = \frac{V_{th}}{V_{ref}}$, given by Eq. B.1, is plotted against temperature and its derivative (sensitivity) for each thermistor at three reference resistances in Fig. B.2. While both thermistor models are comparably sensitive in the nominal temperature range of the experiment (10 °C to 45 °C), a reference resistance equal to or slightly greater than the nominal thermistor resistance yields the maximum sensitivity.

The heat dissipated through the thermistor, or self-heating, is an important source of error that may bias the temperature reading. The amount of heat dissipated is proportional to the power through the thermistor and is given by Eq. B.3.

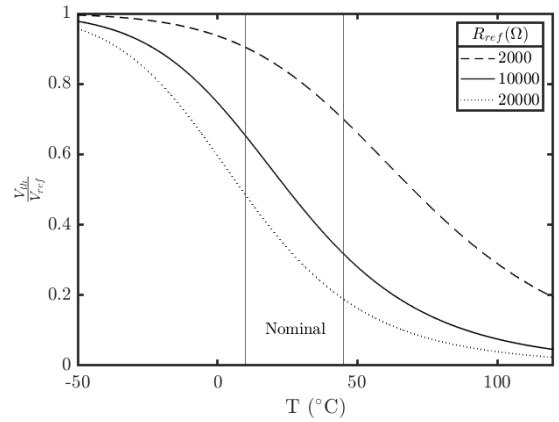

(a) Model 44031 ($R_{25} = 10k\Omega$)

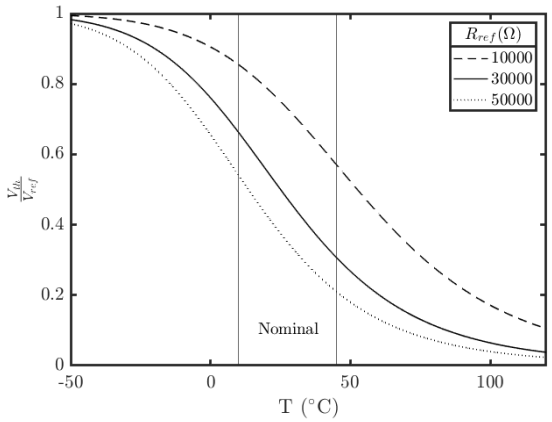

(b) Model 44032 ($R_{25} = 30k\Omega$)

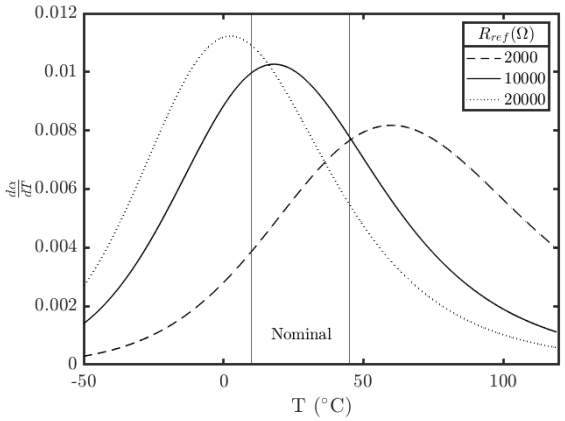

(c) Model 44031 sensitivity ($R_{25} = 10k\Omega$)

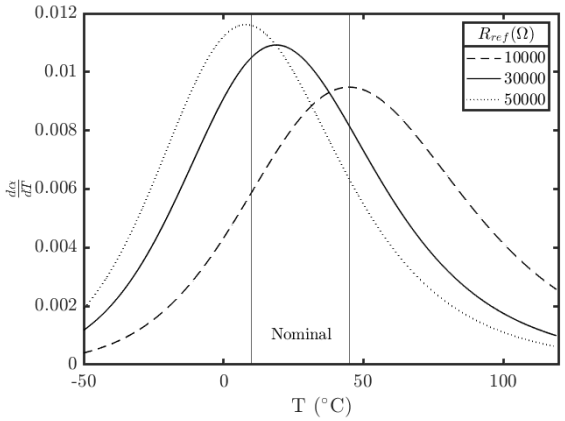

(d) Model 44032 sensitivity ($R_{25} = 30k\Omega$)

Figure B.2: Voltage ratio and sensitivity as a function of reference resistor setting and temperature.

$$P_{th} = I^2 R_{th} = \frac{V_{ref}^2}{(R_{ref} + R_{th})^2} R_{th} \tag{B.3}$$

If the reference resistance is set equal to the nominal thermistor resistance, self-heating can be minimized by either reducing the reference voltage or utilizing a thermistor with a larger nominal resistance. This consideration can be relaxed, however, if the operating current is

within the 10 to 15 μA range suggested by the manufacturer to avoid the effects of self-heating [61]. Assuming a current of 10 μA, the reference voltage required is determined by Ohm's Law. The corresponding voltage across the thermistor for both models, assuming the reference resistance is equal to the nominal thermistor resistance, is listed in Table B.2.

As a final consideration, the output voltages of Table B.2 are weighed against the analog-to-digital (ADC) sensitivity and accuracy of the data acquisition hardware (DAQ). A National Instruments^{TM} NI 6361 X Series data acquisition card with 16-bit analog input resolution and variable input range was used in this experiment (see Appendix A). The analog input voltage resolution, given by:

$$Res_{DAQ} = \frac{2^{16}}{V_{channel}} \tag{B.4}$$

and absolute accuracy supplied by the manufacturer as a function of channel input range is given in Table B.3.

Note, a thermistor with higher voltage sensitivity does not necessarily imply a higher overall measurement sensitivity if its output voltage requires a DAQ channel with larger range and thus lower resolution. Hence, how well the expected voltage output covers the range of the DAQ channel should be considered. The metric which takes this into account is the ADC temperature resolution, obtained by:

$$Res_T = (Res_{DAQ})\frac{dV_{th}}{dT}|_{25^\circ} \tag{B.5}$$

Additionally, an estimation of worst-case ADC accuracy can be determined by normalizing the full-scale absolute accuracy given by the manufacturer in Table B.3 with the maximum expected voltage ($V_{th,10^\circ C}$) from Table B.2, assuming a linear relationship between voltage and accuracy. Note that residual gain and offset errors have an increased effect at a lower input range.

The ADC temperature resolution using the 10 $k\Omega$ thermistor is 6.225 x 10^8 bits/°C with a worst-case absolute ADC accuracy of 34.7 μV, and the resolution for 30 $k\Omega$ is 7.995 x 10^8

Model	$R_{25°C}$ $(k\Omega)$	A	B	C
44031	10	1.032 x 10^{-3}	2.387 x 10^{-4}	1.580 x 10^{-7}
44032	30	9.376 x 10^{-4}	2.208 x 10^{-4}	1.276 x 10^{-7}

Table B.1: Nominal resistance and Steinhart-Hart constants for two Omega thermistors [61].

Model	V_{ref} (V)	$V_{th,10°C}$	$V_{th,25°C}$	$V_{th,45°C}$	$\lvert\frac{dV_{th}}{dT}\rvert_{25°}(\frac{\mu V}{°C})$
44031 ($R_{25°C} = 10000\Omega$)	0.200	0.131	0.100	0.064	1900
44032 ($R_{25°C} = 30000\Omega$)	0.600	0.397	0.300	0.184	6100

Table B.2: Expected thermistor voltage values for various temperatures.

Channel Range (V)	Res_{DAQ} $(\frac{bits}{mV})$	FS Absolute Accuracy (μV)
± 0.5	131.072	100
± 0.2	327.680	53

Table B.3: Resolution and absolute accuracy for NI 6361 DAQ analog input channels [56].

bits/°C with a worst-case absolute accuracy of 79.4 μV.

While the temperature resolution for the 30 $k\Omega$ thermistor is greater, for the purposes of this test campaign, the improved accuracy of the 10 $k\Omega$ thermistor is more important to reduce propagated uncertainty than resolving temperature with a higher resolution. Therefore, the optimal thermistor configuration for this test campaign is an Omega model 44031 thermistor in a voltage divider circuit with a reference resistance of 10 $k\Omega$ and a reference voltage of 0.200 volts.

Uncertainty

The following sources of uncertainty are considered in the measurement of temperature using a thermistor in a voltage divider circuit:

- Thermistor uncertainty, δ_{th} (°C). The thermistor uncertainty for the Omega model 44031 thermistor is specified by the manufacturer at the worst-case temperature (10 °C) as ± 33.8 Ω.

- Reference resistor uncertainty, δ_R (Ω). The resistor uncertainty for the Stackpole RNCF0603 reference resistor is specified by the manufacturer as ± 100 Ω.

- ADC uncertainty, δ_{ADC} (V). The ADC uncertainty is considered to be the quadratic sum of the worst-case (10°C) ADC absolute accuracy and digital resolution accuracy assuming a rectangular probability density function.

$$\delta_{ADC} = \sqrt{\left(\frac{(Res_{DAQ})^{-1}}{2\sqrt{3}}\right)^2 + (Absolute|_{10^\circ C})^2} = 3.47x10^{-7}V \tag{B.6}$$

In order to eliminate the effects of the power supply's uncertainty, the reference voltage can be measured ratiometrically with the output voltage across the thermistor. Thus, the measured ADC reading is:

$$ADC = \frac{V_{th}}{V_{ref}} \cdot 2^{16} \tag{B.7}$$

The reference voltage can be decreased slightly from the preceding analysis in order to ensure compatibility with a ± 0.2V DAQ channel. Substituting (B.7) into (B.1) and rearranging yields:

$$R_{th} = \left(\frac{2^{16}}{ADC} - 1 \right) \cdot R_{ref} \tag{B.8}$$

which can be substituted into (B.2) to compute temperature. The uncertainties of the coefficients A, B, and C are assumed to be contained in δ_{th}. Temperature uncertainty is then:

$$\delta_T = \sqrt{\left(\frac{\partial T}{\partial ADC} \delta_{ADC} \right)^2 + \left(\frac{\partial T}{\partial R_{ref}} \delta_{R_{ref}} \right)^2 + \delta_{th}^2} \tag{B.9}$$

Appendix C

UNCERTAINTY OF MEASURED AND DERIVED QUANTITIES

For a general statement of how uncertainty was treated in this experiment, see Section 3.5. The following text explains in detail how uncertainty was calculated for each measured and derived quantity in the experiment.

Measured Quantities

- Atmospheric Pressure, P_a

  Absolute uncertainty: $\delta_{P_a} = \pm 400$ Pa

  Atmospheric pressure, P_a, was measured using a Digi-Sense Traceable® Digital Barometer. The manufacturer's listed accuracy was ±400 Pa with a resolution of 100 Pa. Only one reading of atmospheric pressure was recorded prior to any test, therefore a random component of uncertainty was not considered. The atmospheric pressure absolute uncertainty, $\delta_{\Delta P_a}$, consisted of the manufacturer's accuracy only.

- Differential Pressure (Omega), ΔP_1

  Absolute uncertainty: $\delta_{\Delta_{P_1}} = \pm\sqrt{6.2^2 + \delta^2_{\Delta_{P_1 ran}}}$ Pa

  The difference between the static pressure of the test section and the static/total pressure of the inlet of the wind tunnel, ΔP_1, was measured using an Omega PX653-10D5V pressure sensor with a full-scale range of 2.49 kPa. The manufacturer's specified accuracy was ±0.25% of full-scale, or ±6.2 Pa. This bias limit was considered along with its random component, $\delta_{\Delta_{P_1 ran}}$, for each data sample.

- Differential Pressure (Baratron), ΔP_2

  Absolute uncertainty: $\delta_{\Delta_{P_2}} = \pm\sqrt{(6.7\ or\ 16.7)^2 + \delta^2_{\Delta_{P_2 ran}}}$ Pa

  All differential pressures other than ΔP_1 (e.g. surface pressures, pitot-static) were measured using one of two Baratron 226A pressure sensors with a full-scale range of 2.67 kPa or 6.67 kPa, depending on the application. The manufacturer's documented accuracy was $\pm 0.25\%$ of full-scale, or $\pm 6.7/\pm 16.7$ Pa with a resolution of 0.01% of full-scale, or 0.27/0.67 Pa. The sensor's accuracy was considered along with its random component, $\delta_{\Delta_{P_2 ran}}$, for each data sample.

- Temperature, T

  Absolute uncertainty: $\delta_T = \pm\sqrt{(1.5)^2 + \delta^2_{T_{ran}}}\ ^\circ C$

  A type-K thermocouple was used to measure stagnation temperature in the test section. The standard type-K thermocouple accuracy of $\pm 1.5\ ^\circ C$ at $0^\circ C$ was assumed to be the bias limit. The thermocouple's accuracy was considered along with its random component, $\delta_{\Delta_{T ran}}$, for each data sample.

- Wall-Normal Distance, Z

  Absolute uncertainty: $\delta_Z = \pm 1/64$" The uncertainty of wall-normal distance for pitot rake measurements was conservatively estimated to be 1/64", taking into account the construction tolerance of the troughs (0.001") and small vibrations during testing.

Derived Quantities

- Velocity, U

  Since velocity was calibrated in a linear equation, the uncertainty of the calibration coefficients was determined using Eqs. 3.2, 3.3, and 3.7:

$$\delta_A = \delta_{\Delta P}\sqrt{\frac{\sum(\Delta P_1)^2}{N\sum(\Delta P_1)^2 - (\sum \Delta P_1)^2}} \tag{C.1}$$

  and

$$\delta_B = \delta_{\Delta P}\sqrt{\frac{N}{N\sum(\Delta P_1)^2 - (\sum \Delta P_1)^2}} \tag{C.2}$$

  where $\delta_{\Delta P}$ accounted for the uncertainty contributions from both the static and pitot-static differential pressures (see Eq. 8.21 in [37]):

$$\delta_{\Delta P} = \sqrt{(\delta_{\Delta P_2})^2 + (B\delta_{\Delta P_1})^2} \tag{C.3}$$

  The $\delta_{\Delta P_1}$ and $\delta_{\Delta P_2}$ measurement uncertainties are documented in the preceding section. It was assumed that these values were constant at each test point in a calibration run. This assumption neglected the negligible random component of uncertainty at a test point and greatly simplified the regression by mitigating the need for weighting.

  Using Eq. 3.1, a calibrated differential pressure, indicative of the true velocity, ΔP_v, was determined. Applying (3.7) to (3.1), the associated uncertainty in the calibrated differential pressure was:

$$\delta_{\Delta P_v} = \sqrt{\delta_A^2 + (\Delta P_1 \delta_B)^2 + (B\delta_{\Delta P_1})^2} \tag{C.4}$$

  Finally, velocity was determined using Bernoulli's principle:

$$U = \sqrt{\frac{2RT\Delta P_v}{P_a}} \tag{C.5}$$

The resulting uncertainty in velocity as determined by applying (3.7) to (C.5) and assuming negligible uncertainty in the perfect gas constant:

$$\delta_U = \frac{1}{2}\sqrt{\frac{2RT\Delta P_v}{P_a}\left[\left(\frac{\delta_T}{T}\right)^2 + \left(\frac{\delta_{\Delta P_v}}{\Delta P_v}\right)^2 + \left(\frac{\delta_{P_a}}{P_a}\right)^2\right]} \tag{C.6}$$

The relative uncertainty of velocity is notionally plotted in Fig. C.1. The worst-case uncertainty of velocity was lower than 2% and decreased by nearly an order of magnitude at the highest tunnel velocity.

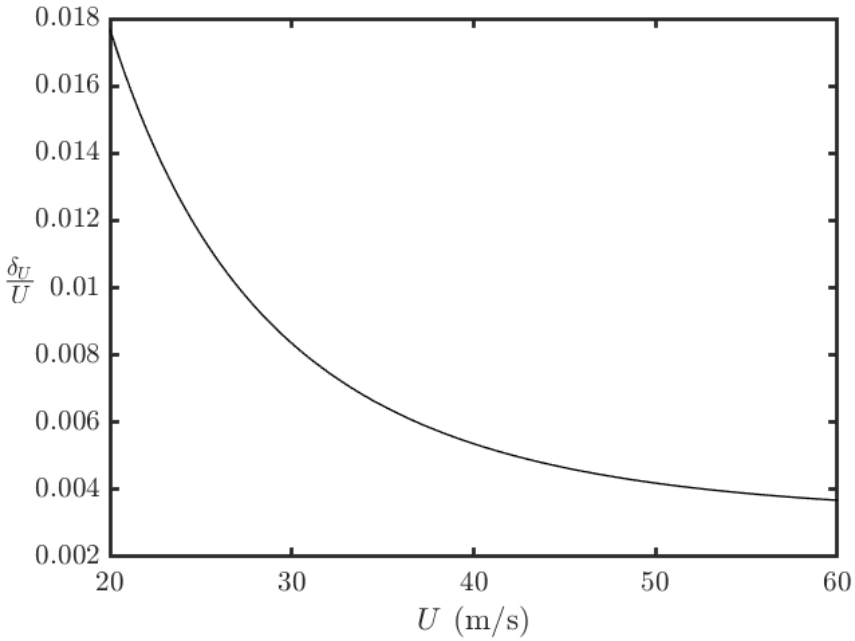

Figure C.1: Calibrated velocity uncertainty under nominal conditions.

- Coefficient of Pressure, C_P

  A simplified expression for the surface pressure coefficient was found by substituting (C.5) into (4.3):

$$C_P = \frac{\Delta P_2}{\Delta P_v} \tag{C.7}$$

  applying (3.7) yields the uncertainty of pressure coefficient:

$$\delta_{C_P} = \frac{1}{\Delta P_v}\sqrt{\left(\delta_{\Delta P_2}^2 + \frac{{\Delta P_2}^2 {\delta_{\Delta P_v}}^2}{{\Delta P_v}^2}\right)} \tag{C.8}$$

- Boundary Layer Thickness, δ

  The boundary layer thickness measured using a pitot rake was calculated by linearly interpolating the wall-normal distance between the distance of the first pitot tube measuring $\overline{U}/\widetilde{U}_\infty \geq 0.99$, and the distance of the tube immediately preceding it. Since the regression was linear, the error of the dependent variable was assumed to be equivalent to the error of the independent variable (see Eq. 8.21 in [37]):

$$\delta_\delta = \sqrt{\delta_Z^2 + (B\delta_{\frac{\overline{U}}{\overline{U}_{\infty,s}}})^2} \tag{C.9}$$

  where δ_Z is documented in the preceding measured quantities section, and the regression slope, B, had no uncertainty since the regression consisted of only two points. The uncertainty of the linearly interpolated independent variable, $\overline{U}/\widetilde{U}_{\infty,s}$ consisted of the precision uncertainties from both mean velocities used in the regression and the precision error of the freestream velocity. The bias error from all of these measurements was the same, and was neglected. Thus,

$$\delta_\delta = \sqrt{\delta_Z^2 + B^2\left(\left(\frac{\sigma_{\overline{U}_1}}{\sqrt{N_1}}\right)^2 + \left(\frac{\sigma_{\overline{U}_2}}{\sqrt{N_2}}\right)^2 + \left(\frac{\sigma_{\widetilde{U}_{\infty,s}}}{\sqrt{10}}\right)^2\right)} \tag{C.10}$$

- Median Inflow Quantities (e.g. $\widetilde{\delta}_{vel}$, $\widetilde{U}_{\infty_{Ceiling}}$)

  The uncertainty of median inflow quantities measured using a pitot rake was assumed to be the quadratic sum of the precision uncertainty of the series upon which the median was taken and the mean of all precision uncertainties of the constituent values in the series. For example:

$$\begin{aligned} &\textbf{if} \quad \widetilde{\delta}_{vel} = med\left(\widetilde{\delta}_{Ceiling}, \widetilde{\delta}_{Floor}, \widetilde{\delta}_{Port}, \widetilde{\delta}_{Starboard}\right) \\ &\textbf{then} \quad \delta_{\widetilde{\delta}_{vel}} = \sqrt{\left(\frac{\sigma_{\widetilde{\delta}_{vel}}}{\sqrt{4}}\right)^2 + \left(\frac{\frac{\sigma_{\widetilde{\delta}_C}}{\sqrt{N_C}} + \frac{\sigma_{\widetilde{\delta}_F}}{\sqrt{N_F}} + \frac{\sigma_{\widetilde{\delta}_P}}{\sqrt{N_P}} + \frac{\sigma_{\widetilde{\delta}_S}}{\sqrt{N_S}}}{4}\right)^2} \end{aligned} \tag{C.11}$$

- PIV Statistical Quantities

  The quantities obtained via PIV in this study were statistical products of time series measurements (i.e. mean velocity, Reynolds stresses). The random component of uncertainty was assumed to predominate with these quantities, and was formulated based on the standard deviation, σ, of the quantity, x, in the time series:

$$\sigma_x = \sqrt{\frac{1}{N-1}\sum_{i=1}^{N}(x_i - \overline{x})^2} \tag{C.12}$$

  where N is the number of samples in the time series.

  The propagation of random uncertainty into derived statistical quantities is detailed in Sciacchitano and Wieneke [49]. A summary of the formulas used is given below:

  Uncertainty of the mean:

$$\delta_{\overline{x}} = \frac{\sigma_x}{\sqrt{N}} \tag{C.13}$$

  Uncertainty of standard deviation:

$$\delta_{\sigma_x} = \frac{\sigma_x}{\sqrt{2(N-1)}} \tag{C.14}$$

Uncertainty of variance (Reynolds normal stress):

$$\delta_{\sigma_x^2} = \sigma_x^2 \sqrt{\frac{2}{N-1}} \tag{C.15}$$

Uncertainty of covariance (Reynolds shear stress):

$$\delta_{\sigma_{xy}^2} = \sigma_x \sigma_y \sqrt{\frac{1+\rho_{xy}^2}{N-1}} \tag{C.16}$$

where ρ_{xy} is the correlation coefficient.

Uncertainty of turbulent shear stress (TSS):

$$\delta_{TSS} = \sqrt{\frac{1}{16}(R_{xx} - R_{yy})^2 \times ((\delta_{R_{xx}})^2 + (\delta_{R_{yy}})^2) + R_{xy}^2 \times (\delta_{R_{xy}})^2} \tag{C.17}$$

Uncertainty of in-plane turbulent kinetic energy (TKE):

$$\delta_{TKE} = \sqrt{\left(\frac{\delta_{\sigma_U^2}}{2}\right)^2 + \left(\frac{\delta_{\sigma_W^2}}{2}\right)^2} \tag{C.18}$$

Uncertainty of velocity magnitude:

$$\delta_{|Vel|} = \sqrt{\left(\frac{\overline{U}\delta_{\overline{U}}}{|Vel|}\right)^2 + \left(\frac{\overline{W}\delta_{\overline{W}}}{|Vel|}\right)^2} \tag{C.19}$$

Appendix D

MATLAB™ REDUCTION SCRIPTS

To further document the signal processing procedures of this experiment, this section provides the scripts used for reduction of the final data products of this test campaign. According to Oberkampf and Smith [1]:

> "Any and all digital processing of the data, including assumptions made in the processing, must be reported at higher levels of completeness... In order to achieve high completeness levels, each digital operation should be described in detail. Ideally, the code used to perform the digital processing should also be provided."

A brief description can be found in the header of each script. Some lines of code were removed for brevity, including those involved with command line output, file operations, similar variable declarations (denoted by a comment where removed), and plotting.

D.1 Drivers

Listing D.1: ReadTunnelCond.m

```
1 function tunnel_cond = readTunnelConditionsV5(varargin)
2 % Calculates uncalibrated tunnel velocity and temperature from binary sensor
      inputs. May 2020.
3 % Input: binary text files of velocity and temperature, mean atmospheric
     pressure
4 % Outputs:
5 %   tunnel_cond.m: Scalar structure of tunnel conditions. Indices 1
6 %   through n correspond to discrete samples of tunnel conditions
```

```
7  %   corresponding to times when other data (e.g. Baratron pressure) was
       sampled.
8  %   Index n+1 corresponds to the full time history for a run.
9  %************************************************************************
10 Conds = dlmread([Folder '/Conditions.txt'],'\t'); % Read mean atmospheric
       pressure
11 Pa = Conds(1)*100; % (Pa) Atmospheric Pressure
12 Vlimits=dlmread([Folder '\Voltage Limits Velocity.txt'],'\t'); % Read
       velocity voltage limits
13 Vdiffr=max(Vlimits)-min(Vlimits);
14 Vminlim=min(Vlimits);
15 clear Vlimits
16 Tlimits=dlmread([Folder '\Voltage Limits Temperature.txt'],'\t'); % Read
       temperature voltage limits
17 Tdiffr=max(Tlimits)-min(Tlimits);
18 Tminlim=min(Tlimits);
19 clear Tlimits
20 fid=fopen([openFolder '\TunnelConditionsVel.bin'],'r','b'); % Binary to
       volts, velocity
21 volts=fread(fid,[length(Vdiffr),inf],'ubit16')';
22 for j=1:length(Vdiffr)
23     volts(:,j)=volts(:,j)/2^16*Vdiffr(j)+Vminlim(j);
24 end
25 fclose(fid);
26 Pomega = volts(:,1);
27 Dflag = volts(:,2);
28 clear volts
```

```
fid=fopen([openFolder '\TunnelConditionsTemp.bin'],'r','b'); % Binary to
    volts, temperature
volts=fread(fid,[length(Tdiffr),inf],'ubit16')';
for j=1:length(Tdiffr)
    volts(:,j)=volts(:,j)/2^16*Tdiffr(j)+Tminlim(j);
end
fclose(fid);
T = volts(:,1)+273.15; %(K) Volts to temperature
clear volts
rho = Pa./(287.058*T); % (kg/m^3) Density.
Pomega = Pomega * (2490.98/5) - 498.178;  %Volts to pressure (Pa)
if length(Pomega)>length(rho)
    Pomega(length(rho)+1 : end) = [];
end
Vo = real((Pomega.*2./rho).^0.5); % Pressure to velocity (m/s)
%% Output Data Structure
i = 1;
ind = 1;
Pomega_case = [];
rho_case = [];
T_case = [];
Vo_case = [];
flag_ind = [];
%Populate structure only with data taken under positive TTL signal
while i < length(Dflag)
    while Dflag(i)>1 && i < length(Dflag)
        Pomega_case = [Pomega_case Pomega(i)];
```

```
55          %Similar assignment for remaining variables
56
57          if i < length(Dflag)
58              i = i + 1;
59          end
60      end
61      if i == 1
62         ;
63      elseif Dflag(i-1) > 1
64          tunnel_cond(ind).Pomega = Pomega_case';
65          tunnel_cond(ind).Pomegamean = mean(Pomega_case');
66          tunnel_cond(ind).Pomegastd = std(Pomega_case');
67          tunnel_cond(ind).Pomegastdom = std(Pomega_case')/length(Pomega_case
               ');
68          tunnel_cond(ind).rho = rho_case';
69          tunnel_cond(ind).T = T_case';
70          tunnel_cond(ind).Tmean = mean(T_case');
71          tunnel_cond(ind).Tstd = std(T_case');
72          tunnel_cond(ind).Tstdom = std(T_case')/length(T_case');
73          tunnel_cond(ind).Tvar = max(T_case)- min(T_case);
74          tunnel_cond(ind).Vo = Vo_case';
75          Pomega_case = [];
76          rho_case = [];
77          T_case = [];
78          Tvar_case = [];
79          Vo_case = [];
80          ind = ind + 1;
```

```
    end
    i = i + 1;
end
flag_ind = min(flag_ind):max(flag_ind);
%Full duration
tunnel_cond(ind).Pomega = Pomega(flag_ind);
%Similar assignment for remaining variables in tunnel_cond
%% Calculate max difference
Pomegavar = max(tunnel_cond(ind).Pomega) - min(tunnel_cond(ind).Pomega);
Tvar = max(tunnel_cond(ind).T)-min(tunnel_cond(ind).T);
tunnel_cond(ind).Tvar = Tvar;
rhovar = max(tunnel_cond(ind).rho) - min(tunnel_cond(ind).rho);
Vovar = max(tunnel_cond(ind).Vo) - min (tunnel_cond(ind).Vo);
save(strcat(saveFolder,'/tunnel_cond.mat'),'tunnel_cond');
end
```

Listing D.2: PressureCal.m

```
function px_calib = pressure_calV6()
% Calculates calibration coefficients and their uncertainties for single
   calibration run
% of a set of two differential pressures. September 2020.
% Inputs: Directory of single calibration folder.
%   bara_type- 1: 20 Torr, 2: 50 Torr
% Outputs: vel_calib.mat
%   px_calib: Structure for single calibration containing:
%       coeff: [B,A]
%           A:  Zeroth order calibration coefficient (Pa)
%           B:  First order calibration coefficient (-)
```

```
%       delta_A: Uncertainty of A (Pa)
%       delta_B: Uncertainty of B (—)
%       pxomega: Array of mean Omega pressures sampled to determine
%       calibration line
%       pxbara: Array of mean Baratron pressures sampled to determine
%       calibration line
%*************************************************************************
% Get transducer uncertainty
bara_type = input('Enter Baratron: (1: 20 Torr, 2: 50 Torr)');
switch bara_type
    case 1
        delta_Pb = get_delta_measurand('Pb20'); % (Pa) Omega pressure
           transducer error
    case 2
        delta_Pb = get_delta_measurand('Pb50');
end
delta_Po = get_delta_measurand('Po');
tunnel_cond = readTunnelConditionsV5(openFolder); % Get tunnel conditions
Pblimits=dlmread([openFolder '\Voltage Limits Bara.txt'],'\t'); %Get voltage
    limits — velocity
Pbdiffr=max(Pblimits)—min(Pblimits);
Pbminlim=min(Pblimits);
clear Pblimits
filePattern = fullfile(openFolder, 'BaraPress_*'); %Obtain all Baratron
   binary files in directory
dataFiles = dir(filePattern);
%Sort array to ensure files are in correct order
```

```
for ii = 1:length(dataFiles)
    B = regexp(dataFiles(ii).name,'\d*','Match');
    dataFiles(ii).num = str2double(B{1});
end
dataFilesfields = fieldnames(dataFiles);
dataFiles_cell = struct2cell(dataFiles);
sz = size(dataFiles_cell);
dataFiles_cell = reshape(dataFiles_cell, sz(1), []);
dataFiles_cell = dataFiles_cell';
dataFiles_cell = sortrows(dataFiles_cell, 7);
dataFiles_cell = reshape(dataFiles_cell', sz);
dataFiles = cell2struct(dataFiles_cell, dataFilesfields, 1);
%Get Baratron voltages
n = 1;
Pbara = [];
for file = dataFiles'
    fid=fopen(file.name,'r','b');
    volts=fread(fid,[length(Pbdiffr),inf],'ubit16')';
    for j=1:length(Pbdiffr)
        volts = volts/2^16*Pbdiffr(j)+Pbminlim(j);
    end
    fclose(fid);
    Pbara(:,n) = volts(:,1);
    n = n + 1;
    clear volts
end
%Voltage to pressure
```

```
bara_type=dlmread([openFolder '\BaraType.txt'],'\t');
switch bara_type
    case 1
        Pbara = Pbara .* 266.645; %(Pa)
    case 2
        Pbara = Pbara .* 666.612;
end
Pbara_mean = mean(Pbara); %Get pressure statistics - Baratron
Pbara_std = std(Pbara);
% Get Omega Data
Pomega_mean = zeros(1,length(tunnel_cond)-1);
Pomega_std = zeros(1,length(tunnel_cond)-1);
for m = 1:length(tunnel_cond)-1
    Pomega_mean(1,m) = mean(tunnel_cond(m).Pomega);
    Pomega_std(1,m) = std(tunnel_cond(m).Pomega);
end
% Find Calibration Coefficients
coeff = polyfit(Pomega_mean,Pbara_mean,1);
%% Find uncertainty
delta_delta_P = sqrt(delta_Pb^2 + (coeff(1)*delta_Po)^2);
delta_A = delta_delta_P * (sqrt(sum(Pomega_mean).^2)/...
    (size(Pomega_mean,2)*sum(Pomega_mean.^2)-sum(Pomega_mean)^2));
delta_B = delta_delta_P * sqrt(size(Pomega_mean,2)/...
    (size(Pomega_mean,2)*sum(Pomega_mean.^2)-sum(Pomega_mean)^2));
%% Export data structure
px_calib.coeff = coeff;
%Similar assignment for remaining variables
```

```
save(strcat(saveFolder,'/vel_calib.mat'),'px_calib')
end
```

Listing D.3: SurfacePressures.m

```
function run_data = SurfacePressures(varargin)
% Main reduction script for a single-velocity surface pressure run. July
   2020.
% Required Subfunctions:
%   readTunnelConditionsV5.m: Reduces tunnel conditions if needed.
%   u_calU.m: Determines velocity uncertainty at a single point.
%   u_CpV2.m: Determines coefficient of pressure uncertainty at a single
   point.
% Ouput: run_data.dat
%   ##Row matches with tap number
%   pb:      (Pa) Pressure tap time series
%   pb_mean: (Pa) Average pressure at tap
%   pb_std:  (Pa) Standard deviation of pressure at tap
%   pb_stdom:(Pa) Standard deviation of mean of pressure at tap
%   U:       (m/s)Calibrated tunnel velocity
%   deltaU:  (m/s)Uncertainty of calibrated tunnel velocity
%   q:       (Pa) Tunnel dynamic pressure
%   Pv:      (Pa) Calibrated tunnel mean pressure differential (dynamic
   pressure)
%   deltaPv: (Pa) Uncertainty of calibrated tunnel mean pressure
   differential
%   Cp:      (-)  Coefficient of pressure at bump tap referenced to tap 1
%   deltaCp: (-)  Uncertainty of coefficient of pressure at bump tap
%************************************************************************
```

```
num_taps = 48;
%Load velocity/pressure calibration file
cal = dir(strcat(Folder,'\**\vel_calib*'));
load([cal.folder '/' cal.name]);
%Load tunnel conditions
if exist(strcat(Folder,'\Tunnel Conditions\tunnel_cond.mat'), 'file')~=2
    tunnel_cond = readTunnelConditionsV5(Folder);
else
    load([Folder '/Tunnel Conditions/tunnel_cond.mat']);
end
%Read sensor type - get range
bara_type=dlmread([Folder '\BaraType.txt'],'\t');
switch bara_type
    case 1 %20 Torr
        Plim = 20 * 133.322; % (Pa)
    case 2 %50 Torr
        Plim = 50 * 133.322; % (Pa)
end
%Get voltage limits - velocity
Vlimits=dlmread([Folder '\Voltage Limits Bara.txt'],'\t');
Vdiffr=max(Vlimits)-min(Vlimits);
Vminlim=min(Vlimits);
run_data(num_taps) = struct(); %Initialize structure
%% Process Data
P = tunnel_cond(num_taps+1).Pa;    %(Pa) Atmospheric/Stagnation pressure
for n = 1:num_taps
    fid=fopen([Folder '\BaraPress_' num2str(n) '.bin'],'r','b');
```

```
48      volts=fread(fid,[length(Vdiffr),inf],'ubit16')';
49      for j=1:length(Vdiffr)
50          volts(:,j)=volts(:,j)/2^16*Vdiffr(j)+Vminlim(j);
51      end
52      fclose(fid);
53      run_data(n).pb = volts(:,1)' .* (Plim/10);  %V to Pa Calb (0-10V, 20Torr
            )
54      run_data(n).pb_mean = mean(volts(:,1)' .* (Plim/10));
55      run_data(n).pb_std = std(volts(:,1)' .* (Plim/10));
56      run_data(n).pb_stdom = std(volts(:,1)' .* (Plim/10))/length(volts);
57      Ps = tunnel_cond(n).Pomega;%(Pa) Tunnel pressure differential (Omega)
58      T = tunnel_cond(n).T;      %(K) Tunnel stagnation temperature
59      run_data(n).T = mean(T);
60      rho = tunnel_cond(n).rho;  %(kg/m^3) Tunnel air density
61      run_data(n).U = ((px_calib.coeff(2) + px_calib.coeff(1).*Ps).*2./rho)
            .^0.5; %(m/s) Tunnel velocity
62      run_data(n).q = 0.5 .* rho .* run_data(n).U.^2; %(Pa) Tunnel dynamic
            pressure
63      [run_data(n).deltaU, run_data(n).Pv, run_data(n).deltaPv] = u_calU(P,Ps,
            T,px_calib);
64      run_data(n).Cp = (run_data(n).pb_mean - run_data(1).pb_mean)./...   %(-)
            Coefficient of pressure
65          (0.5*mean(rho)*mean(run_data(n).U)^2);
66      run_data(n).deltaCp = u_CpV2(run_data(n).Pv, run_data(n).deltaPv,
            run_data(n).pb,bara_type); %(-) Coefficient of pressure uncertainty
67      clear volts Ps T rho
68  end
```

```
save(strcat(Folder,'/run_data.mat'),'run_data')
end
```

Listing D.4: Uniformity.m

```
function run_data = Uniformity(varargin)
% Main reduction script for inflow uniformity tests. January 2021.
% Required subfunctions:
%   readTunnelConditionsV5.m: Reduces tunnel conditions if needed.
%   u_U.m: Determines velocity uncertainty at a single point.
% Ouput: run_data.dat
%   ##Row matches with rake tube number
%   pb:      (Pa) Pressure tap time series
%   pb_mean: (Pa) Average pressure at tap
%   pb_std:  (Pa) Standard deviation of pressure at tap
%   pb_stdom:(Pa) Standard deviation of mean of pressure at tap
%   T:       (K)  Average temperature while sampling tube
%   rho:     (kg/m^3) Average tunnel air density while sampling tube
%   U:       (m/s) Average tunnel velocity while sampling tube
%   delta_U:  (m/s)Uncertainty of flow velocity (bias and precision)
%   delta_U_prec:  (m/s)Uncertainty of flow velocity (precision only)
%   q:       (Pa) Dynamic pressure
%   U_norm:  ()   Velocity normalized to mean of last 10 tube velocities
%   delta_U_norm:()Normalized velocity uncertainty
%   delta:   (m) Boundary layer thickness (U = 0.99 Uinf with linear
%          interpolation between closest two points)
%   delta_deltaprec: (m) Uncertainty of delta (bias of tube location,
%       precision of both tube location and velocity)
%*************************************************************************
```

```
num_tubes = 30;
L = 36;
%Load tunnel conditions
if exist(strcat(Folder,'\Tunnel Conditions\tunnel_cond.mat'), 'file')~=2
    tunnel_cond = readTunnelConditionsV5(Folder);
else
    load(strcat(Folder,'/Tunnel Conditions/tunnel_cond.mat'));
end
%Read sensor type - get range
%bara_type = input('\nEnter Baratron type (1: 20Torr, 2: 50Torr): ');
   %1- 20Torr  2-50Torr
bara_type=dlmread(strcat(Folder,'\BaraType.txt'),'\t');
switch bara_type
    case 1 %20 Torr
        Plim = 20 * 133.322; % (Pa)
    case 2 %50 Torr
        Plim = 50 * 133.322; % (Pa)
end
%Get voltage limits - velocity
Vlimits=dlmread(strcat(Folder,'\Voltage Limits Bara.txt'),'\t');
Vdiffr=max(Vlimits)-min(Vlimits);
Vminlim=min(Vlimits);
%Load pitot tube locations
load tube_locs
tube_locs = tube_locs .* 0.0254;  %in to m
%Initialize structure
run_data(num_tubes) = struct();
```

```
%% Process Data
P = tunnel_cond(num_tubes+1).Pa;    %(Pa) Atmospheric/Stagnation pressure
for n = 1:num_tubes
    fid=fopen(strcat(Folder,'\BaraPress_',num2str(n),'.bin'),'r','b');
    volts=fread(fid,[length(Vdiffr),inf],'ubit16')';
    for j=1:length(Vdiffr)
        volts(:,j)=volts(:,j)/2^16*Vdiffr(j)+Vminlim(j);
    end
    fclose(fid);
    run_data(n).pb = volts(:,1)' .* (Plim/10);  %V to Pa Calb (0-10V, 20Torr
       )
    run_data(n).pb_mean = mean(volts(:,1)' .* (Plim/10));
    run_data(n).pb_std = std(volts(:,1)' .* (Plim/10));
    run_data(n).pb_stdom = std(volts(:,1)' .* (Plim/10))/length(volts);
    T = tunnel_cond(n).T;      %(K) Tunnel stagnation temperature
    run_data(n).T = mean(T);
    run_data(n).rho = mean(tunnel_cond(n).rho); %(kg/m^3) Tunnel air density
    run_data(n).U = (run_data(n).pb_mean*2/ run_data(n).rho)^0.5; %(m/s)
       Tunnel velocity
    run_data(n).q = 0.5 .* run_data(n).rho .* run_data(n).U.^2; %(Pa) Tunnel
        dynamic pressure
    run_data(n).delta_U = u_U(P,run_data(n).pb,T,bara_type); %(m/s) Velocity
        uncertainty
    run_data(n).delta_U_prec = ((run_data(n).pb_std*2/ run_data(n).rho)^0.5)
       ./length(run_data(n).pb); %(m/s) Velocity precision error
    clear volts Ps T
end
```

```
%Get data into array form
T = [run_data.T];
U_inf = mean([run_data((end-10:end)).U]);
delta_U_infprec = std([run_data(end-10:end).U])/sqrt(10);
for n = 1:num_tubes
    U(n,1) = run_data(n).U;         %(m/s) Velocity
    delta_U(n,1) = run_data(n).delta_U; %(m/s) Velocity uncertainty
    run_data(n).U_norm = run_data(n).U/U_inf;
end
% Calculate BL properties
        pos = 0;
        for i = num_tubes:-1:1
            if U(i) >= 0.99*U_inf
                pos = i;
            end
        end
        Umask = U./U_inf;
        run_data(num_tubes+1).Uinf = U_inf;
        Pos_coeff = polyfit(Umask(pos-1:pos),tube_locs(pos-1:pos),1);
        run_data(num_tubes+1).delta = polyval(Pos_coeff,0.99); %(m) BL
           thickness
        delta_z = 1/64 * 0.0254; %(m) Tube location uncertainty
        run_data(num_tubes+1).delta_deltaprec = mean(sqrt(delta_z^2 + (
           Pos_coeff(2).*[run_data(pos-1:pos).delta_U_prec]).^2) +
           delta_U_infprec^2); %(m) BL thickness uncertainty (precision only
            for U/U_inf)
        [run_data(num_tubes+1).delstar,run_data(num_tubes+1).theta,run_data(
```

```
            num_tubes+1).H] = ...
96              CalcBLThick(tube_locs,U',U_inf,[run_data(:).rho],1,2);
97  save(strcat(Folder,'/run_data.mat'),'run_data')
98  end
```

Listing D.5: ImportDavis10_BB.m

```
1   function ImportDaVis10_BB_V6(varargin)
2   % Imports image data from DaVis 10 to calculate statistical PIV fields.
        January 2021.
3   %
4   % Input: Folder_PIV: folder path of image set
5   %
6   % Output: Array and scattered interpolant object of statistical fields.
7   %%%%%%%%%%%%%%%%%%%%%%%%%%%%%%%%%%%%%%%%%%%%%%%%%%%%%%%%%%%%%%%%%%%%%%%
8   %% Determine Small or Large FOV and set constants
9   if contains(Folder_PIV,'Small')
10      SFOV = 1;
11  else
12      SFOV = 0;
13      max_station = 5;
14  end
15  if SFOV
16      scale_factor = 38.44; %pixels/mm
17      origin_shift_x = 315.24; %(pixels)
18      origin_shift_y = 89.56; %(pixels)
19      switch str2num(cell2mat(regexp(char(regexp(Folder_PIV,'Vel\d*','match'))
            ,'\d','match')))
20          case 20
```

```
            dt = 7.04;
        case 30
            dt = 5.59;
        case 40
            dt = 5.33;
        case 60
            dt = 4.16;
    end
else
    scale_factor = 11.84; %pixels/mm
    origin_shift_x = 114.03; %(pixels)
    origin_shift_y = 112.52; %(pixels)
    switch str2num(cell2mat(regexp(char(regexp(Folder_PIV,'Vel\d*','match'))
        ,'\d','match')))
        case 20
            dt = 44.7;
        case 30
            dt = 29.8;
        case 40
            dt = 22.35;
        case 60
            dt = 14.9;
    end
end
% Determine frame dimensions
fov_horz = 2560 / scale_factor; %(mm)
fov_vert = 2160 / scale_factor; %(mm)
```

```
47 z0 = 18*25.4; % (mm) z0 position for plate position=4
48 %Load velocity calibration coefficients
49 load('H:\Boeing Bump - Large FOV - Fall 2020\vel_calib.mat');
50 %Load tunnel conditions
51 try
52     load('Tunnel Conditions/tunnel_cond.mat');
53     %Calibrated freestream velocity
54     Uinf = ((tunnel_cond(end).Pomegamean * px_calib.coeff(1)...
55         + px_calib.coeff(2)).*2./mean([tunnel_cond(end).rho])).^0.5;
56     tunnel_cond(end).Vcal = Uinf;
57     save('Tunnel Conditions/tunnel_cond.mat','tunnel_cond');
58 catch
59     Uinf= str2num(cell2mat(regexp(char(regexp(Folder_PIV,'Vel\d*','match')),
        '\d','match')));
60 end
61 %Load frame coordinates
62 coord_file = dir('**\PIV_Coords*.*');
63 coord = readmatrix(coord_file.name).*25.4; %(mm)
64 % Set speed-bump definition (in)
65 L = 36; L_b = 35.5;
66 x_0 = 0.195 * L_b; y_0 = 0.06 * L_b; h_0 = 0.085* L_b;
67 Z_bump = @(x_bump,y_bump) (h_0/2) .* exp(-(x_bump./x_0).^2) .* (1 + erf((L_b
    /2 - 2*y_0 - abs(y_bump))./y_0));
68 %Find actual z coordinates based on wall location in raw image
69 try
70     wall_offset = (2160-FindWall(Folder_PIV))./scale_factor; %(mm) Bottom of
         image to plate/bump apex
```

```
71      if contains(Folder_PIV,'Long','IgnoreCase',true)
72          fprintf('\nNo z coordinate correction applied (long sample).\n')
73      elseif contains(Folder_PIV,'inflow','IgnoreCase',true)
74          coord(:,3) = z0 + fov_vert/2 - wall_offset;
75      else
76          dz = (z0 + h_0*25.4 + fov_vert/2 - wall_offset) - max(coord(:,3));
77          coord(:,3) = coord(:,3) + dz;
78      end
79  catch
80      fprintf('\nNo z coordinate correction applied.\n')
81  end
82  % Find station folder paths
83  ind = 1;
84  dir_loop = dir('loop*.*');
85  if exist('max_station','var')
86      if max_station*2 < length(dir_loop)
87          k = max_station*2;
88      else
89          k = length(dir_loop);
90      end
91  else
92      k = length(dir_loop);
93  end
94  for i = 1:k
95      if dir_loop(i).isdir
96          dir_piv = dir([dir_loop(i).folder '\' dir_loop(i).name '\PIV*']);
97          if contains(Folder_PIV,'long','IgnoreCase',true) %Long sample.
```

```
            Append PIV processed sets
98          for j = 1:length(dir_piv)
99              if dir_piv(j).isdir
100                 P(ind).DataPath = [dir_piv(j).folder '\' dir_piv(j).name
                        '\PostProcessed\Denoised'];
101                 ind = ind + 1;
102             end
103         end
104     else %Most tests. Take the most recent PIV processing set
105         P(ind).DataPath = [dir_piv(end-1).folder '\' dir_piv(end-1).name
                '\PostProcessed\Denoised'];
106         ind = ind + 1;
107     end
108     clear dir_piv
109 end
110 end
111 %% Process vector fields
112 for pos = 1:length(P)
113     d = dir([P(pos).DataPath '/*.vc7']);
114     d = {d.name};
115     numpics = length(d);
116     oldFolder = cd(P(pos).DataPath);
117     if numpics == 0
118         disp('No suitable files found')
119         cd(oldFolder)
120         return
121     end
```

```
122     %Take in span,stream, Z of PIV coordinate from test inputs
123     stream_coord = coord(pos,1);
124     span_coord = coord(pos,2);
125     z_coord = coord(pos,3);
126     %Initialize arrays
127     M = readimx(char(d(1)));
128     D = showimx(M.Frames{1});
129     U = zeros(size(D.U')); W = zeros(size(D.V'));
130     clear M D
131     %Extract data from frame
132     for pict=1:numpics
133         M = readimx(char(d(pict)));
134         D = showimx(M.Frames{1});
135         if pict ==1
136             X = D.X';
137             Z = D.Y'; %Wall-normal in Davis
138         end
139         U(:,:,pict) = D.U'; %add each velocity vector field values to
                overall array containing vector field for each image
140         W(:,:,pict) = D.V';
141         clear M D
142     end
143     close gcf
144     clear pict
145     %mm to  m
146     X = X/1000;
147     Z = Z/1000;
```

```
148     %Shift origin from DaVis to line up y to 0
149     X = X+origin_shift_x/scale_factor/1000;
150     Z = Z+origin_shift_y/scale_factor/1000;
151     %Offset data using PIV position inputs
152     X = X+(-stream_coord/1000)-fov_horz/2/1000;
153     Z = Z+((z_coord-z0)/1000)-fov_vert/2/1000;
154     %Flip Signs
155     X = -1.*X;
156     U = -1.*U;
157     %Remove Zeros
158     Vel = (U.^2.+W.^2).^0.5;
159     U(Vel==0)=NaN;
160     W(Vel==0)=NaN;
161     %Remove edges of frame
162     trim = 5;
163     Z = Z(trim:end-trim,trim:end-trim);
164     X = X(trim:end-trim,trim:end-trim);
165     U = U(trim:end-trim,trim:end-trim,:);
166     W = W(trim:end-trim,trim:end-trim,:);
167     %Calculate Statistical Properties
168     dim = size(U);
169     Umean = nanmean(U,3);           %(m/s) Mean streamwise velocity
170     Wmean = nanmean(W,3);           %(m/s) Mean normal velocity
171     Speed = sqrt(Umean.^2 + Wmean.^2); %(m/s) Total vector magnitude
172     Uvar = nanvar(U,[],3);          %(m/s)^2 Streamwise velocity variance;
            Rxx
173     Wvar = nanvar(W,[],3);          %(m/s)^2 Normal velocity variance; Rzz
```

```
174     Ustd = nanstd(U,[],3);          %(m/s) Streamwise velocity standard
           deviation
175     Wstd = nanstd(W,[],3);          %(m/s) Normal velocity standard
           deviation
176
177     %Calculate covariance; Reynolds shear stress
178     Uprime = zeros(dim); Wprime = zeros(dim);     UW = zeros(dim);
179     for j=1:dim(3)
180         Uprime(:,:,j) = U(:,:,j)-Umean(:,:);
181         Wprime(:,:,j) = W(:,:,j)-Wmean(:,:);
182         UW(:,:,j) = Uprime(:,:,j).*Wprime(:,:,j);
183     end
184     UWprime = nanmean(UW,3);    %(m/s)^2 Streamwise/Normal velocity
           covariance; Rxz
185     rho_UW = UWprime./(Ustd.*Wstd); %(-) Streamwise/Normal velocity
           correlation coefficient
186     pTKE = (Uvar + Wvar)./2;   %(m/s)^2 Planar turbulent kinetic energy
187     TSS = sqrt(0.25.*(Wvar-Uvar).^2 + UWprime.^2); %(m/s)^2 Turbulent shear
           stress
188     %Calculate uncertainty
189     U_Umean = Ustd.*sqrt(1/dim(3)); %(m/s) Streamwise mean velocity
           uncertainty
190     U_Wmean = Wstd.*sqrt(1/dim(3)); %(m/s) Normal mean velocity uncertainty
191     U_Speed = sqrt((Umean.*U_Umean./Speed).^2 + (Wmean.*U_Wmean./Speed).^2);
            %(m/s) Total velocity magnitude uncertainty
192     U_Ustd = Ustd.*sqrt(1/(2*(dim(3)-1))); %(m/s) Streamwise velocity
           standard deviation uncertainty
```

```
193     U_Wstd = Wstd.*sqrt(1/(2*(dim(3)-1))); %(m/s) Normal velocity standard
            deviation uncertainty
194     U_Uvar = Uvar.*sqrt(2/(dim(3)-1)); %(m/s) Rxx uncertainty
195     U_Wvar = Wvar.*sqrt(2/(dim(3)-1)); %(m/s) Rzz uncertainty
196     U_UWprime = Ustd.*Wstd.*sqrt((1+rho_UW.^2)/(dim(3)-1)); %(m/s) Rxz
            uncertainty
197     U_pTKE = sqrt((0.5.*U_Uvar).^2 + (0.5.*U_Wvar).^2); %(m/s)^2 pTKE
            uncertainty
198     U_TSS = (1./TSS).*sqrt((1/16).*(Uvar-Wvar).^2.*(U_Uvar.^2+U_Wvar.^2)+...
199         (UWprime.^2 .* U_UWprime.^2)); %(m/s)^2 Turbulent shear stress
                uncertainty
200     %Populate into data structure
201     P(pos).U = U;     P(pos).W = W;     P(pos).X = X;   P(pos).Z = Z;
202     P(pos).Input.Stream = stream_coord; P(pos).Input.Span = span_coord;
203     P(pos).Input.Wall_Normal = z_coord; P(pos).Input.Units = 'in';
204     Stats(pos).X = X;
205     %Similar assignment for remaining variables
206     clear U W d Umean Wmean Uvar Wvar Ustd Wstd UWprime pTKE TSS rho_UW
207     clear U_Umean U_Wmean U_Speed U_Uvar U_Wvar U_Ustd U_Wstd U_UWprime
            U_TSS U_pTKE
208 end
209 %% Create interpolant objects
210 % Meshgrid to coordinate vectors
211 ind = 1;
212 [Ny, Nx] = size(Stats(1).X);
213 for i = 1:length(P)
214     for j = 1:Ny
```

```
215         for k = 1:Nx
216             if ~isnan(Stats(i).U(j,k))
217                 VecX(ind) = Stats(i).X(j,k);
218                 %Similar assignment for remaining variables
219                 ind = ind + 1;
220             end
221         end
222     end
223 end
224 
225 FullField.U = scatteredInterpolant(VecX',VecZ',VecU','linear','none');
226 %Similar assignment for remaining variables
227 if SFOV
228     fileStats = 'SFOV_MATLAB_Processed_Stat.mat';
229     fileAll = 'SFOV_MATLAB_Processed.mat';
230 else
231     fileStats = 'LFOV_MATLAB_Processed_Stat.mat';
232     fileAll = 'LFOV_MATLAB_Processed.mat';
233 end
234 if exist('Tunnel Conditions/tunnel_cond.mat') ==2
235     save(strcat(saveFolder, casename, fileStats),'Stats',...
236         'FullField','coord','px_calib','tunnel_cond','-v7.3')
237     save(strcat(saveFolder, casename, fileAll),'P','Stats',...
238         'FullField','coord','px_calib','tunnel_cond','-v7.3')
239 else
240     save(strcat(saveFolder, casename, fileStats),'Stats',...
241         'FullField','coord','px_calib','-v7.3')
```

```
242     save(strcat(saveFolder, casename, fileAll),'P','Stats',...
243         'FullField','coord','px_calib','-v7.3')
244 end
245 end
```

D.2 Subfunctions

Listing D.6: U_U.m

```
1  function [delta_U] = u_U(P, Pb, T,bara_type)
2  % Calculates uncertainty of velocity. August 2020.
3  % Input (P, Ps, T):
4  %   % P: Atmospheric/Stagnation pressure (mean) (Pa)
5  %   % Ps: Differential pressure from static ports [Omega] (time series) (Pa)
6  %   % T: Stagnation temperature (time series) (K)
7  % Output: Uncertainty value of velocity (m/s).
8  % Required Subfunctions:
9  %   get_omega_measurand.m: Determines uncertainty of specific piece of
       equipment.
10 %%%%%%%%%%%%%%%%%%%%%%%%%%%%%%%%%%%%%%%%%%%%%%%%%%%%%%%%%%%%%%%%%%%%%%%%
11 % Set Constants
12 R = 287.05;      % (J/kg K) Ideal gas constant
13 % Get systematic uncertainty
14 delta_T = get_delta_measurand('T');  % (K) Thermocouple error
15 delta_P = get_delta_measurand('P');  % (Pa) Atmospheric pressure sensor
       error
16 switch bara_type
17     case 1
```

```
18          delta_Pb = get_delta_measurand('Pb20'); % (Pa) Omega pressure
                transducer error
19      case 2
20          delta_Pb = get_delta_measurand('Pb50'); % (Pa) Omega pressure
                transducer error
21  end
22  % Calculate sampling uncertainty
23  sigma_T_samp = std(T)/sqrt(length(T)); % (K) Standard deviation of the mean
24  sigma_Pb_samp = std(Pb)/sqrt(length(Pb)); % (Pa) Standard deviation of the
        mean
25  % Calculate total uncertainty
26  delta_T = sqrt(delta_T^2 + sigma_T_samp^2); % (K) Temperature total
        uncertainty
27  delta_Pb = sqrt(delta_Pb^2 + sigma_Pb_samp^2); % (Pa) Pressure total
        uncertainty
28  % Calculate velocity uncertainty
29  delta_U = 0.5*sqrt((2*R*mean(T)*mean(Pb)/P) * ((delta_T/mean(T))^2 + (
        delta_Pb/mean(Pb))^2 + (delta_P/P)^2));
30  end
```

Listing D.7: U_CalU.m

```
1  function [delta_U, Pv, delta_Pv] = u_calU(P, Ps, T, px_calib)
2  % Calculates uncertainty of calibrated velocity and differential
3  % pressure. September 2020.
4  % Input (P, Ps, T, px_calib):
5  %   % P: Atmospheric/Stagnation pressure (mean) (Pa)
6  %   % Ps: Differential pressure from static ports [Omega] (time series) (Pa)
7  %   % T: Stagnation temperature (time series) (K)
```

```
%   % px_calib: structure containing velocity calibration coefficients and
%       their uncertainties. Obtained from pressure_cal.m or vel_calib.m.
% Output: Uncertainty value of velocity and calibrated differential pressure
    (m/s).
% Required Subfunctions:
%   get_delta_measurand.m: Determines uncertainty of specific piece of
    equipment.
%*************************************************************************
%% Set Constants
R = 287.05;      % (J/kg K) Ideal gas constant
% Get systematic uncertainty
delta_T = get_delta_measurand('T');  % (K) Thermocouple error
delta_P = get_delta_measurand('P');  % (Pa) Atmospheric pressure sensor
    error
delta_Ps = get_delta_measurand('Po'); % (Pa) Omega pressure transducer error
% Calculate sampling uncertainty
sigma_T_samp = std(T)/sqrt(length(T)); % (K) Standard deviation of the mean
sigma_Ps_samp = std(Ps)/sqrt(length(Ps)); % (Pa) Standard deviation of the
    mean
% Calculate total uncertainty
delta_T = sqrt(delta_T^2 + sigma_T_samp^2); % (K) Temperature total
    uncertainty
delta_P = delta_P; % (Pa) Atmospheric pressure total uncertainty
delta_Ps = sqrt(delta_Ps^2 + sigma_Ps_samp^2); % (Pa) Static pressure total
    uncertainty
% Calculate calibrated pressure differential its uncertainty
Ps_mean = mean(Ps);    % (Pa) Mean static differential pressure
```

```
Pv = px_calib.coeff(2) + px_calib.coeff(1)*Ps_mean; %(Pa) Calibrated
   differential pressure
delta_Pv = sqrt(px_calib.sigmaA^2 + (Ps_mean*px_calib.sigmaB)^2 + ...
    (px_calib.coeff(1)*delta_Ps)^2);  %(Pa) Calibrated differential pressure
        uncertainty
% Calculate calibrated velocity uncertainty
T_mean = mean(T);       %(K) Mean temperature
delta_U = 0.5*sqrt((2*R*T_mean*Pv/P) * ((delta_T/T_mean)^2 + (delta_Pv/Pv)^2
    + (delta_P/P)^2));
end
```

Listing D.8: U_Cp.m

```
function delta_Cp = u_CpV2(Pv, delta_Pv, Pb,bara_type)
% Calculates random and systematic uncertainty of coefficient of pressure
%   at particular tap. May 2020.
% Input (Pv, delta_Pv, Pb):
%   % Pv: Calibrated pressure differential (mean) (Pa)
%   % delta_Pv: Calibrated pressure differential uncertainty (mean)(Pa)
%   % Pb: Bump pressure differential (time series)
% Output: Total uncertainty value of coefficient of pressure at particular
   tap.
% Required Subfunctions:
%   get_omega_measurand.m: Determines uncertainty of specific piece of
   equipment.
%   u_UV2.m: Calculates uncertainty of calibrated velocity and calibrated
%       pressure differential.
%*************************************************************************
% Get systematic uncertainty
```

```
switch bara_type
    case 1
        delta_Pb = get_delta_measurand('Pb20'); % (Pa) Omega pressure
           transducer error
    case 2
        delta_Pb = get_delta_measurand('Pb50'); % (Pa) Omega pressure
           transducer error
end
% Calculate sampling uncertainty
sigma_Pb_samp = std(Pb)/length(Pb); % (Pa) Standard deviation of the mean of
    bump pressure
% Calculate total uncertainty
delta_Pb = sqrt(delta_Pb^2 + sigma_Pb_samp^2); % (Pa) Bump pressure total
   uncertainty
delta_Cp = (1/Pv) * sqrt(delta_Pb^2 + (mean(Pb)^2 * delta_Pv^2)/Pv^2);
end
```

Listing D.9: get_delta_measurand.m

```
function error = get_delta_measurand(measurand)
% Calculates systematic error of individual measuring device. September
   2019.
% Input: String of desired measurand
%   % 'P': Atmospheric/Stagnation pressure (Pa)
%   % 'Po': Differential pressure from static ports [Omega] (Pa)
%   % 'Pb': Differential pressure from pitot tube [Baratron] (Pa)
%   % 'T': Stagnation temperature (K)
% Output: Uncertainty value of measurand in corresponding units.
%*********************************************************************
```

```
switch measurand
    case 'P'
        acc = 400;   %(Pa) Accuracy
        error = acc;
    case 'Po'
        %Systematic Error
        FS = 2490.89; %(Pa) Full scale range
        acc = 0.0025 * FS; %(Pa) Accuracy
        error = acc;
    case 'Pb20'
        %Systematic Error
        FS = 2666.6; %(Pa) Full scale range
        acc = 0.0015 * FS; %(Pa) Accuracy
        error = acc;
    case 'Pb50'
        %Systematic Error
        FS = 6666.12; %(Pa) Full scale range
        acc = 0.0012 * FS; %(Pa) Accuracy
        error = acc;
    case 'T'
        acc_t = 1.5; %(K) Type-K thermocouple accuracy
        error = acc_t;
end
end
```

Listing D.10: FindWall.m

```
function [y] = FindWall(Folder)
% Finds pixel location of wall at plate (Inflow) or bump apex (other).
```

```
   December 2020
% Inputs:
%   Folder: Path of test directory. Requires 'Export' subfolder from DaVis
%      Export operation (.im7 DaVis native format)
% Outputs:
%   wall: pixels from top of frame
%*************************************************************************
dat_loop = dir('**\Export\loop*.*');
ind = 1;
%Find median/min wall location of each station
for i = 1:length(dat_loop)
    if dat_loop(i).isdir
        %Import first raw image
        image_path = [dat_loop(i).folder '\' dat_loop(i).name '\B0001.im7'];
        img = readimx(image_path);
        img_dat = double(img.Frames{1, 1}.Components{1, 1}.Planes{1, 1});
        %Normalize pixel intensities and rotate
        img_dat = rot90(img_dat./max(max(img_dat)));
        %Find middle of wall (intensity above 99%)
        [yl,xl] = size(img_dat);
        for x = 1:xl
            wall_img(x) = yl-nanmedian(find(img_dat(:,x) > 0.99));
        end
        if contains(Folder,'inflow','IgnoreCase',true)
            wall_loop(ind) = nanmedian(wall_img);
        else
            wall_loop(ind) = nanmin(wall_img);
```

```
        end
        ind = ind + 1;
        clear wall_img image_path img img_dat yl xl
    end
end
%Find overall bump apex or plate location
if contains(Folder,'inflow','IgnoreCase',true)
    y = wall_loop';
elseif contains(Folder,'Small')
    y = nanmax(wall_loop);
else
    y = nanmin(wall_loop);
end
end
```

Appendix E

ANCILLARY RESULTS

Table E.1: Empty-tunnel boundary layer properties per station on **C**eiling, **F**loor, **S**tarboard and **P**ort walls, measured using pitot rake. Median quantities found in Tab. 4.2.

Nominal Velocity, m/s	Wall	y/L	z/L	δ_s (δ_{δ_s}), in	$\widetilde{U}_{\infty_s}$ ($\delta_{\widetilde{U}_{\infty_s}}$), in
20	C	13/36	-	0.19 (0.02)	25.36 (0.2)
		1/4	-	0.25 (0.02)	25.03 (0.2)
		1/6	-	0.51 (0.02)	25.01 (0.2)
		1/12	-	0.22 (0.02)	25.07 (0.2)
		0	-	0.28 (0.02)	24.80 (0.2)
		-1/2	-	0.29 (0.02)	25.37 (0.2)
		-1/6	-	0.15 (0.02)	25.40 (0.2)
	F	13/36	-	0.31 (0.02)	25.01 (0.2)
		1/4	-	0.33 (0.02)	25.34 (0.2)
		1/6	-	0.23 (0.02)	25.46 (0.2)
		1/12	-	0.58 (0.02)	25.70 (0.2)
		0	-	0.42 (0.02)	25.36 (0.2)
		-1/2	-	0.35 (0.02)	24.70 (0.2)
		-1/6	-	0.43 (0.02)	25.28 (0.2)
	S	-	13/36	0.33 (0.02)	24.58 (0.2)
		-	1/4	0.50 (0.02)	25.46 (0.2)
		-	1/6	1.37 (0.02)	25.09 (0.3)
		-	1/12	0.34 (0.02)	24.28 (0.3)

		-	0	0.39 (0.02)	24.95 (0.2)
		-	-1/2	0.89 (0.02)	24.64 (0.3)
		-	-1/6	0.38 (0.02)	25.30 (0.2)
	P	-	13/36	0.43 (0.03)	25.43 (0.2)
		-	1/4	0.33 (0.02)	25.45 (0.2)
		-	1/6	0.28 (0.02)	25.25 (0.2)
		-	1/12	0.29 (0.02)	25.26 (0.2)
		-	0	0.16 (0.02)	24.91 (0.2)
		-	-1/2	0.58 (0.02)	25.57 (0.2)
		-	-1/6	0.44 (0.02)	25.31 (0.2)
40	C	13/36	-	0.33 (0.02)	46.00 (0.2)
		1/4	-	0.38 (0.02)	45.65 (0.2)
		1/6	-	0.70 (0.02)	46.43 (0.2)
		1/12	-	0.47 (0.02)	46.30 (0.2)
		0	-	0.40 (0.02)	46.58 (0.2)
		-1/2	-	0.43 (0.02)	46.86 (0.2)
		-1/6	-	0.34 (0.02)	46.23 (0.2)
	F	13/36	-	0.42 (0.02)	46.21 (0.2)
		1/4	-	0.53 (0.02)	46.60 (0.2)
		1/6	-	0.39 (0.02)	45.75 (0.2)
		1/12	-	1.07 (0.04)	46.49 (0.2)
		0	-	0.51 (0.02)	46.03 (0.2)
		-1/2	-	0.49 (0.02)	46.42 (0.2)
		-1/6	-	0.48 (0.02)	46.10 (0.2)
	S	-	13/36	0.45 (0.02)	46.56 (0.2)
		-	1/4	0.54 (0.02)	46.44 (0.2)
		-	1/6	1.02 (0.02)	46.35 (0.2)

		-	1/12	0.40 (0.02)	46.03 (0.2)
		-	0	0.45 (0.02)	46.17 (0.2)
		-	-1/2	0.78 (0.02)	46.23 (0.2)
		-	-1/6	0.47 (0.02)	46.26 (0.2)
	P	-	13/36	0.53 (0.02)	46.67 (0.2)
		-	1/4	0.49 (0.02)	46.56 (0.2)
		-	1/6	0.42 (0.02)	46.17 (0.2)
		-	1/12	0.62 (0.02)	46.46 (0.2)
		-	0	0.44 (0.02)	46.72 (0.2)
		-	-1/2	0.46 (0.02)	46.60 (0.2)
		-	-1/6	0.96 (0.02)	46.34 (0.2)
60	C	13/36	-	0.35 (0.02)	65.32 (0.2)
		1/4	-	0.35 (0.02)	64.62 (0.2)
		1/6	-	0.69 (0.02)	63.58 (0.2)
		1/12	-	0.47 (0.02)	62.95 (0.2)
		0	-	0.45 (0.02)	64.74 (0.2)
		-1/2	-	0.41 (0.02)	64.70 (0.2)
		-1/6	-	0.32 (0.02)	65.18 (0.2)
	F	13/36	-	0.42 (0.02)	65.16 (0.2)
		1/4	-	0.53 (0.02)	63.93 (0.2)
		1/6	-	0.36 (0.03)	64.60 (0.2)
		1/12	-	1.10 (0.04)	64.17 (0.2)
		0	-	0.49 (0.02)	64.64 (0.2)
		-1/2	-	0.48 (0.02)	65.27 (0.2)
		-1/6	-	0.44 (0.02)	65.55 (0.2)
	S	-	13/36	0.42 (0.02)	65.44 (0.2)
		-	1/4	0.54 (0.03)	65.73 (0.2)

	-	1/6	0.96 (0.03)	65.83 (0.2)
	-	1/12	0.37 (0.03)	65.81 (0.2)
	-	0	0.42 (0.03)	65.78 (0.2)
	-	-1/2	0.49 (0.04)	65.84 (0.2)
	-	-1/6	0.51 (0.03)	65.96 (0.2)
P	-	13/36	0.42 (0.02)	65.24 (0.2)
	-	1/4	0.61 (0.02)	65.58 (0.2)
	-	1/6	0.45 (0.02)	65.73 (0.2)
	-	1/12	0.60 (0.02)	65.80 (0.2)
	-	0	0.34 (0.02)	65.75 (0.2)
	-	-1/2	0.42 (0.02)	65.81 (0.2)
	-	-1/6	0.46 (0.03)	65.79 (0.2)

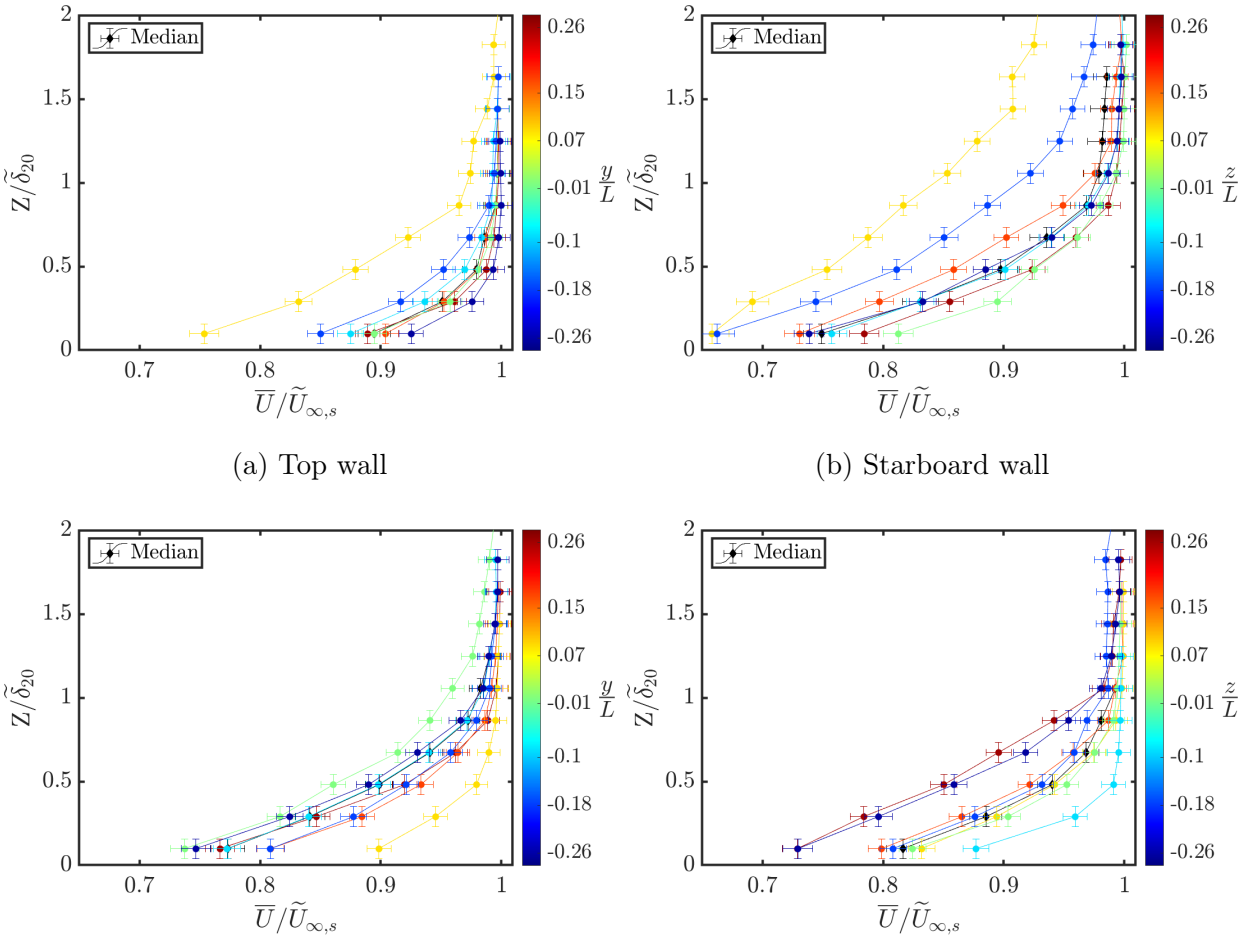

(a) Top wall

(b) Starboard wall

(c) Bottom wall

(d) Port wall

Figure E.1: Empty-tunnel wall inflow boundary layers by station at $Re_L = 1.40x10^6$ (20 m/s), x/L = -1.0.

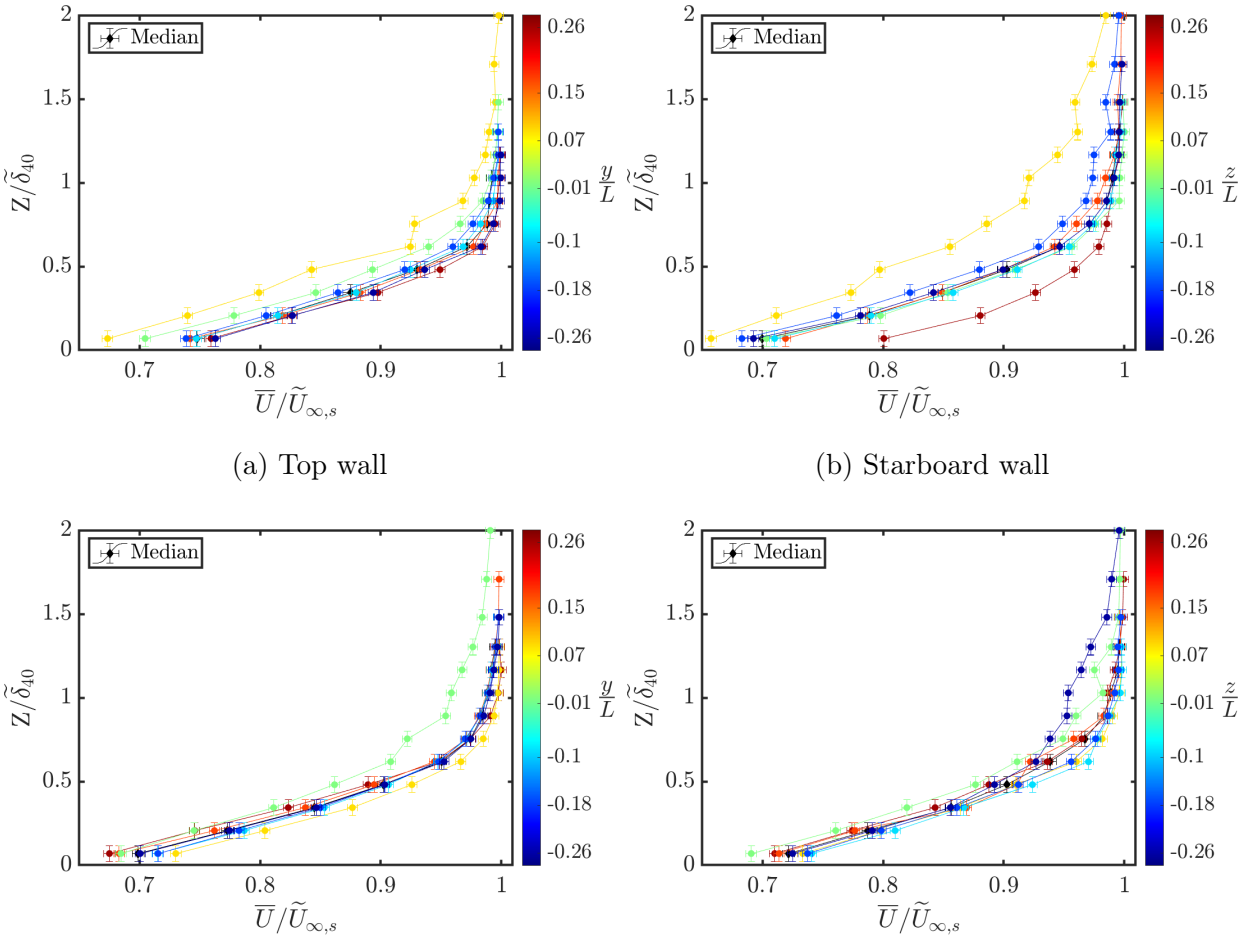

(a) Top wall

(b) Starboard wall

(c) Bottom wall

(d) Port wall

Figure E.2: Empty-tunnel wall inflow boundary layers by station at $Re_L = 2.55x10^6$ (40 m/s), x/L = -1.0.

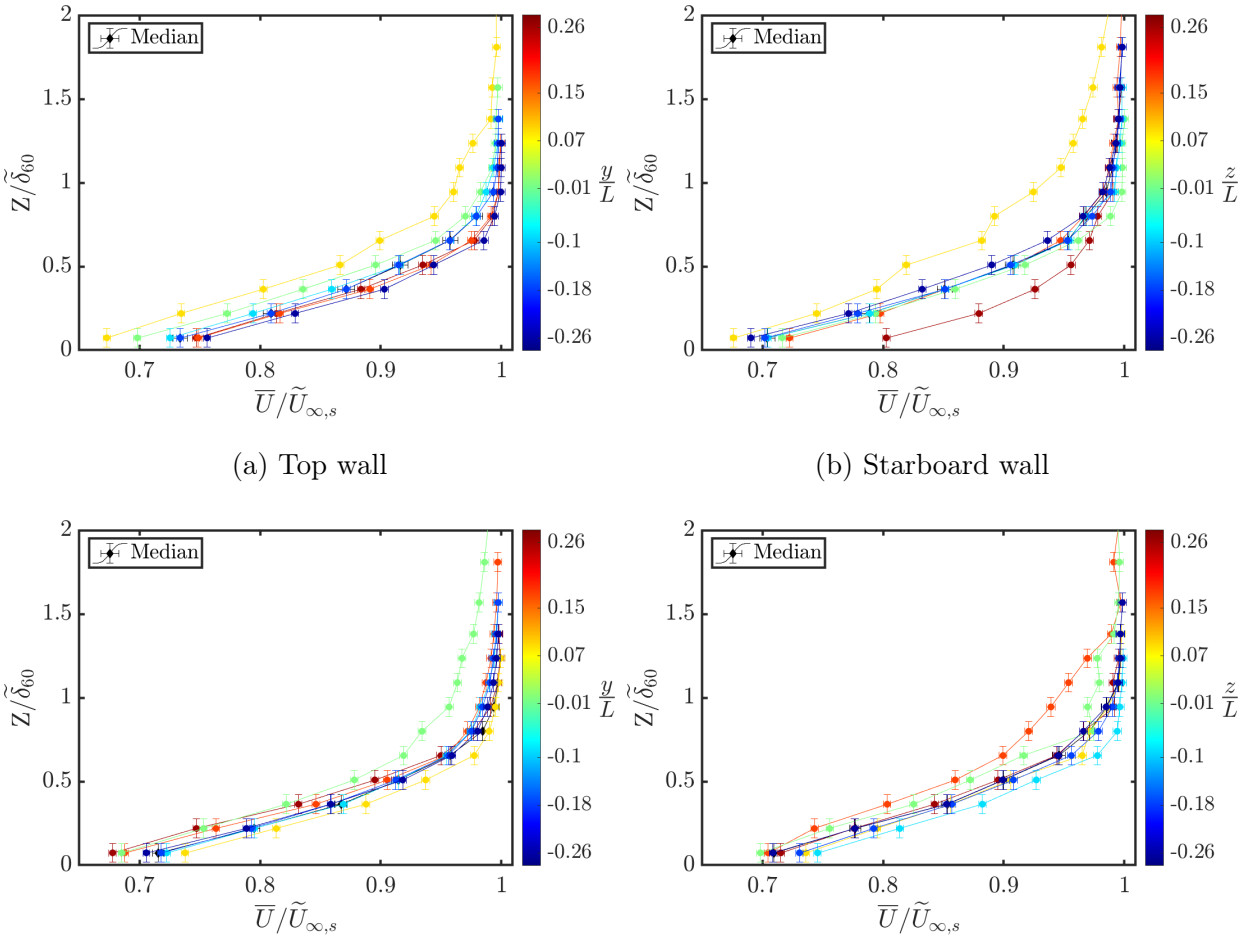

(a) Top wall

(b) Starboard wall

(c) Bottom wall

(d) Port wall

Figure E.3: Empty-tunnel wall inflow boundary layers by station at $Re_L = 3.57x10^6$ (60 m/s), x/L = -1.0.

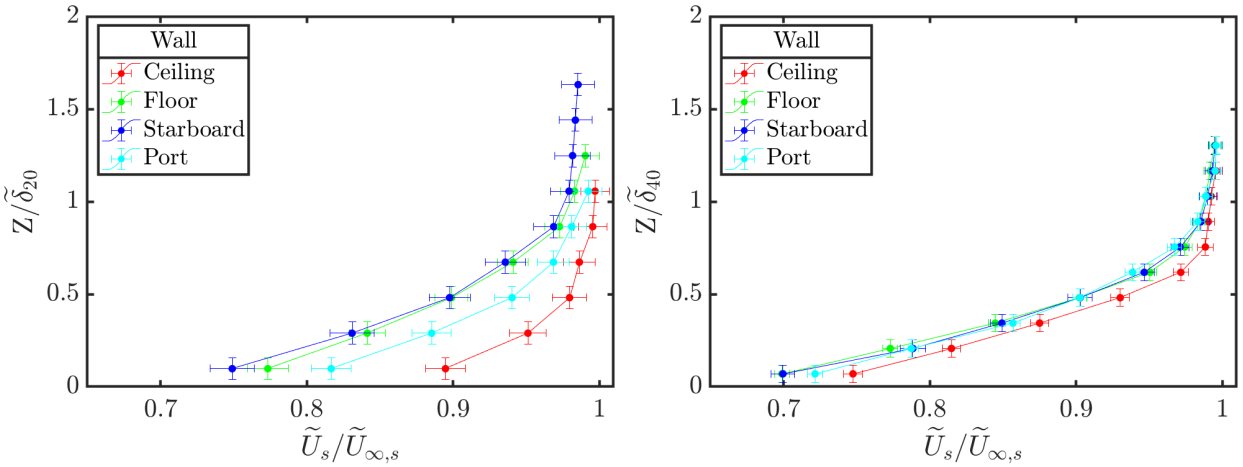

(a) $Re_L = 1.40x10^6$ (20 m/s)

(b) $Re_L = 2.55x10^6$ (40 m/s)

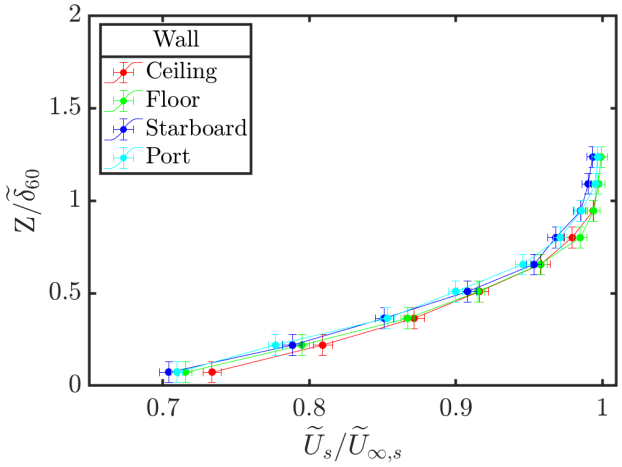

(c) $Re_L = 3.57x10^6$ (60 m/s)

Figure E.4: Empty-tunnel wall median inflow boundary layers by wall, x/L = -1.0.

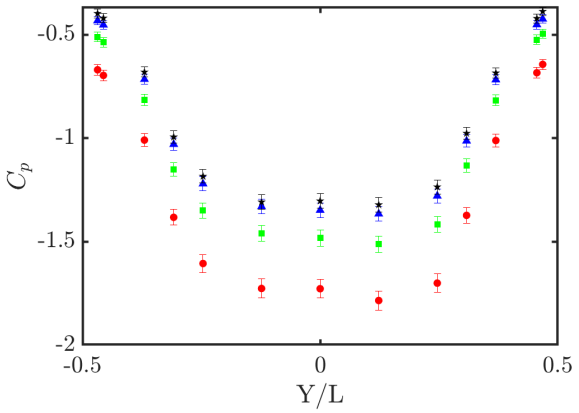

(a) $Re_L = 1.39x10^6$ (20 m/s)

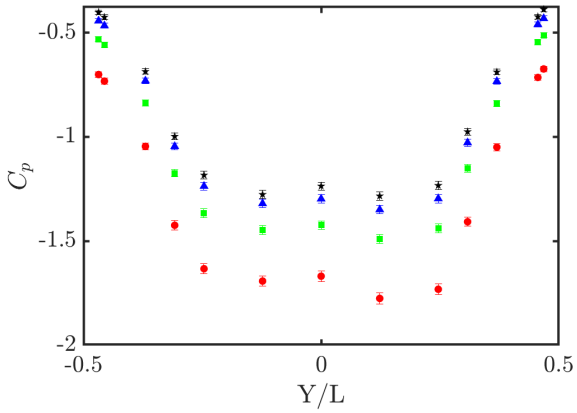

(b) $Re_L = 1.97x10^6$ (30 m/s)

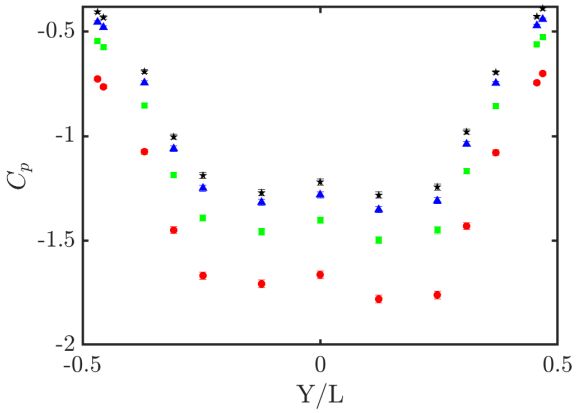

(c) $Re_L = 2.55x10^6$ (40 m/s)

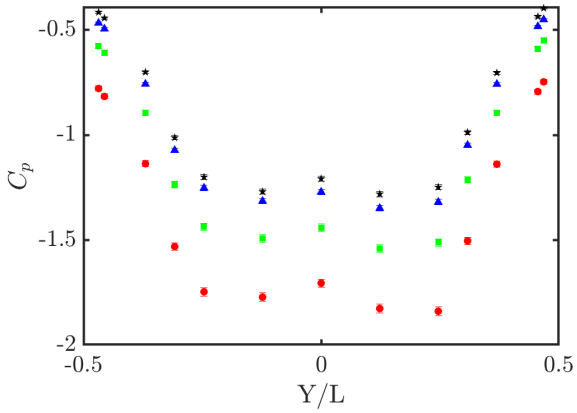

(d) $Re_L = 3.17x10^6$ (50 m/s)

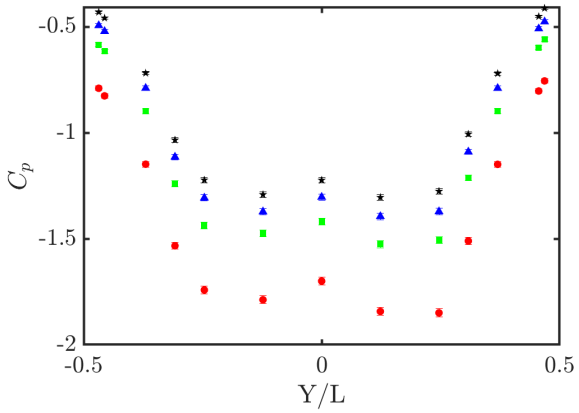

(e) $Re_L = 3.44x10^6$ (60 m/s)

Figure E.5: Confinement and Reynolds number sensitivity of surface pressure at streamwise centerline, x/L = 0. See legend on Fig. E.6.

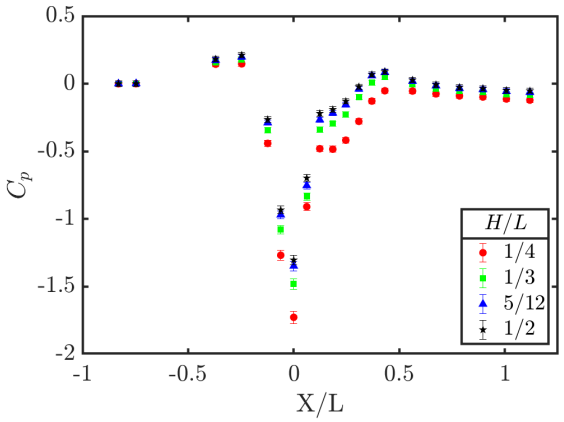

(a) $Re_L = 1.39x10^6$ (20 m/s)

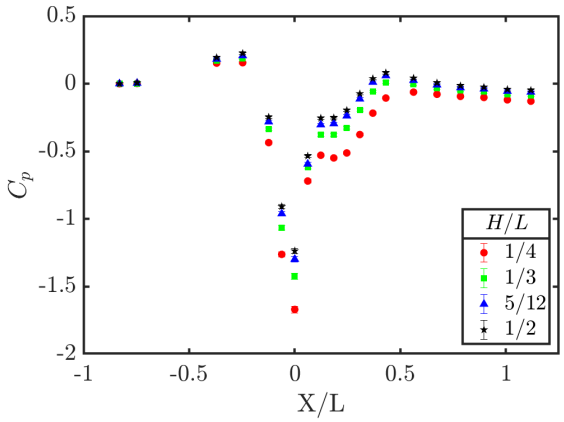

(b) $Re_L = 1.97x10^6$ (30 m/s)

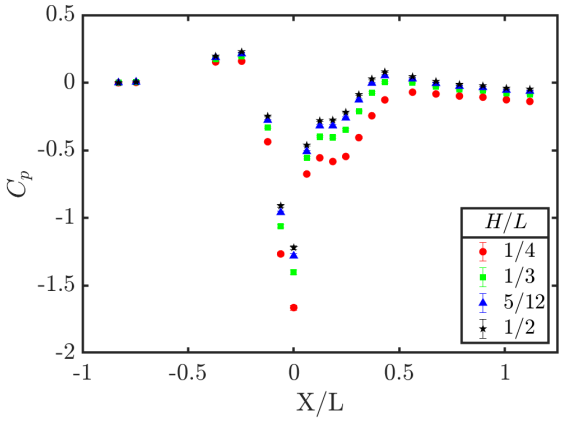

(c) $Re_L = 2.55x10^6$ (40 m/s)

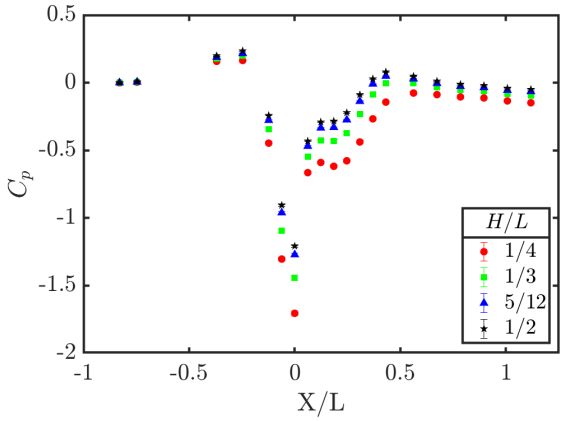

(d) $Re_L = 3.17x10^6$ (50 m/s)

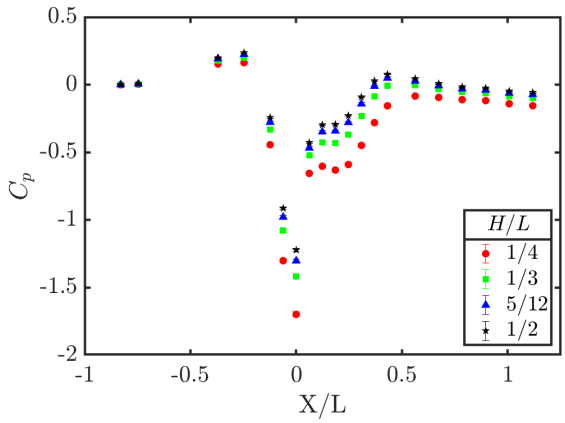

(e) $Re_L = 3.44x10^6$ (60 m/s)

Figure E.6: Confinement and Reynolds number sensitivity of surface pressures at spanwise centerline, y/L = 0.

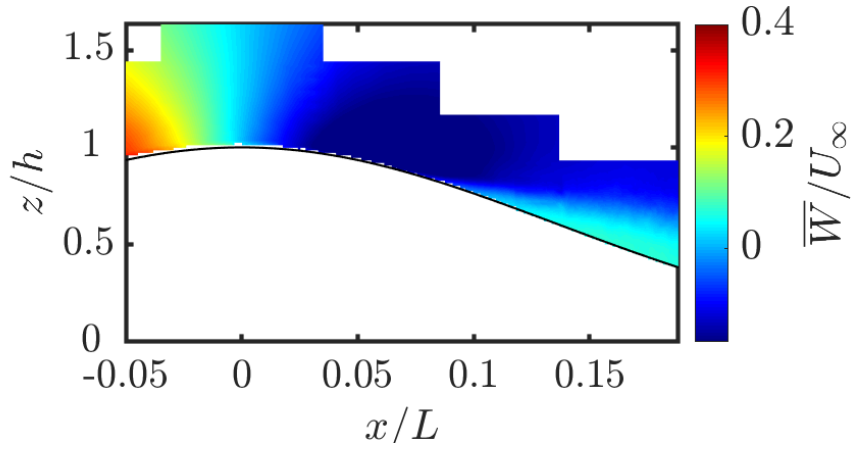

(a) $Re_L = 1.39x10^6$ (20 m/s)

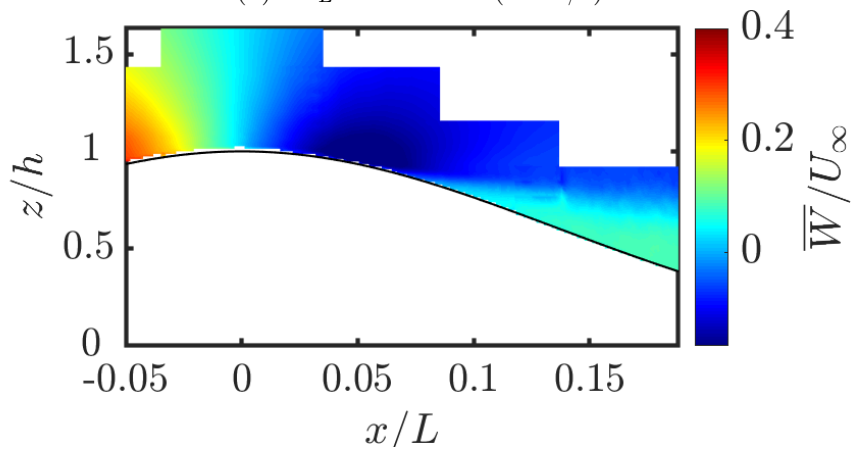

(b) $Re_L = 1.97x10^6$ (30 m/s)

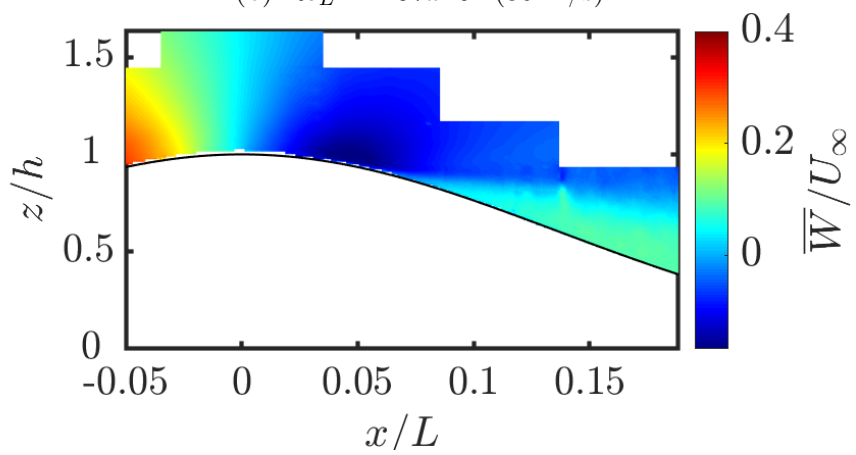

(c) $Re_L = 3.44x10^6$ (60 m/s)

Figure E.7: Mean normal component of velocity over the speed-bump near the separation point at y/L = 0 for various Reynolds numbers.

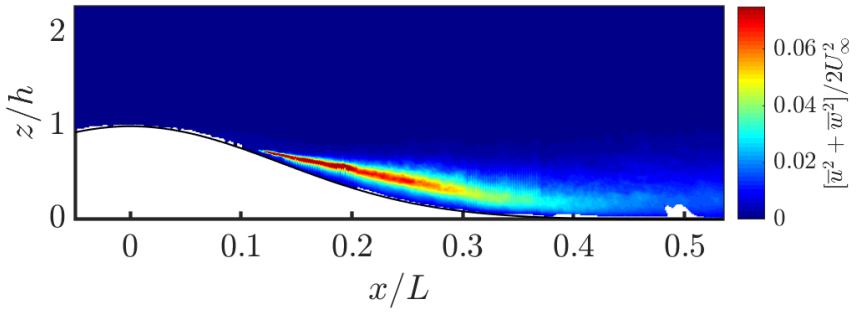

(a) $Re_{L} = 1.39x10^6$

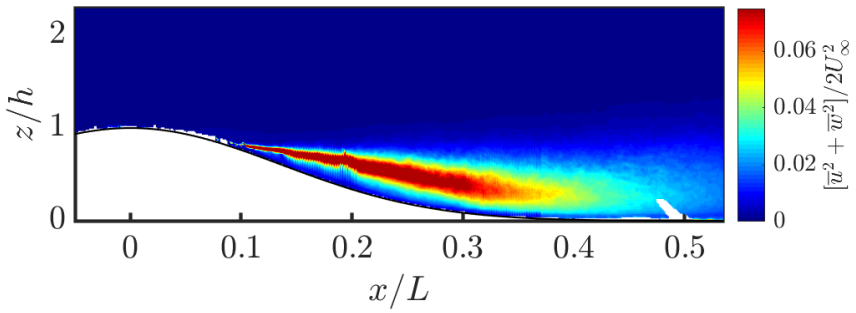

(b) $Re_{L} = 1.97x10^6$

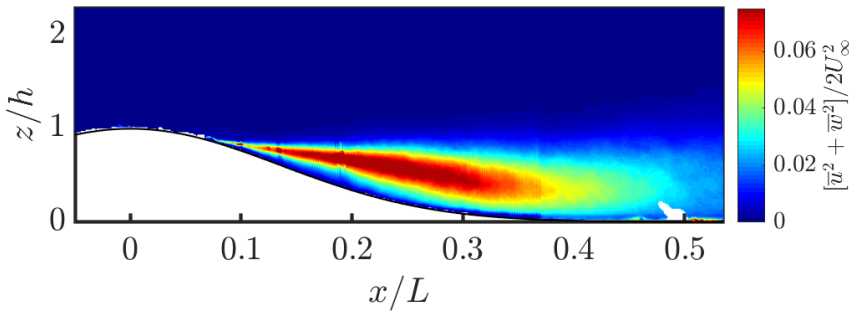

(c) $Re_{L} = 2.55x10^6$

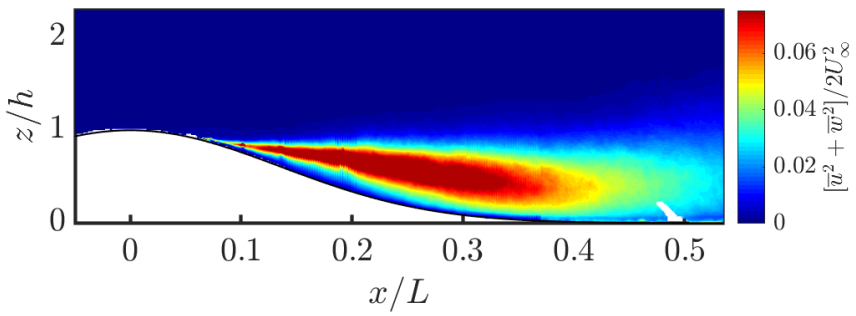

(d) $Re_{L} = 3.44x10^6$

Figure E.8: Mean turbulent kinetic energy near the separated region at various Reynolds numbers at y/L = 0.083, H/L = 1/2.